High-Precision Measurement of Strong-Interaction Effects in Pionic Deuterium

Inaugural-Dissertation

zur

Erlangung des Doktorgrades

der Mathematisch-Naturwissenschaftlichen Fakultät

der Universität zu Köln

vorgelegt von

Thomas Strauch

aus Olpe

Forschungszentrum Jülich
2009

Berichterstatter:	PD Dr. Detlev Gotta
	Prof. Dr. Andreas Zilges

Tag der mündlichen Prüfung: 30.06.2009

Zusammenfassung

Die hadronische Verschiebung ϵ_{1s} und Verbreiterung Γ_{1s} des Grundzustands in pionischem Deuterium wurde im Rahmen einer Hochpräzisionsmessung an der Pionfabrik des Paul Scherrer Instituts (PSI), Schweiz gemessen (PSI-Experiment R-06.03). Die Verschiebung ϵ_{1s} in pionischem Deuterium steht in direkter Beziehung zu den Pion-Nukleon Streulängen die im Rahmen der Messung der Verschiebung ϵ_{1s} und Verbreiterung Γ_{1s} in pionischem Wasserstoff ermittelt wurden (PSI-Experiment R-98.01). Die Kombination der hochpräzisen Daten des πH Experiments mit der Verschiebung ϵ_{1s} in πD erlaubt eine weitere Verbesserung im Rahmen der Rechnungen effektiver Feldtheorien wie der Chiralen Störungstheorie (χPT), die die QCD im nicht perturbativen Bereich beschreibt. Insbesondere ist die Verschiebung in πD im Gegensatz zu geladene Pion-Nukleon Reaktionen sehr empfindlich auf isospinbrechende Korrekturen. Desweiteren ist die hadronische Verbreiterung Γ_{1s} in πD auf direktem Wege mit Pionproduktion an der Schwelle verknüpft. Diese ist z. Zt. Gegenstand aufwändiger theoretischer Untersuchungen im Rahmen der χPT.

In diesem Experiment wurden die 3 keV Röntgenstrahlen des 3p-1s Übergangs in πD mit einem hochauflösenden Bragg Kristallspektrometer gemessen, das mit einem großflächigen ortsempfindlichen CCD Detektor bestückt war. Die charakteristische Röntgenstrahlung stammt aus der Abregungskaskade des pionischen Atoms. Um eine intensive Röntgenquelle mit pionischen Atomen zu erzeugen wird die Zyklotronfalle benutzt, die mit Hilfe eines fokussierenden Magnetfeldes den Pionenstrahl derart aufwickelt, daß er mit ausreichender Effizienz in einem kryogenischen D_2 Target gestoppt werden kann. Die Bestimmung der hadronischen Verschiebung ϵ_{1s} erfolgt durch Vergleich der gemessenen Übergangsenergie mit dem Wert für die rein elektromagnetische Übergangsenergie. Zur Bestimmung der hadronischen Verbreiterung benötigt man die genaue Kenntnis der Spektrometerauflösung. Diese wurde mit Hilfe von sehr schmalen Röntgenübergängen in stark ionisierten Atomen, die in einer Elektron-Zyklotron Ionen-Falle produziert wurden, gemessen.

Eine wesentliche Schwierigkeit des Experiments besteht in der Trennung der hadronischen Anteile in der gemessenen Energieverschiebung und Verbreiterung der Röntgenlinie von Beiträgen, die während der atomaren Kaskade durch Kollisionen der Atome mit dem πD Atom induziert werden. Es ist bekannt, daß bei diesen Kol-

lisionen komplexe Moleküle entstehen. Mögliche Röntgenemissionen aus molekularen Zuständen führen zu einer zusätzlichen Energieverschiebung. Da die Anzahl entstehender Moleküle druckabhängig ist, wurde der 3p-1s Übergang in πD bei drei verschiedenen Deuteriumdichten gemessen.

Bei einem weiteren Prozess der atomaren Kaskade, der sogenannten Coulomb-Abregung, wird die freiwerdende Abregungsenergie in kinetische Energie der Kollisionspartner umgesetzt. Dies führt zu einer Dopplerverbreiterung nachfolgender Röntgenübergänge. Zur Bestimmung der hadronischen Verbreiterung Γ_{1s} müssen folglich die Auflösungsfunktion des Spektrometers und die Anteile der Dopplerverbreiterung aus dem gemessenen Spektrum entfaltet werden.

Eine Druckabhängigkeit der Energie-, respektive der Linienverschiebung konnte nicht gefunden werden, d.h., der Anteil von Röntgenübergängen aus molekularen Zuständen liegt unter der Nachweisschwelle und wird daher vernachlässigbar. Das Ergebnis für die hadronische Verschiebung des Grundzustandniveaus lautet $\epsilon_{1s} = (-2,325 \pm 0,031)\,\mathrm{eV}$ entsprechend einem relativen Fehler von 1,3%. Dieser Wert wurde aus dem Mittel der bei drei verschiedenen Drücken gemessenen Verschiebungen bestimmt. Der Fehler wird dominiert durch die Genauigkeit des Gallium Kα_2 Übergangs der zur Energiekalibrierung genutzt wurde.

In der Analyse der Linienform konnten keine Dopplerverbreiterung durch Hochenergiekomponenten identifiziert werden. Limitiert man diese somit auf kinetische Energien von wenigen eV lautet das Ergebnis für die hadronische Grundzustandsverbreiterung $\Gamma_{1s} = (1,162^{+0,024}_{-0,049})\,\mathrm{eV}$. Dies entspricht einer relativen Genauigkeit von $^{+2,1}_{-4,2}\,\%$.

Die Präzision der beiden in diesem Experiment ermittelten Werte erreicht oder übertrifft die Genauigkeit der heutigen und in naher Zukunft erwarteten Berechnungen im Rahmen der χPT. Somit befinden sich Experiment und Theorie auf einem vergleichbaren Stand bei der Bestimmung der Pion-Nukleon Streulängen und von diesen abgeleiteten Parametern.

Abstract

The hadronic ground state shift ϵ_{1s} and width Γ_{1s} in pionic deuterium were measured with high precision at the pion factory of the Paul Scherrer Institut (PSI), Switzerland (PSI-Experiment R-06.03). The shift ϵ_{1s} in pionic deuterium is directly related to the pion-nucleon isospin scattering lengths as measured from the shift ϵ_{1s} and broadening Γ_{1s} in pionic hydrogen (PSI-Experiment R-98.01). The combination of the high-precision results from πH with the value from πD will provide a decisive constraint for effective field theories like chiral perturbation theory (χPT) describing QCD in the non-perturbative regime. In particular, the shift in πD is very sensitive to isospin-breaking corrections in contrast to charged pion-nucleon reactions. Furthermore, the hadronic width Γ_{1s} in πD is directly related to pion production at threshold, a field of considerable efforts from the theoretical side also within the frame work of χPT.

In this experiment the πD(3p-1s) X-ray transition of about 3 keV was measured using a high-resolution Bragg crystal spectrometer equipped with a large-area position sensitive CCD detector. The characteristic X-radiation stems from a de-excitation cascade of the pionic atom. In order to produce an intense X-ray source, the cyclotron trap was used to stop pions in a cryogenic D_2 target after winding up the pion beam in a magnetic field. The hadronic shift ϵ_{1s} is obtained from the measured transition energy by comparison to the pure electromagnetic value, where the determination of the broadening Γ_{1s} requires the precise knowledge of the spectrometer response, obtained from measurements of narrow X-ray transitions from highly ionised atoms, produced in an electron cyclotron resonance ion trap.

The major problem of the experiment is to disentangle from the observed energy shift and width of the X-ray line the pure hadronic contributions from collision-induced effects during the atomic cascade. It is known, that molecules are formed in $\pi D + D_2$ collisons and a possible X-ray emission from molecular states leads to an additional energy shift. As the formation rate is assumed to be density dependent, the πD(3p-1s) X-ray energy was measured at three different D_2 pressures.

Another cascade process (Coulomb de-excitation) transforms the energy release of de-excitation steps into kinetic energy of the collision partners leading to a Doppler broadening of subsequent X-ray transitions. The hadronic broadening Γ_{1s} is only obtained after deconvolution of the spectrometer response function and the contributions

from Doppler broadening.

No energy dependence of the πD(3p-1s) was found, and it is concluded that radiative de-excitation from molecular states is negligible within the experimental accuracy. Hence, the result for the shift reads $\epsilon_{1s} = (-2.325 \pm 0.031)\,\mathrm{eV}$, corresponding to an accuracy of 1.3% and represents the average of the three measured densities. The uncertainty is dominated by the accuracy of the gallium Kα_2 transition used for the energy calibration.

From the analysis of the Doppler broadening no significant contribution from high kinetic energies could be identified from the line shape. With Doppler contribution constrained to kinetic energies below a few eV, the result for the hadronic ground-state width is $\Gamma_{1s} = (1.162^{+0.024}_{-0.049})\,\mathrm{eV}$, corresponding to an accuracy of $^{+2.1}_{-4.2}\,\%$.

The precision of both shift and width as obtained in this experiment reaches or exceeds the accuracy envisaged in present and forthcoming χPT calculations. Hence, experiment and theory contribute at comparable level to the extraction of the pion-nucleon scattering lengths and related parameters.

Contents

List of Figures

List of Tables

Chapter 1

Introduction

1.1 Motivation

Quantum chromodynamics (QCD) is today's fundamental microscopic theory of strong interaction. QCD is a gauge theory based on coloured quarks and coloured field quanta called gluons. The complex quark-gluon and gluon-gluon interaction results in a running strong coupling "constant" α_s being small at high energies (asymptotic freedom). Therefore, in this regime conventional perturbative methods using α_s as order parameter can be applied with great success. The picture changes at low energies where the coupling constant increases to the order 1 and, therefore, this perturbation methods fail to describe the interaction of strongly interacting particles (hadrons).

Hence, to describe this interaction at low energies microscopically, a different approach becomes necessary. The method is based on the observation, that charged pions are much lighter than nucleons. In the limit of vanishing mass the pion even becomes stable thus conserving the so called axial current (pions belong to the pseudoscalar meson octet 0^-). In the real world pions do decay but only slowly, a fact described under the keyword partially conserved axial current (PCAC) [1]. Taking further into account, that hadrons are build up by almost massless quarks of a few MeV/c^2, the hadron masses are almost entirely due to the strong interaction.

Microscopically, PCAC is now understood to originate from the fact, that massless fermions can not change their spin projection as required by the weak decay $\pi \rightarrow \mu\nu$. This conservation is behind the so called chiral symmetry which must be slightly broken because of the small but finite quark masses. Though the symmetry is slightly broken, it still determines the strong low-energy interaction of the 0^- mesons with hadronic matter. Formulated in the frame work of an effective field theory, perturbative methods become applicable also at low energies.

Chiral perturbation theory (χPT) as a new frame work dates back to an idea of S.Weinberg in the outgoing seventies [2]. In the eighties Gasser and Leutwyler developed χPT [3, 4] and the theoretical basis was laid by Leutwyler [5]. This effective field theory considers the QCD Lagrangian in the chiral limit, i.e., treating the light quarks u, d and s as massless, leading to conservation of chirality as explained. The quark masses are then introduced as perturbation, describing the explicitly broken chiral symmetry. Especially for the up and down quark with masses of 3 and 5 MeV/c^2, respectively, which are small on the strong interaction scale corresponding to about the nucleon's mass, the symmetry breaking is small as the zero mass limit is closely approached. This is then even true for light mesons like pions, which are combined from up and down quarks and the lightest strongly interacting particles. Therefore, χPT works best for cases involving the two lightest quarks as for the description of pion-pion interaction [6, 7]. Applied to the meson-nucleon case the approach is often denoted as Heavy Baryon Chiral Perturbation Theory (HBχPT) [1, 8, 9, 10, 11].

In χPT the symmetry properties of the QCD Lagrangian manifest in observables related by low-energy theorems. Ordering the chiral expansion by counting the powers of small momenta, the quark mass difference (m_d–m_u) and the fine structure constant α allows to include on the same footing strong isospin-breaking effects resulting from the quark mass difference and those of electromagnetic origin. Parameterisation of the unknown QCD structure of short range is done using so-called low energy constants (LECs), which must be taken from experiment. In leading order of the hadron-hadron interaction the LECs can be identified by the s-wave scattering lengths.

Partly, theoretical calculations in HBχPT have been performed already in 3rd and 4th order in the chiral expansion. Therefore, the extraction of scattering lengths from experiment at a level of 1% or better must be the aim.

To study the interaction at low energies hadronic atoms provide an ideal laboratory. In this atoms the relative energies are restricted to the keV range and thus they represent a scattering experiment at threshold [12]. The strong interaction effects manifest in a shift ϵ and a width Γ of the low-lying atomic states. Access to these quantities is possible by measuring the characteristic X-radiation, which is emitted during the de-excitation cascade starting after formation.

1.2 πH and πD X-ray measurements

The pionic hydrogen collaboration [13] performed experiments in this field.

In a series of experiments the hadronic ground state shift ϵ_{1s} and broadening Γ_{1s} in pionic hydrogen (πH) were studied by measuring the K X-radiation having transition energies in the range of 2.4 keV to 3 keV. Preliminary results of these experiments for the ground state shift and width are [14]

$$\epsilon_{1s} = (7.120 \pm 0.008 \pm 0.006)\, eV, \;\; \frac{\Delta\epsilon_{1s}}{\epsilon_{1s}} = 0.2\% \tag{1.1}$$

and

$$\Gamma_{1s} = (0.823 \pm 0.019)\, eV, \quad \frac{\Delta\Gamma_{1s}}{\Gamma_{1s}} = 2.3\%. \tag{1.2}$$

From these quantities the two πN scattering lengths, arising from the two possible isospin combinations, are extracted with an accuracy on the few per cent level.

In the frame work of χPT the ground state shift in πD is unambiguously related to the πN scattering lengths including the same (three) LECs as in the πH case in next-to-leading order (NLO). Noteworthy, that one of these LECs (f_1) is not well known from other sources, and that in a combined analysis of the πH data and the πD shift a decisive constraint on f_1 can be provided. Consequently, the determination of the strong-interaction shift from experiment with an accuracy comparable to the accuracy extracted from the pionic hydrogen experiment is desirable [15].

Another field of significant theoretical effort within the framework of χPT is pion production [16]. The imaginary part of the πD scattering length $\Im a_{\pi D}$, obtained from the hadronic broadening of the ground state, is directly related to pion production reactions at threshold. At present $\Im a_{\pi D}$ is calculated with an accuracy of 30 % within χPT. In the near future this accuracy is expected to be improved significantly to ≈ 5 % [17]. Hence, a value of the ground state width with comparable precision should be available.

Measurements of the characteristic X-radiation from pionic deuterium started with a first pioneering experiment in 1974 [18]. The experiment measured the 2p-1s transition (2.6 keV) by the critical absorber technique and extracted the shift ϵ_{1s} to be $-4.8^{+1.6}_{-2.0}$ eV. In 1985 this shift was measured by means of a curved graphite crystal spectrometer to be (-5.5±0.1) eV [19]. The first measurement measuring also the ground state width Γ_{1s} was performed in the early nineties [20]. This experiment used, as the following experiments including this work, a high resolution crystal spectrometer and the high-intensity pion beam at the meson factory at PSI, Switzerland. The hadronic shift and width were determined from the 3p-1s transition (3.1 keV) to $\epsilon_{1s} = (-2.43 \pm 0.10)$ eV and $\Gamma_{1s} = (1.02 \pm 0.21)$ eV. The most precise measurement until now, using the 2p-1s transition [21] resulted in

$$\epsilon_{1s} = (-2.469 \pm 0.055)\, eV, \quad \frac{\Delta\epsilon_{1s}}{\epsilon_{1s}} = 2\% \tag{1.3}$$

and

$$\Gamma_{1s} = (1.194 \pm 0.105)\, eV, \quad \frac{\Delta\Gamma_{1s}}{\Gamma_{1s}} = 8.8\%. \tag{1.4}$$

1.3 Aim and strategy

In 2006 the new πD-experiment [15] was setup at PSI. Aim of the measurement described in this work is to improve on the strong-interaction effects by at least a factor of 2, i.e., to achieve an accuracy equal or better than the forthcoming theoretical results achieved within χPT. In this experiment the πD(3p-1s) transition energy and line shape was measured. To reach the high precision the measurement was done by means of a highly sophisticated high resolution Bragg crystal spectrometer in Johann geometry. As with such a device only relative energy measurements are possible, Ga Kα_2 X-rays were needed as a calibration line. Furthermore, the πD(3p-1s) transition energy was measured at different pressures in the target gas cell to clarify whether X-ray transitions from molecular states occur. If radiative de-excitation contributes, one expects a density dependence of the X-ray energy, because the formation rate depends on the density. In that case the transition energy of the isolated system must be obtained from extrapolation to zero density.

Chapter 2 deals with the formation of exotic atoms and the atomic cascade, in particular exotic hydrogen, preceding the measured X-ray transition. The influence of cascade processes on the transition energy and the line shape is discussed. In chapter 3 the relations of the hadronic effects as measured in pionic hydrogen and deuterium to quantities of the pion nucleon interaction are presented. The principle and the theoretical background of the high resolution Bragg crystal spectrometer are outlined in chapter 4. Furthermore, the hardware and the constituting various experimental setups are introduced. Chapter 5 gives an overview of the performed measurements. The analysis is described in chapter 6 together with the methods used to extract the quantities of interest. The final results are presented and compared to earlier measurements and theoretical predictions in chapter 7. The document closes by summarizing the work and giving a brief outlook with chapter 8.

Chapter 2

Formation and cascade of pionic atoms

2.1 Formation of exotic atoms

Exotic atoms are formed by capturing heavy negatively charged particles like muons, pions, kaons or antiprotons into the Coulomb field of nuclei. The binding energies E_n, which are given in leading order by the Bohr formula, are proportional to the reduced mass μ_{red} of captured particle and nucleus $A(Z,N)$:

$$E_n = \frac{\mu_{red} c^2 \alpha^2 Z^2}{2n^2}. \tag{2.1}$$

Here α denotes the fine structure constant, Z the nuclear charge and n the principal quantum number. Therefore, the transition energies in exotic atoms are increased approximately by a factor M_x/m_e, the mass ratio of the captured particle M_x and the electron m_e. The Bohr radii r_B and with them the expectation values of the orbit radii $\langle r_n \rangle$ are proportional to $1/\mu_{red}$:

$$\begin{aligned} r_B &= \frac{\hbar c}{\mu_{red} c^2 \alpha Z}, & (2.2) \\ \langle r_n \rangle &= r_B \cdot [3n^2 - l(l+1)/2]. & (2.3) \end{aligned}$$

In the last equation l is the angular momentum. It can be seen, that even for light particles like muons and pions such atoms reach nuclear dimensions for low-lying states and, therefore, allow for investigations of hadronic effects at threshold. To be captured in the Coulomb field the particle has to be slowed down to a kinetic energy of a few eV. The exotic atoms are then formed in highly excited states by electron emission at radii comparable to the outermost electron Bohr radius. The corresponding principal quantum number of this initial state is given by

$$n_i \approx \sqrt{\frac{M_x}{m_e}}. \tag{2.4}$$

Consequently, in the case of a hydrogen or deuterium target the particle is, in the simplest model, captured after ionization of the atom in a state overlapping largely with the 1s electron wave function. For pionic hydrogen this leads to an initial principle quantum number $n_i \approx 15$. Furthermore, the initial conditions of the exotic atom depend on the angular momentum quantum number l and the kinetic energy T. For the angular momentum quantum number mostly a modified statistical distribution is used to approximate the initial population of the l-states, which reads

$$P_l \propto (2l+1)\, e^{\alpha l}, \tag{2.5}$$

with the parameter α fitted to the X-ray line yields and usually with a modulus less than 0.2 [22]. The initial kinetic energy of the exotic atom is assumed to follow a Maxwell distribution

$$w(T_i) = 3\sqrt{\frac{3T_i}{2\pi T_0}}\, exp\left(-\frac{3T_i}{2\pi T_0}\right), \tag{2.6}$$

with T_0=0.5 eV [23].

After the formation of the exotic atom in a highly excited state a de-excitation cascade starts. For exotic atoms with $Z > 2$ this cascade is in the upper part dominated by internal Auger effect and in the lower part by radiative decay, due to the different energy dependence of this two leading de-excitation mechanisms. The cascade time decreases quickly with increasing Z as the radiative width strongly depends on the nuclear charge ($\Gamma_x \propto Z^4$). For hydrogen isotopes, however, the interaction with the environment, i.e., collisional processes become dominant. The different processes and the evolution of the cascade for this case are described in the next section. For descriptions of capture and atomic cascade see also [23, 24].

2.2 Cascade in pionic hydrogen and deuterium

2.2.1 Cascade processes

The exotic hydrogen isotopes are electrically neutral and small on the atomic scale, by which they take an exceptional position compared to all other exotic atoms. The electrical neutrality enables approaches to surrounding nuclei close enough to experience the influence of their Coulomb potential, leading to various processes dominating the cascade in the upper and the medium part. These collisional processes with cross sections of geometrical order, i.e., of about the size of the exotic atom $\sigma_{coll} \approx \pi \langle r_n \rangle^2$, are

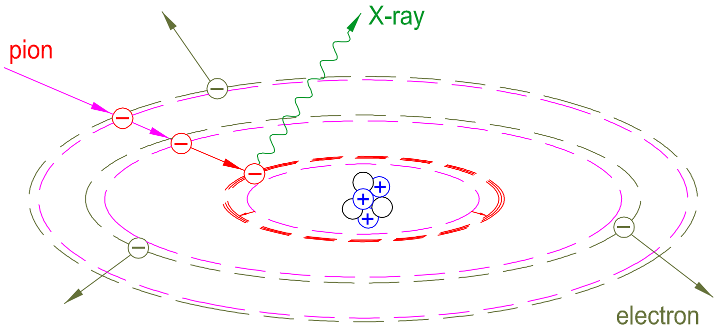

Figure 2.1: *Schematic drawing of a pionic atom. After the pion is captured in a high-lying atomic state a de-excitation cascade starts. The electrons are emitted if internal Auger effect is possible. Radiative de-excitation dominates in the lower part of the cascade. For low-lying atomic levels, the strong interaction causes an energy shift and broadening.*

most important for the evolution of the kinetic energy distribution during the cascade as they change the velocity v, decisive for the competition of internal and external processes, of the exotic atom significantly. The collision rate R is given by $R = \rho \cdot v \cdot \sigma_{coll}$, with ρ being the density. The different processes occurring are shortly described in the following and listed with their symbolic representation in Table 2.1.

Radiative de-excitation. In the radiative de-excitation process the transition energy release originating from Δn transitions is carried away by a photon. This process is non-collisional and, therefore, not environment dependent and follows the properties of electric-dipole transitions obeying the selection rule $\Delta l = \pm 1$. Transitions with $\Delta n = max$ are preferred.

Stark mixing. Due to the non-vanishing matrix element $\langle nlm \mid \mathbf{E} \mid nl'm' \rangle$ an electric field **E** mixes the atomic states of same principle quantum number n according to the selection rules $\Delta l = \pm 1$ and $\Delta m = 0$ when passing during collisions the Coulomb field of other target atoms inducing so called Stark transitions [25]. The large number of Stark transitions, transition rates are of the order $10^{11}/s$ (Fig. 2.4), between the l states leads to a statistical population in high n states. Because of the high probability of nuclear reactions in s states due to strong interaction the X-ray yields are strongly affected.

External Auger effect. If the pionic atom de-excites via the external Auger effect, neighboring molecules are ionized in collisions and the transition energy is mainly carried away by the emitted electron. As the condition that the energy of the Δn transition exceeds the binding energy of the electron must be fulfiled and $\Delta n = 1$ transitions are favored, Auger emission contributes mainly in the range $\Delta n \approx 6 - 10$, but there with significant rate [26, 27].

Process	Example
Radiative transitions	$(\pi^- D)_{nl} \rightarrow (\pi^- D)_{n',l-1} + \gamma$
Stark mixing	$(\pi^- D)_{nl} + D_2 \rightarrow (\pi^- D)_{nl'} + D_2^*$
External Auger effect	$(\pi^- D)_{nl} + D_2 \rightarrow (\pi^- D)_{n'l'} + D_2^+ + e^-$
Coulomb de-excitation	$(\pi^- D)_n + D_2 \rightarrow (\pi^- D)_{n-1} + D + D + kinetic\ energy$
Elastic scattering	$(\pi^- D)_{nl} + D_2 \rightarrow (\pi^- D)_{nl} + D_2^*$
Molecular formation	$(\pi^- D)_{nl} + D_2 \rightarrow [(\pi^- dd)d]ee$
Nuclear reactions	$(\pi^- D)_{n,l=0} \rightarrow nn,\ nn\gamma,\ nne^+e^-,\ nn\pi^0$
Weak decay	$\pi^- \rightarrow \mu^- + \bar{\nu}_\mu$

Table 2.1: *Listing of processes occurring during the atomic cascade of pionic deuterium.*

Coulomb de-excitation. Another de-excitation mechanism originating from collisions during the cascade are the so called Coulomb transitions. In this process the energy release from a de-excitation step Δn is converted into kinetic energy of the collision partners, leading to high kinetic energy gains for low lying transitions. Coulomb de-excitation was directly observed for the first time in the time-of-flight spectrum of monoenergetic neutrons from the charge exchange reaction at rest $\pi^- p \rightarrow \pi^0 n$ as a broadening [28]. The broadening turned out to be a superposition of several Doppler contributions corresponding to different de-excitation steps $n \rightarrow n'$ of the initial $\pi^- p$ system with Δn=1 transitions preferred, but also evidence was found for Δn=2 [29]. For that reason the Coulomb de-excitation can cause besides the strong interaction an additional line broadening of the X-ray transitions.

Elastic scattering. This collisional process contributes to the evolution of the cascade decreasing the velocity of the exotic atoms. It counteracts the acceleration of the system due to Coulomb de-excitation.

Molecular formation. Furthermore, it is expected that collisions between the pionic atoms lead to the formation of complex metastable molecules. This is known from experiments on muon-catalysed fusion where metastable hybrid molecules like $[(pp\mu)p]ee$ are formed from a μH atom and a H_2 molecule [30]. The molecules usually decay via Auger emission. A possible radiative decay is discussed in [31, 32, 33, 34].

Weak decay. If a weak decay of the pion, mainly in a muon and a antimuon neutrino, occurs, the cascade is terminated. This decay is found to be rare during the de-excitation cascade resulting from comparison of typical cascade times with the pion life time (Chap. 2.2.2).

Nuclear reactions. Finally, the nuclear reactions of the pion with the nucleus occur with highest probability from s states. The four possible reactions are listed in Table 2.1. A detailed description of the main processes can be found in Chapter 3.

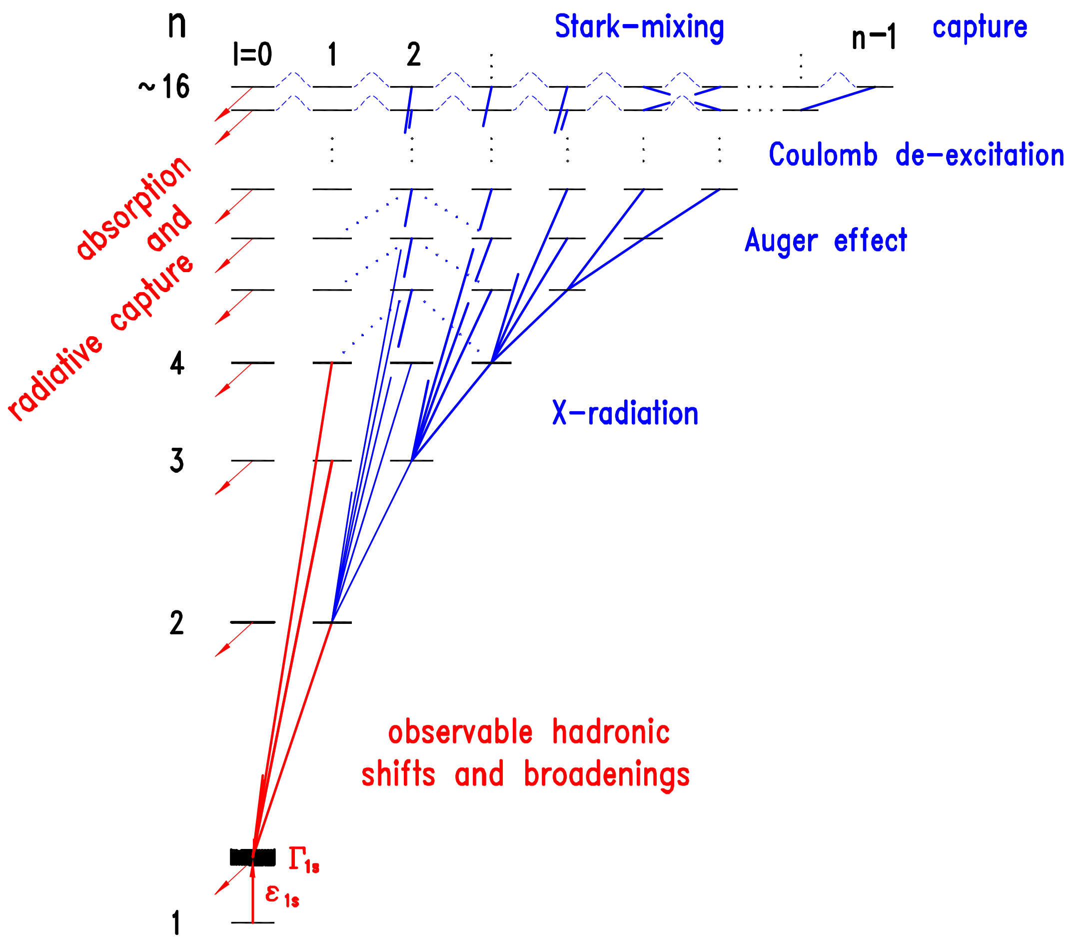

Figure 2.2: *Scheme of the atomic cascade in pionic deuterium. De-excitation in the upper part is dominated by Coulomb de-excitation as well as the intermediate part is dominated by the external Auger effect. Due to the hadronic interaction the ground state is shifted and broadened. The interaction in* πD *is repulsive and the shift* $\epsilon \equiv E_{X-ray} - E_{QED}$ *thus negative, i.e., the transition energy obtained from the experiment is smaller than the pure electromagnetic one calculated by the methods of QED.*

2.2.2 Cascade models

The theoretical description of the de-excitation cascade of a pionic atom including all the above mentioned processes in a comprehensive cascade model, including calculations of the various cross sections and thus leading to correct predictions of measurable quantities, the X-ray line yields and the Coulomb transition induced Doppler broadening, is a big challenge even nowadays.

The most recent evolutions of the so-called standard cascade model (SCM) gave a first approximate description of the atomic cascade in exotic hydrogen [35]. In SCM almost all relevant processes, namely radiative de-excitation, Stark mixing, Auger effect, Coulomb de-excitation as well as strong interaction effects were taken into account. However, it was assumed that the kinetic energy of the exotic system at the initial n state amounts to about 1 eV and that this kinetic energy is almost constant through the whole cascade. The (constant) kinetic energy was treated only as a tuning parameter when fitting the X-ray line yields. Within SCM X-ray line yields and the fraction of nuclear absorption are calculable reasonably, in particular the strong dependence on the density.

A new fact overcomes the assumption of a constant kinetic energy of the exotic system in SCM by neutron time-of-flight measurements [28]. In this measurements it was found that πH systems can have kinetic energy distributions of up to about 200 eV. Consequently, an extended standard cascade model (ESCM) had to be developed, which takes into account a state dependent kinetic energy distribution [36]. Besides the processes included in SCM, ESCM contains elastic scattering and the kinetic energy is treated as a time-dependent distribution and not as a tuning parameter of constant value. The collisional processes stand for acceleration and deceleration mechanisms competing during the cascade and changing constantly the kinetic energy distribution.

In the ESCM calculations by [23] the cascade is divided into two parts. For high n the processes are calculated with a classical-trajectory Monte Carlo model and for low and medium n quantum mechanically. In this model the calculations can be performed without any additional fitting parameters as used in earlier calculations leading straight forward to the evolution in kinetic energy.

For pionic hydrogen - up to now no calculations for pionic deuterium exist - in the upper part of the de-excitation cascade with $n > 8$ Coulomb de-excitation and Stark mixing are the dominant effects. In the intermediate state $8 \geq n \geq 7$ besides Stark mixing the external Auger emission peaks and in the lower part, $6 \geq n \geq 3$ radiative de-excitation dominates. As Stark mixing plays an important role through the whole cascade, nuclear absorption from s states also takes place through the whole cascade. Therefore, the strength of the Stark mixing determines essentially the X-ray line yields. Figure 2.3 shows calculated and measured πH and πD X-ray yields of various K transitions. It is clearly visible, that only for the lower transitions the yields are sufficient to achieve a reasonable count rate.

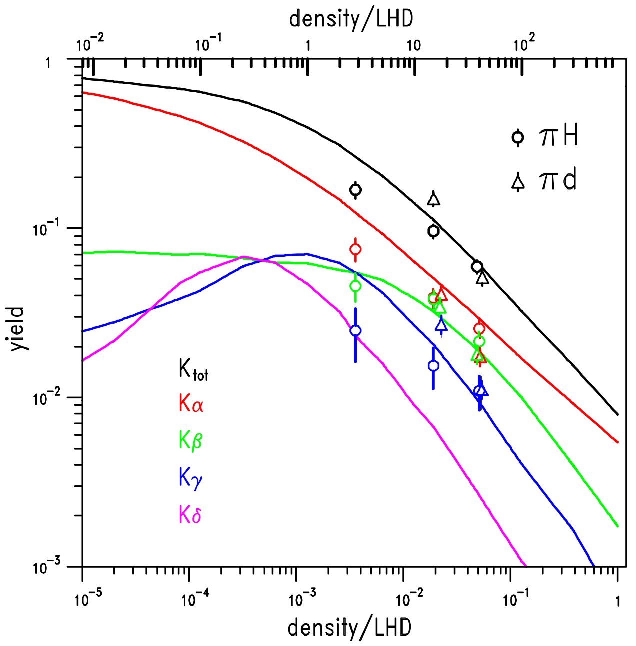

Figure 2.3: *K X-ray yields. The yields depend strongly on the density as Stark mixing increases strongly with increasing pressure, leading to absorption from s states before the X-ray transitions can occur. The figure is taken from [37] with ESCM calculations for hydrogen. The sketched in experimental values are from [38].*

The time scale on which the de-excitation cascade occurs, is in the order of picoseconds. Measurements of the cascade times for $\pi^- p$ in liquid hydrogen resulted in $\tau_{exp} = 1.2^{+1.2}_{-0.5}\, ps$ [39] and $\tau_{exp} = (2.3 \pm 0.6)\, ps$ [40]. This is extremely short compared to the pion lifetime of $\tau_{\pi^-} = 26\, ns$. Though radiative life times in highly excited states of pionic hydrogen atoms are in the nanosecond range, the collisional processes accelerate the cascade by order of magnitude for densities used in experiment.

The goal of the calculations using ESCM is a full ab initio description of the kinetic energy distribution at the instant of the X-ray emission. For this ambitious goal the cross sections for the different processes must be well known, that finally no tuning parameters enter the calculations. In Figure 2.4 the calculated rates at different steps of the cascade in hydrogen are shown.

2.2.3 Muonic hydrogen

The measurement of the 3p→1s transition in muonic hydrogen represents a test of the predictions of the ESCM [42, 43]. In this case the line shape is determined only by the spectrometer response function and the line broadening coming from cascade effects, since muons as leptons do not underlie strong interaction. For an accurate

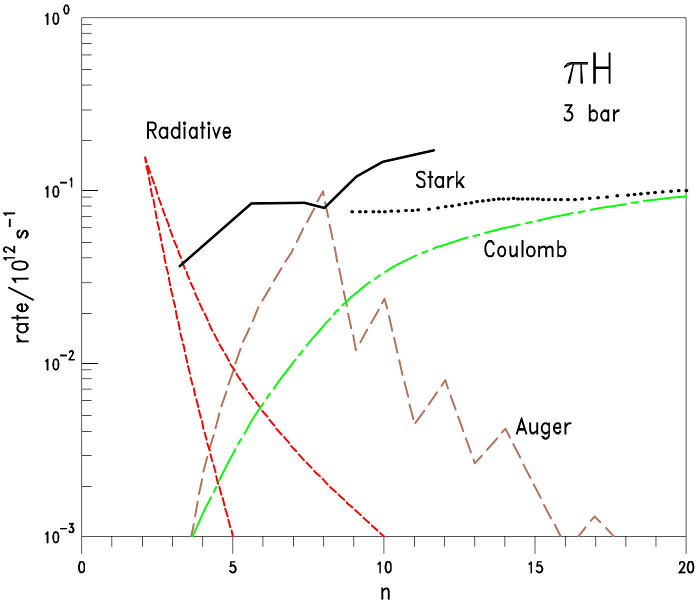

Figure 2.4: *Transition rates for pionic hydrogen. Isotope effects in the atomic cascade are not expected. The figure is adapted from [41]. Stark mixing is shown calculated within two different models. The radiative rates are for np→1s (right) and Δn=1 (left) transitions, respectively.*

calculation of the kinetic energy distributions the Coulomb de-excitation cross sections turned out to be very important. Latest results for cross sections inserted in ESCM calculations predict a kinetic energy distribution consisting of a main contribution of 55% in an energy range from 0 to 1 eV [44]. Additional contributions are predicted at the energies belonging to Coulomb de-excitations, most pronounced the 4-3 transition as well as small contributions continuously from 0 eV up to 90 eV. These calculations show reasonable agreement with the μH experiment.

With the information from the muonic hydrogen experiment a new calculation for the pionic hydrogen energy distribution at the instant of the 3p-1s transition was calculated. Assuming no significant isotope effects for the K X-ray lines (no absorption from l≥1 states), based on the fact, that no such effects were found for the L series (no annihilation from l≥2 states) in antiprotonic hydrogen and deuterium [45], the distribution can be scaled to the pionic deuterium energies. The scaled kinetic energy distribution is shown in Figure 2.5. It should be pointed out, that the good agreement of calculation and measurement in the case of muonic hydrogen does not necessarily ensures, that automatically a good description for pionic hydrogen is found.

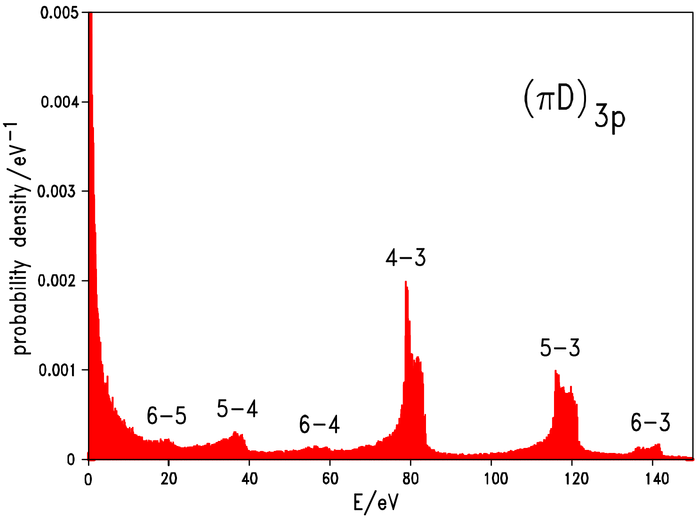

Figure 2.5: *Kinetic energy distribution of the π^-d atoms at the instant of the 3p-1s transition scaled from an ESCM prediction for π^-p [46]. The intensity in between the peaks originating from the Coulomb transitions is due to the system slowed down by elastic collisions.*

2.2.4 Modelling the kinetic energy distribution

The energy release in a Coulomb transition is given by

$$E_{n-n'} = \frac{\mu_{red}}{2}\left(\frac{1}{n'^2} - \frac{1}{n^2}\right). \tag{2.7}$$

The gain in kinetic energy by the πD atom in a two-body Coulomb de-excitation is thus given by

$$T_{\pi D} = \frac{m_d}{m_d + m_{\pi D}} E_{n-n'}, \tag{2.8}$$

with m_d being the deuterium mass and $m_{\pi D}$ the pionic deuterium mass. Energy gains due to Coulomb de-excitation are given in Table 2.2.

Model free approximations to the kinetic energy distributions can be done by using rectangular boxes adapted to their shape. The kinetic energy distribution leads to a velocity distribution of the target atoms responsible for a broadening of the X-ray transition line widths due to the Doppler effect. The distribution of the velocity distribution from a box-like kinetic energy distribution can be easily obtained. Assuming first a discrete kinetic energy T_0 being a δ-function $\delta(T-T_0)$ in the energy spectrum. This will then correspond to a rectangular box on the 1-dimensional velocity distribution extended from -v_0 to v_0 if $v_0 = \sqrt{2T_0/m}$ holds (Fig. 2.6).

transition	kinetic energy gain /eV
7→ 6	12.3
6→ 5	20.4
5→ 4	37.5
6→ 4	57.9
4→ 3	81.0
5→ 3	118.5

Table 2.2: *Possible energy gain due to Coulomb de-excitation.*

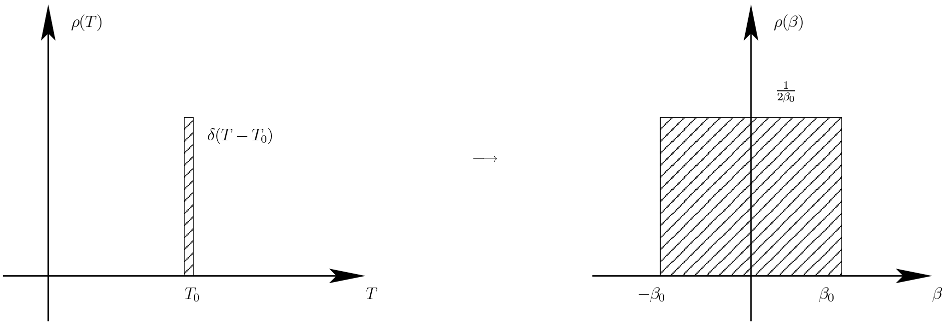

Figure 2.6: *Relation between a δ-like kinetic energy distribution and the resulting velocity distribution.*

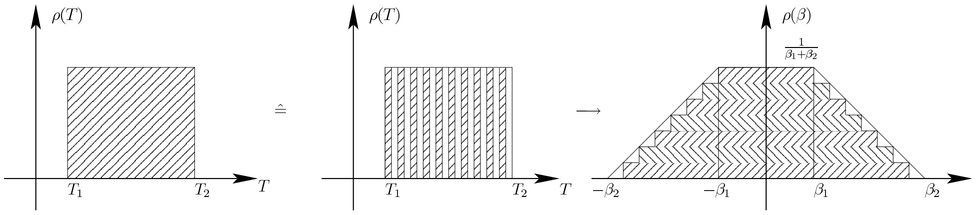

Figure 2.7: *Relation between a box like kinetic energy distribution and the resulting velocity distribution.*

Proceeding with a rectangular box limited by T_2 and T_1 one can obtain the velocity distribution by regarding the box as sum of discrete energy distribution. Each of them corresponds to a rectangular box on the velocity distribution summing up to a trapezoid structure (Fig. 2.7). More details can be found in [47].

Implementation in fitting routines allows decisive fits taking the energy distribution into account on the one hand but also be able to treat the number of boxes, their weights and limits as free parameters. In this way it is a model free approximation, which is not biased by distribution predictions and is in that way a tool to test predictions from cascade models.

Chapter 3

Pionic hydrogen and deuterium

3.1 Pion-nucleon interaction

The interaction of pions and nucleons within pionic hydrogen or deuterium atoms divides in scattering and absorption processes. Figures 3.1 and 3.2 show the LO processes.

For pionic hydrogen these are the elastic scattering $\pi^- p \rightarrow \pi^- p$, the charge exchange reaction $\pi^- p \rightarrow \pi^0 n$ and the radiative capture $\pi^- p \rightarrow \gamma n$. Elastic scattering leads to the shift of the ground state level as the charge exchange reaction is responsible for the hadronic level width. The Panofsky ratio between charge exchange and radiative capture amounts to $P_{\pi p} = 1.546 \pm 0.009$ [48].

In pionic deuterium as a three particle system besides single scattering also double scattering processes contribute to the level shift because of the smallness of the single scattering contributions (see Chap. 3.1.4). Whereas in πH the width is due to charge exchange, here, the level width arises in LO from true absorption $\pi^- d \rightarrow nn$, which is dominated by re-scattering processes where the pion scatters at one nucleon and is then absorbed at the second (Fig. 3.2). For the relative strength of true absorption and radiative capture $\pi^- d \rightarrow nn\gamma$ the ratio is $P_{\pi d} = 2.83 \pm 0.04$ [49]. Considering also internal pair conversion $\pi^- d \rightarrow nne^+e^-$ and charge exchange $\pi^- d \rightarrow nn\pi^0$ the

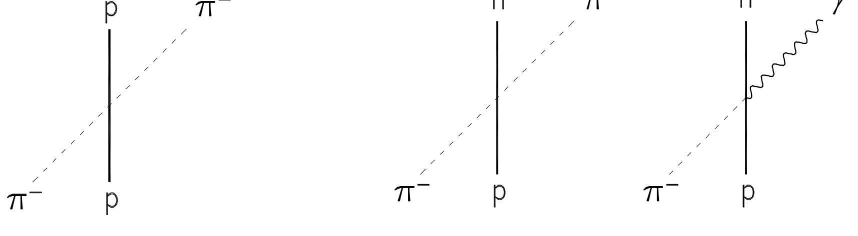

Figure 3.1: *Origin of the hadronic shift (left) and width (right) in pionic hydrogen in LO.*

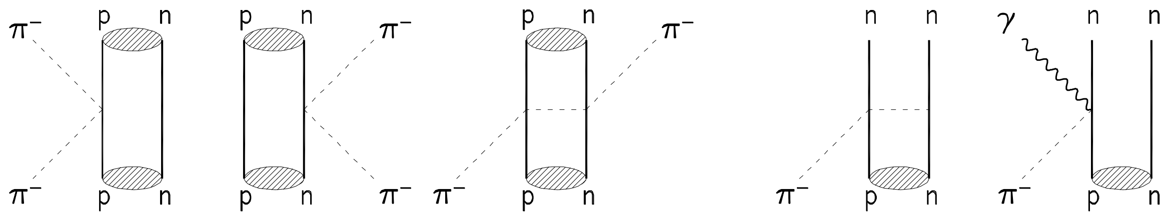

Figure 3.2: *Origin of the hadronic shift (left) and width (right) in pionic deuterium. The hatched blobs denote the deuterium bound state.*

relative strength of the true absorption channel to all other processes amounts to $P'_{\pi d} = 2.75 \pm 0.04$.

3.1.1 Scattering lengths

Pions and nucleons combine to isospin 1/2 or 3/2 systems. In the limit of isospin conservation, all πN processes at threshold are completely described by two amplitudes reducing to two real numbers and being identified with the s-wave scattering lengths. Therefore, the scattering lengths of the elastic scattering processes can be expressed by

$$a_{\pi^+p\to\pi^+p} = a_{3/2} \tag{3.1}$$

$$a_{\pi^-p\to\pi^-p} = \frac{1}{3}\big(2a_{1/2} + a_{3/2}\big) \tag{3.2}$$

$$a_{\pi^-p\to\pi^0n} = \frac{\sqrt{2}}{3}\big(a_{3/2} - a_{1/2}\big). \tag{3.3}$$

Conventionally the scattering lengths are stated in terms of the isoscalar (isospin-even) and isovector (isospin-odd) scattering lengths a^+ and a^- given by

$$a^+ = \frac{1}{2}(a_{\pi^+p\to\pi^+p} + a_{\pi^-p\to\pi^-p}) = \frac{1}{3}\big(a_{1/2} + 2a_{3/2}\big) \tag{3.4}$$

$$a^- = \frac{1}{2}(a_{\pi^-p\to\pi^-p} - a_{\pi^+p\to\pi^+p}) = \frac{1}{3}\big(a_{1/2} - a_{3/2}\big). \tag{3.5}$$

Assuming exact isospin symmetry the elastic channels are related to the charge exchange by

$$a_{\pi^-p\to\pi^-p} - a_{\pi^+p\to\pi^+p} = -\sqrt{2}a_{\pi^-p\to\pi^0n}. \tag{3.6}$$

It is a mandatory prediction of χPT, that in leading order a^+ vanishes and $a^- = \frac{m_\pi M}{m_\pi + M} \cdot \frac{1}{8\pi F_\pi^2} = -0.079/m_\pi$ [1, 50]. Deviations from these values manifest as higher order in the chiral expansion and are the subject to be tested from the data extracted for the πH and πD measurements.

3.1.2 Pionic atoms

The measured shift ϵ_{ns} and width Γ_{ns} in pionic atoms are related in first order to the complex pion-nucleus scattering length $a_{\pi A}$ by the classical Deser formula [51]. It reads

$$\epsilon_{ns} + i\,\Gamma_{ns}/2 = -4\frac{E_n}{r_B} \cdot \frac{a^{LO}_{\pi A}}{n}, \tag{3.7}$$

where E_n is the atomic state binding energy and r_B the Bohr radius of the πA system as given by the Bohr formula and Equation 2.2. Rewriting the Deser formula taking into account the Coulomb field by expressing the corrections in an expansion in the ratio scattering length over Bohr radius one gets the so-called Trueman formula [52]. In NLO it reads

$$\epsilon_{ns} + i\,\Gamma_{ns}/2 = -\frac{2\alpha^3 Z^3 \mu^2 c^4}{\hbar c} \cdot \frac{a^C_{\pi A}}{n^3}[1 - 2\alpha Z\frac{\mu c^2}{\hbar c}(ln\,\alpha - 1) \cdot a^C_{\pi A}], \tag{3.8}$$

where $a^C_{\pi A}$ is the scattering length in presence of the Coulomb field. Here the binding energy and the Bohr radius are explicitly written. The correction turns out to be small ($< 1\,\%$) for light pionic atoms.

3.1.3 Pionic hydrogen

In reality, isospin conservation holds only approximately. For charged pion-nucleon reactions isospin violation at the 1-2% level is predicted, which is caused both by electromagnetic- and strong-interaction effects. Therefore, corrections must be applied before extracting the isospin scattering lengths from pionic atom data. Applying such corrections the shift and width of the ground state in pionic hydrogen can be expressed still by Deser type formulae [53]

$$\begin{aligned}
\epsilon_{1s} &= -4\,\frac{E_B}{r_B}\,a_{\pi^- p\to\pi^- p}(1+\delta_\epsilon) && (3.9)\\
&= -4\,\frac{E_B}{r_B}\,(a^+ + a^-)(1+\delta_\epsilon) && (3.10)\\
\Gamma_{1s} &= 8\,\frac{q_0 E_B}{r_B}\left(1+\frac{1}{P}\right)[a_{\pi^- p\to\pi^0 n}(1+\delta_\Gamma)]^2 && (3.11)\\
&= 8\,\frac{q_0 E_B}{r_B}\left(1+\frac{1}{P}\right)[a^-(1+\delta_\Gamma)]^2. && (3.12)
\end{aligned}$$

In the latter $q_0 = 0.142 fm^{-1}$ is the cms momentum of the π^0. Usually, all corrections are condensed in the parameters δ_ϵ and δ_Γ. Their structure depends on the respective approach, as there are potential models [54], phenomenological approaches [55] or calculations within χPT [56, 57]. In these corrections usually also the Trueman correction is included, if considered, which makes various calculations not necessarily more transparent.

The value of the corrections $\delta_{\epsilon,\Gamma}$ amounts depending on the approach from (2±0.5)% (potential model) to (9±3)% (χPT). The corrections were controversially discussed. Though claimed to be very precise the potential model finally turned out to be incomplete [56]. In this work, the χPT approach is used because it is regarded to be complete up to the order considered.

The corrections contain low energy constants (LECs) called c_1, f_1 and f_2 already in next to leading order. These non-trivial LECs arise in the case of c_1 from strong isospin-breaking and in the case of f_1, f_2 from the electromagnetic interaction. For the sake of completeness, the correction terms ϵ containing the low energy constants from which the quantities δ_ϵ and δ_Γ can be obtained are given up to 2nd order. They read

$$\delta_\epsilon: \ \ \epsilon = \frac{m_p}{8\pi(m_p+m_\pi)F_\pi^2}(8c_1(m_{\pi^+}^2 - m_{\pi^0}^2) - 4e^2 f_1 - e^2 f_2) \ [58] \tag{3.13}$$

and

$$\delta_\Gamma: \ \ \epsilon = \frac{1}{16F_\pi^2 \pi m_\Sigma}(2e^2 f_2 F_\pi^2 m_p + g_A^2(m_{\pi^+}^2 - m_{\pi^0}^2)) \ [57]. \tag{3.14}$$

c_1 can be determined from the pion-nucleon phase shift, e.g., the KA86 analysis [58, 61]. f_2 can be extracted from the proton-neutron mass difference [56, 58]. The determination of f_1 from experimental data is ambiguous. Therefore, the uncertainty of f_1 dominates the error of the correction δ_ϵ. Considering the hadronic shift in pionic deuterium in the analysis gives access to f_1. Noteworthy, that the width does not depend on f_1 in NLO.

3.1.4 Pionic deuterium hadronic shift

In 2nd order (Eq. 3.8) the hadronic shift in pionic deuterium is related by Trueman's formula to the pion-deuteron scattering length $a_{\pi D}$ by the equation

$$\epsilon_{1s} = -\frac{2\alpha^3\mu^2c^4}{\hbar c}\Re\, a_{\pi D}\left[1 - \frac{2\alpha\mu c^2}{\hbar c}(ln\alpha - 1)\cdot\frac{\Re^2\, a_{\pi D} - \Im^2\, a_{\pi D}}{\Re\, a_{\pi D}}\right]. \tag{3.15}$$

The deviation from the Deser formula amounts less than 0.5%. Via the imaginary part in this equation an additional shift $\Delta\epsilon$ is induced from the hadronic width Γ. $\Re a_{\pi D}$

can be expressed in terms of the elementary pion-nucleon amplitudes a^+ and a^-.

$$\begin{aligned}
\Re\, a_{\pi D} &= S + D + ... \\
&= \tfrac{1+m_\pi/M}{1+m_\pi/M_d}\left(a_{\pi^- p} + a_{\pi^- n}\right) \\
&\quad +2\tfrac{(1+m_\pi/M)^2}{1+m_\pi/M_d}\left[\left(\tfrac{(a_{\pi^- p}+a_{\pi^- n})}{2}\right)^2 - 2\left(\tfrac{(a_{\pi^- p}-a_{\pi^- n})}{2}\right)^2\right] < 1/r > \\
&\quad +... \qquad\qquad (3.16)\\
&= \tfrac{1+m_\pi/M}{1+m_\pi/M_d}\, a^+ \\
&\quad +2\tfrac{(1+m_\pi/M)^2}{1+m_\pi/M_d}\left[\left(\tfrac{a^+}{2}\right)^2 - 2\left(\tfrac{a^-}{2}\right)^2\right] < 1/r > \\
&\quad +...
\end{aligned}$$

In this equation S denotes the single and D the double scattering term (Fig. 3.2, left). The leading order term is very small due to the nearly cancellation of $a_{\pi^- p\rightarrow\pi^- p}$ and $a_{\pi^- n\rightarrow\pi^- n}$. In the limit of isospin invariance, $a_{\pi^- p}$+ $a_{\pi^- n}$=a^+ and $a_{\pi^- n}$=$a_{\pi^+ p}$ holds.

Because of the chiral suppression of the LO, πD is a particular case, where 2nd order dominates over the 1st order. In the double scattering term the deuteron structure has to be taken into account denoted as $< 1/r >$, the deuteron wave function. It is stated in literature, that the corrections owing to the deuteron structure are well under control [59]. When introducing the expansion of the isospin-breaking contribution by means of χPT again correction terms containing the LECs c_1, f_1 and f_2 have to be added. The correction term $\Delta a_{\pi D}$ up to 2nd order reads [59]

$$\begin{aligned}
\Delta a_{\pi D} &= (4\pi(1+\mu/2))^{-1}(\delta\tau_p + \delta\tau_n) \qquad (3.17)\\
\delta\tau_p &= \tfrac{4(m_\pi^2 - m_{\pi^0}^2)}{F_\pi^2}c_1 - \tfrac{e^2}{2}(4f_1 + f_2) \\
\delta\tau_p &= \tfrac{4(m_\pi^2 - m_{\pi^0}^2)}{F_\pi^2}c_1 - \tfrac{e^2}{2}(4f_1 + f_2).
\end{aligned}$$

Besides the isospin breaking correction dispersive contributions are considered. An important one is due to virtual absorption, i.e., the pion is absorbed in a 1st stage and re-emitted in a 2nd one. This effect has been calculated to be ~6.5% [60].

3.1.5 Isospin πN scattering lengths

From pionic hydrogen and pionic deuterium experiments information concerning the elementary pion-nucleus scattering lengths can be extracted. In NLO we have

$$\begin{aligned}
\epsilon_{1s}^{\pi H} &= \epsilon_{1s}^{\pi H}(a^+, a^-, c_1, f_1, f_2) = \epsilon_{1s}^{\pi H}(a^+, a^-, f_1) \qquad (3.18)\\
\Gamma_{1s}^{\pi H} &= \epsilon_{1s}^{\pi H}(a^-, c_1, f_2) = \epsilon_{1s}^{\pi H}(a^-) \qquad (3.19)\\
\epsilon_{1s}^{\pi D} &= \epsilon_{1s}^{\pi D}(a^+, a^-, c_1, f_1, f_2) = \epsilon_{1s}^{\pi D}(a^+, a^-, f_1). \qquad (3.20)
\end{aligned}$$

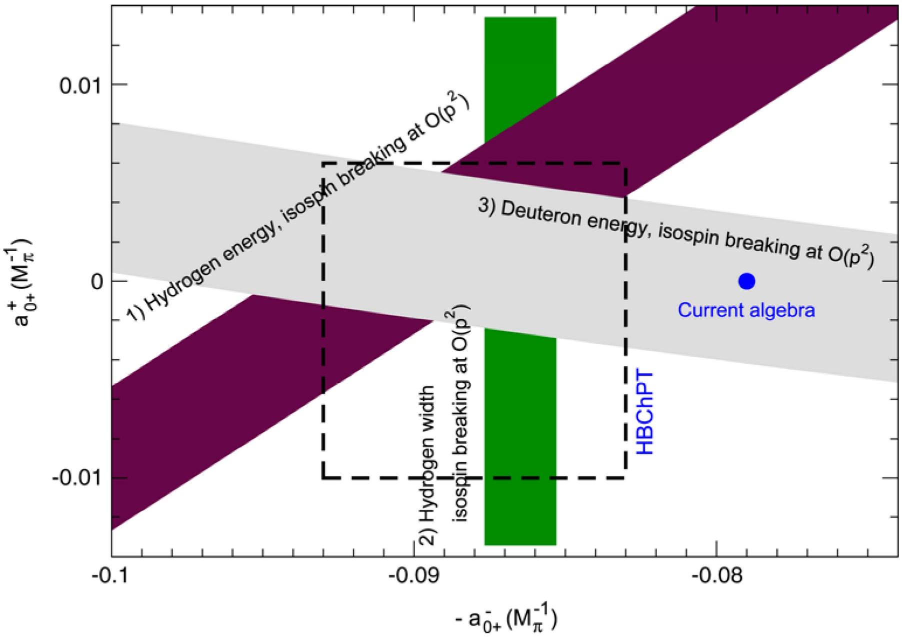

Figure 3.3: *Illustration of the connection between the scattering lengths of different access capabilities. See the text for a detailed description. The figure was taken from [62].*

Omitting the dependence on c_1 and f_2 as these values are determined with reasonable accuracy [61, 56] one ends up from the experimental data of pionic hydrogen and deuterium with three equations with three unknown quantities. This allows for a correlated fit to extract a^+, a^- and f_1. Figure 3.3 shows the determination of the scattering lengths a^+ and a^- from combined analysis of experimental data from πH [14] and πD [21]. The width of the bands 1 and 3 are mainly due to the uncertainty of f_1 and to minor part to c_1. That means, a more precise value for $\epsilon_{1s}^{\pi D}$ should allow for a decrease of the two bandwidths. After that, the three bands must still have a common intercept. Therefore the measured values induce the possibility of a decisive test of χPT calculations.

3.2 Pion absorption and production at threshold

3.2.1 Pionic deuterium hadronic width

The Trueman formula of the ground state width for pionic deuterium up to 2nd order reads

$$\Gamma_{1s} = -\frac{4\alpha^3\mu^2c^4}{\hbar c}\Im\, a_{\pi D}[1 - \frac{2\alpha\mu c^2}{\hbar c}(ln\alpha - 1)\cdot 2\Re\, a_{\pi D}]. \tag{3.21}$$

Also here an additional width $\Delta\Gamma$ is induced by the real part from the hadronic shift ϵ. The imaginary part of the pure hadronic πD scattering length can be obtained by

$$\Im\, a_{\pi D} = -\frac{\hbar c}{4\alpha^3\mu^2c^4}\frac{1}{1-\frac{2\alpha\mu c^2}{\hbar c}(ln\alpha-1)\cdot 2\Re\, a^C_{\pi D}}\cdot\left(\frac{\Gamma_{1s}}{2}\right). \tag{3.22}$$

In this equation the leading order result $a^C_{\pi D}$ obtained from the Deser formula is inserted into the second order term, which is of sufficient accuracy, as the corrections for πD amounts to less than 0.5%.

3.2.2 Pion production

As already mentioned, true absorption $\pi^- d \rightarrow nn$ is the origin of the hadronic ground state width. The ground state width of the πD system can be directly related to the reverse reaction, i.e., to π-production at threshold. The relation is mediated by the imaginary part of the πD scattering length, the optical theorem, charge invariance and detailed balance.

Optical theorem. The total cross section σ_{tot} is related to the imaginary part of the forward scattering amplitude by the optical theorem, which reads

$$\frac{4\pi}{p}\Im A(0) \;=\; \sigma_{tot}. \tag{3.23}$$

Herein p denotes the modulus of the CMS momentum for the scattering of two particles with masses m_a and m_b and total CMS energy $\sqrt{s}$ in Lorentz invariant notation $p = \lambda^{1/2}(s, m_a^2, m_b^2)/2\sqrt{s}$ with $\lambda(x,y,z) = x^2+y^2+z^2-2xy-2yz-2zx = (x-y-z)^2-4yz$ being the so called triangle function [63].

Charge invariance. Assuming isospin conservation the matrix elements of the reactions

$$\pi^- d \rightarrow nn \;\;\text{and}\;\; \pi^+ d \rightarrow pp \tag{3.24}$$

can be treated as equal since in both reactions the same transition of nucleon pairs occurs.

$$^3S_1(I=0) \rightarrow {}^3P_1(I=1) \tag{3.25}$$

Relating the cross sections Coulomb correction factors have to be taken into account as well as the slightly different phase factors [63].

$$\sigma_{\pi^- d\rightarrow nn}\cdot\frac{p_p}{\hat{C}_0^2} \;=\; \sigma_{\pi^+ d\rightarrow pp}\cdot\frac{p_n}{\tilde{C}_0^2} \tag{3.26}$$

Detailed balance. The exchange of final and initial state corresponds to time reversal. The ratio of the reaction cross sections is determined by the phase space.

The relative rate of pion production and absorption is given by [64]

$$\frac{\sigma_{pp\to\pi^+ d}}{\sigma_{\pi^+ d\to pp}} = \frac{3}{2}\cdot\left(\frac{p_\pi}{p_p}\right)^2 . \tag{3.27}$$

Parameterisation of the cross section in the well studied field of pion production in pp collisions at low energies is usually done by [64]

$$\sigma(pp\to\pi^+ d) = \alpha C_0^2\eta + \beta C_1^2\eta^3 + \dots . \tag{3.28}$$

Herein $\eta = k_{\pi D}/M_\pi$ is the reduced momentum of the pion in the πd rest frame. The parameters α, β... stand for s-wave, p-wave... production. The factors C_i take into account the reduction of the cross section due to Coulomb interaction. The leading order correction C_0^2 is expected to be about 30% [65] and an important source of uncertainty. At threshold ($\eta\to 0$) only the parameter α, representing pure s-wave production, contributes, while higher partial waves (β, ...) vanish.

Combining Equations 3.23, 3.26, 3.27 and restricting to s-waves in the parameterisation of the cross section (Eq. 3.28) the imaginary part of the $\pi^- d$ scattering length can be related to π^+ production as follows:

$$\begin{aligned}\Im a_{\pi d} &= \frac{p_\pi}{4\pi}\cdot\sigma_{\pi^- d\to nn}/\hat{C}_0^2\\ &= \frac{p_\pi}{4\pi}\cdot\sigma_{\pi^+ d\to pp}/\tilde{C}_0^2\cdot\frac{p_n}{p_p}\\ &= \frac{p_\pi}{4\pi}\cdot\frac{2}{3}\cdot\left(\frac{p_p}{p_\pi}\right)^2\cdot\sigma_{pp\to\pi^+ d}/C_0^2\cdot\frac{p_n}{p_p}\\ &= \frac{p_\pi}{6\pi}\cdot\left(\frac{p_p}{p_\pi}\right)^2\cdot\alpha\cdot\frac{p_\pi}{m_\pi}\cdot\frac{p_n}{p_p}\\ &= \frac{1}{6\pi}\cdot\frac{(p_p\cdot p_n)}{m_\pi}\cdot\alpha .\end{aligned} \tag{3.29}$$

The s-wave production parameter α obtained from pion production has to be corrected for radiative capture by means of the ratio $P'_{\pi d}$ before comparison with the value determined from πD Γ_{1s}.

$$\Im a_{\pi D} = \left(1+\frac{1}{P'_{\pi d}}\right)\cdot\frac{(p_p\cdot p_n)}{m_\pi}\cdot\alpha . \tag{3.30}$$

3.3 Width and shift of the πD(3p-1s) transition

The strong interaction broadening Γ and shift ϵ are most pronounced in the ground state. Aim of this work is the extraction of the hadronic ground state width and shift from measuring the 3p-1s X-ray transition. Because of the decreasing overlap of nucleus- and atomic wave function, Γ and ϵ decrease with increasing principal quantum number n. Assuming hydrogen-like wave functions, Γ and ϵ scale like [35]

$$\Gamma_{ns} = \frac{\Gamma_{1s}}{n^3}, \quad \epsilon_{ns} = \frac{\epsilon_{1s}}{n^3}. \tag{3.31}$$

Hadronic width

The natural width Γ_{3p-1s} of the πD X-ray transition between the two atomic levels is given by the sum of the level widths

$$\Gamma_{3p-1s} = \Gamma_{1s} + \Gamma_{3p}. \tag{3.32}$$

For the πD atom, the ground state width Γ_{1s} is given exclusively by the level life time due to the nuclear reactions (Tab. 2.1).

To the upper width several processes contribute:

$$\Gamma_{3p} = \Gamma_{3p}^{rad} + \Gamma_{3p}^{had} + \Gamma^{Stark} + \Gamma^{Auger}. \tag{3.33}$$

The electromagnetic dipole transition strength Γ_{3p}^{rad}, calculable from QED, and possibly a p-wave πD interaction Γ_{3p}^{had} occur even in an isolated system. Γ_{3p}^{had} can be estimated from the πD scattering volume $a_{\pi D}^{l=1}$ from the Trueman formula [66] for exotic atom p states. It relates the complex scattering volume to the atomic np level width and shift, where the width (shift) is given by imaginary (real) part of the expression.

Γ^{Stark} and Γ^{Auger} are collision induced effects. Γ^{Auger} can be neglected, because the presence of an electron is very unlikely in the neutral πD system. Γ^{Stark} is due to the s-p level mixing (Stark-mixing), which induces a hadronic part originating from 3s-level absorption. The magnitude depends on the 3s-3p level splitting and Γ_{3s}. In the weak mixing limit is $\Gamma^{Stark} = \mid a \mid^2 \Gamma_{3s}$ [67]. The mixing parameter a is given by $a = \frac{\langle 3p|\mathbf{E}|3s\rangle}{\Delta E}$ with $\langle 3p \mid \mathbf{E} \mid 3s\rangle \approx \omega^{Stark}$ (Fig. 2.4) and $\Delta E_{3s-3p} \approx \epsilon_{3s} = \epsilon_{1s}/27$. Also this contribution is found to be too small to contribute to the line width at the level of the experimental precision. The contributions to the line width are summarised in Table 3.1.

Therefore, the only sizeable broadening of the X-ray line shape in addition to the hadronic ground state width Γ_{1s} stems from the Doppler broadening induced by Coulomb de-excitation and modified by collisions in between the de-excitation steps (Tab. 2.2). According to the discussion in Chapter 2.2.4, the line shape can be approximated by the sum of individual Doppler contributions convoluted with the natural line shape given by Γ_{1s}:

$$\Gamma_{3p-1s} \approx \Gamma_{1s} \otimes \sum D_i. \tag{3.34}$$

In the experiment this line shape is convoluted in addition with the resolution function of the spectrometer.

width origin	$\Delta\Gamma$ /meV	reference
Γ_{1s}^{had}	1194	previous exp. [21]
Γ_{3p}^{had}	0.008	scattering volume [66], scaling [68]
Γ_{3p}^{rad}	0.028	QED [69]
Γ_{3p}^{Stark}	0.1	weak mixing [67]
Γ_{3p}^{Auger}	-	neglected

Table 3.1: *Approximations of contributions to the (3p-1s) X-ray line width.*

Hadronic shift

In the case of the shift, again environmental effects must be considered. From theoretical considerations the hadronic shift ϵ scales in the same way as the hadronic width. Possible contributions add up to

$$\epsilon_{3p-1s} \approx \epsilon_{1s}^{had} + \epsilon_{3p}^{had} + \epsilon^{Stark} + \epsilon^{e^- screen.} + \epsilon^{mf}. \tag{3.35}$$

The shift due to electron screening $\epsilon_{e^- screen.}$ is mentioned here only for the sake of completeness and can be neglected as well as ϵ^{Stark} and ϵ_{3p}^{had}, being as small as Γ_{3p} for reasons given in the discussion of the width.

No clear information is available for a possible radiative de-excitation from molecules formed in πD and D$_2$ collisions. In theory, for μH and πH no, or at least only a small fraction of radiative de-excitations from molecules is predicted. Whereas this fraction should be increased for μD/πD and even dominate for μT/πT [34].

Molecular formations of the target gas can induce a additional shift ϵ_{mf}, if radiative transitions out of these molecular formations appear. The extracted hadronic shift would be falsified, as the πD(3-1) X-ray transitions out of molecules would be slightly changed to lower energies due to the shifted molecular energy levels compared to the atomic ones. As the origin of molecular formation are collisions between the πD atoms and D$_2$ molecules the relative number of formed complex molecules should depend on the target density. To test for possible contributions from transitions out of molecular states, it is necessary to measure the transition energy at different target densities. The hadronic shift reads now

$$\epsilon_{3p-1s} \approx (1-P)\epsilon_{1s} + P\epsilon_{mf}, \tag{3.36}$$

with P being the fraction of X-ray transitions out of molecular states.

Chapter 4

Experiment

The measurement of the hadronic width and shift in pionic deuterium requires ultra high resolution together with high precision in the energy determination. The best method for few keV X-rays to extract these quantities is a reflection-type crystal spectrometer. In this chapter at first the theoretical foundations of Bragg's law and the principle of a Bragg crystal spectrometer in Johann setup are outlined together with the most prominent corrections. Secondly, the setup of the highly sophisticated apparatus used for the measurement at the Paul Scherrer Institut, Switzerland, in summer 2006 is introduced in some detail. The chapter ends up with a description of the additional setups of supplementary experiments necessary for the data analysis done at the Institut für Kernphysik, Forschungszentrum Jülich, Germany.

4.1 Bragg refraction and crystal spectrometer

4.1.1 Bragg's law and dynamical theory

In 1912 W. Bragg discovered the law relating the wave length of an X-ray diffracted in a crystal with the refraction angle:

$$n\lambda = 2d \cdot sin\theta_B. \tag{4.1}$$

In this equation n denotes the order of reflection, λ the wave length of an incoming X-ray, d the spacing of the diffraction lattice planes and θ_B is called the Bragg angle (Fig. 4.1)[70]. This relation between refraction angle and wave length is used in spectroscopy to transform an energy in an angle measurement, using the relation $E = hc/\lambda$ with h being the Planck constant and c the speed of light in vacuum.

An important correction to Bragg's law to be taken into account is the index of refraction of the crystal material. For soft X-rays as they occur in this experiment, the refraction index μ is slightly smaller than 1 and is parametrised (neglecting absorption)

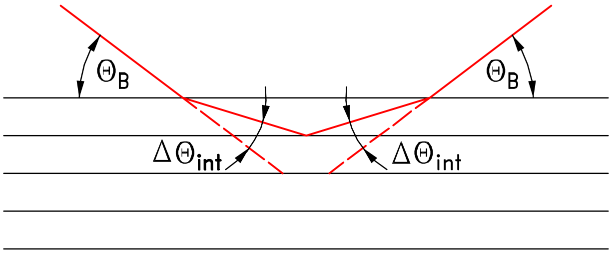

Figure 4.1: *Bragg refraction at a flat crystal. As the refraction index is smaller than 1, the Bragg angle is shifted to greater values.*

as

$$\mu = 1 - \delta, \tag{4.2}$$

with δ as a small positive number. Considering the refraction at the crystal surface due to Bragg's law and rewriting Bragg's law inside the crystal to be

$$n\lambda^{'} = 2d \cdot sin\theta_B^{'} \tag{4.3}$$

one obtains

$$\mu = \frac{\lambda}{\lambda^{'}} = \frac{cos\theta_B}{cos\theta_B^{'}} = 1 - \delta \tag{4.4}$$

leading to

$$n\lambda = 2d\left[1 - \frac{4d^2}{n^2} \cdot \frac{\delta}{\lambda^2}\right] \cdot sin\theta_B \tag{4.5}$$

as the modified Bragg law (see e.g. [71]). The correction is called index of refraction shift and is usually given as an offset angle $\Delta\Theta_{ind}$. It should alluded at this point, as it becomes important later on, that the size of the correction depends on the wave length, therefore, on the energy as well as on the order of refraction.

The properties of uniform crystals, so called ideal crystals, can be calculated within the dynamical theory of diffraction [72, 73], where a wave field is reflected from an infinite stack of atomic planes. A monoenergetic incoming wave is reflected into an angle range $\Delta\theta$. Conversely, this means that incoming waves fulfil the Bragg condition only within a small angular range which essentially represents the intrinsic resolution of the crystal material. The gross features of the diffraction pattern of a monoenergetic wave (Darwin curve) is shown in Figure 4.2 with a flat top region known as the region of total reflection. Due to the index refraction shift the reflectivity is not peaked at zero. The integrated intensity of the reflectivity curve is given in first order by

$$R_I \approx \frac{4}{3} P \cdot \Delta\theta, \tag{4.6}$$

with R_I being the integrated reflectivity, P the peak reflectivity as the maximum of the reflectivity curve and $\Delta\theta$ the FWHW of the curve. The reflectivity is reduced

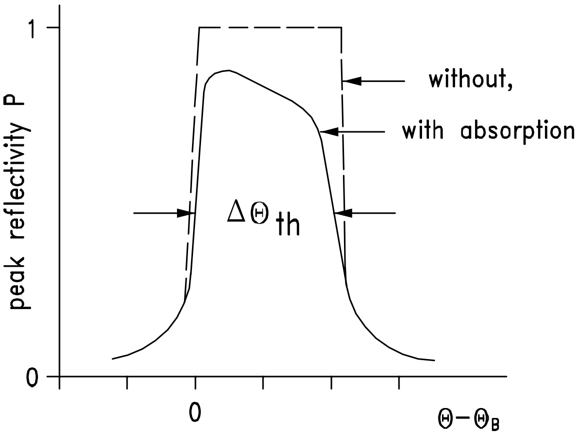

Figure 4.2: *Typical rocking curve for an ideal flat crystal.*

taking into account absorption processes in the crystal material. The proportion of these two values determines the order of the reduction inducing an asymmetric shape of the Darwin curve. Absorption is mainly due to the photoelectric effect in the few keV range. The extinction depth due to Bragg diffraction, i.e., the penetration depth, is measured perpendicular to the crystal surface and depends on the polarization of the incident beam. The total diffraction pattern from an unpolarized beam can be split up in

$$I = \frac{1}{2}(I_\sigma + I_\pi), \tag{4.7}$$

with I_σ and I_π being the diffraction pattern of the σ and π polarized beam. In the case of σ-polarization the electric field vector is perpendicular to the reflection plane, as in the case of π-polarization this vector is parallel to the reflection plane. For a given crystal material all these quantities can be calculated precisely within the frame work of dynamical diffraction theory by the program XOP [74]. Figure 6.21 left illustrates the situation.

The angular width of the rocking curve leads by Bragg's law to the energy resolution of the crystal

$$\frac{\Delta E}{E} = \frac{\Delta\lambda}{\lambda} = \frac{\Delta\Theta_{th}}{\tan\Theta_B}. \tag{4.8}$$

In high resolution X-ray spectroscopy in the few keV range silicon or quartz crystals are the only suitable choice. With such materials a relative resolution is achieved of

$$\frac{\Delta E}{E} \approx 10^{-4}. \tag{4.9}$$

4.1.2 Johann spectrometer

As described above the Bragg condition is only fulfilled for a small angular region leading to a low rate of reflected X-rays coming from a spatially extended source. To increase the efficiency, that means increasing the rate of reflected X-rays, focusing spectrometers with cylindrically or, like in this experiment, spherically bent crystals are used. Common are reflection-type spectrometers of the so called Johann geometry [75]. In this setup an extended source, a bent crystal and a detector are placed on the so-called Rowland circle (Fig. 4.3). The radius of the Rowland circle (R) is equal to half of the bending radius of the crystal R$_c$. The focusing condition for a beam hitting the crystal at the very center is

$$R = R_C \cdot sin\theta_B. \tag{4.10}$$

Using the Johann setup an extended source together with a large-area detector allows for a simultaneous measurement of an energy interval, given by the horizontal extension of source and/or detector. X-rays with different wave lengths are accepted from different places of the extended source and are focused to adjacent places on the detector. In that way the detector's position spectrum contains information about the energy differences of the outgoing X-rays. This relation can be expressed as equation of the local dispersion

$$\frac{dE}{dx} = \frac{E}{R \cdot sin\theta_B \cdot tan\theta_B}, \tag{4.11}$$

with the direction x of the local dispersion perpendicular to the axis crystal-detector (Fig. 4.3).

Usually the setup is modified such, that the extended source is placed about 20 % of the focal distance inside the Rowland circle. In this way, non uniformities of the source are washed out, because now not only X-rays from one narrow strip, but from a region of the source fulfil the Bragg condition. Placing the source outside the Rowland circle results in the same effect, but reduces the effective source width and, therefore, the size of the measurable energy interval.

The different radii of the crystal and the Rowland circle lead to a defocussing of the parts of the beam that are not reflected at the center of the crystal and causes a broadening of the measured X-ray line at the detector. From geometrical considerations it can be seen, that X-rays not hitting this central vertical of the crystal are always reflected to the high energy side, i.e., towards smaller Bragg angles. This shift is maximal at the edges of the crystal. At this points, assuming the total width of the crystal to be b, in the symmetry plane the so called Johann shift reads in leading order [76]

$$\Delta\Theta_J = \frac{1}{2}\left(\frac{b}{2R_C}\right)^2 \cot\Theta_B. \tag{4.12}$$

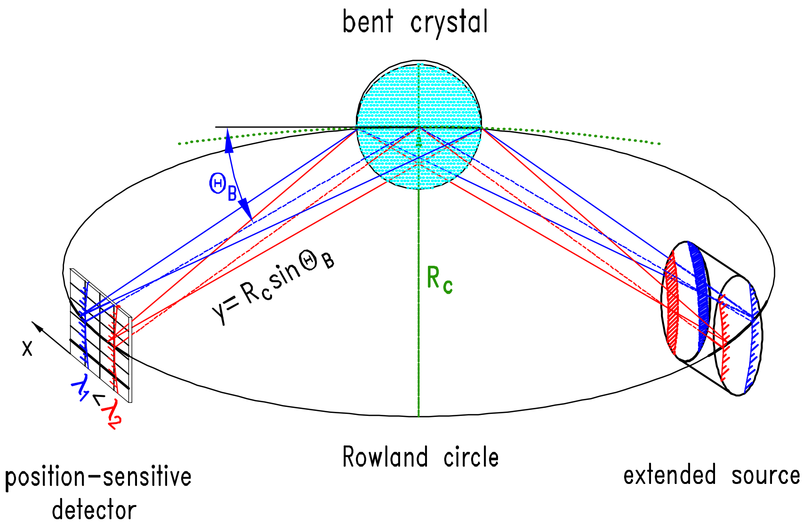

Figure 4.3: *Schematic drawing of a Bragg spectrometer in Johann setup. This setup together with an extended source allows for simultaneous measurement of a finite energy interval. Smaller wave lengths (higher energies) belong to smaller Bragg angles* Θ_B.

The Johann broadening can be tolerated if it is small compared to the crystal resolution, which is the case for a large crystal bending radius R_C. An aperture in front of the crystal restricting the crystal width can be used to limit the Johann broadening. Using a rectangular aperture the average shift is given in good approximation by integrating over the whole crystal surface to be

$$\Delta\Theta_{J-av.} \approx \frac{1}{3}\Delta\Theta_J. \tag{4.13}$$

Obviously this reduces the rate because the reflecting crystal area is directly proportional to the reflected intensity. For this reason one has to choose a compromise between Johann broadening and rate.

In principle one can avoid this geometrical aberration using the Johansson setup [77]. There the crystal is bent to a radius equal to two times the radius of the Rowland circle as it is the case in the Johann setup, but additionally the crystal surface is ground with the radius of the Rowland circle. In practice, this is realised for compact industrial spectrometers of moderate resolution. The production of such crystals for large bending radii of three meters was not necessary for this experiment because resolutions close to the theoretical limit are achievable also with the Johann setup.

The bending of the crystal not only in the horizontal but also in the vertical direction increases the efficiency of the spectrometer, because the additional vertical focusing reduces the reflection height and, hence, enlarges the hit density at the detector [78]. The crystal expansion in vertical direction leads to a curvature of the

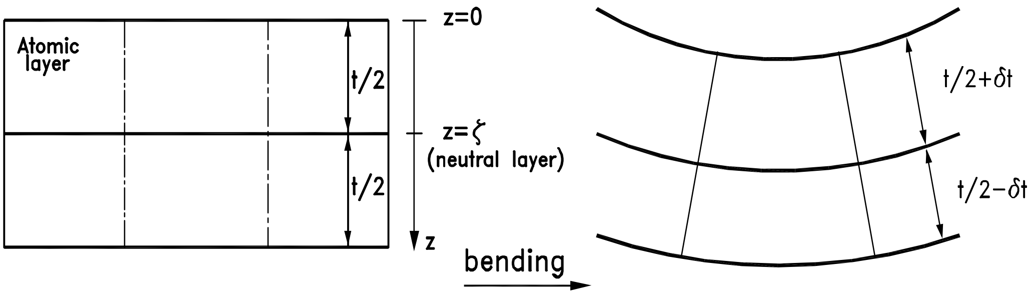

Figure 4.4: *As effect of the bending deformation the distance d between the crystal planes changes.*

reflection in direction to lower energies. In principle each point of the source, when fulfilling the Bragg condition, is reflected to a hyperbola on the detector. Therefore, the integral distribution at the detector emitted from an extended source comprises out of a multitude of superimposed hyperbola. A list of the corrections due to geometrical aberrations arising from the extended cylindrically bent crystal as well as from the extended source can be found in [76], which can be used as approximation also for spherically bent crystals with large bending radii. The imaging properties of spherically bent crystals are discussed in [78]. The overall curvature of the reflection has no negative consequences when using a two-dimensional position-sensitive detector.

Geometry implicates another important correction. A finite penetration depth seemingly changes the angle between the incident X-ray and the crystal planes increasing with the depth of the reflecting layer. With z being the penetration depth this correction reads [79, 80]

$$\Delta\Theta_p = -\frac{z}{R_C}\frac{1}{tan\theta_B}. \tag{4.14}$$

On the other hand bending leads to a depth dependent d-spacing of the crystal (Fig. 4.4), given by the elastic properties of the crystal material.

Defining ζ as the neutral layer to be at half of the thickness of the crystal, the lattice spacing decreases for $z \geq \zeta$ and increases for $z \leq \zeta$. The correction is given by

$$\Delta\Theta_{el} = -\frac{2\nu}{1-\nu}\frac{(z-\zeta)}{R} \cdot tan\theta_B, \tag{4.15}$$

where ν is the Poisson ratio of the crystal. For few keV X-rays, diffraction occurs close to the surface, i.e., the increase of d is close to the maximum.

A further correction to be taken into account stems from a possible crystal miscut. The beforehand reported relations implied, that the crystallographic planes were parallel to the crystal surface. If this is not the case, the focal condition

$$y = R_C \cdot sin\theta_B \tag{4.16}$$

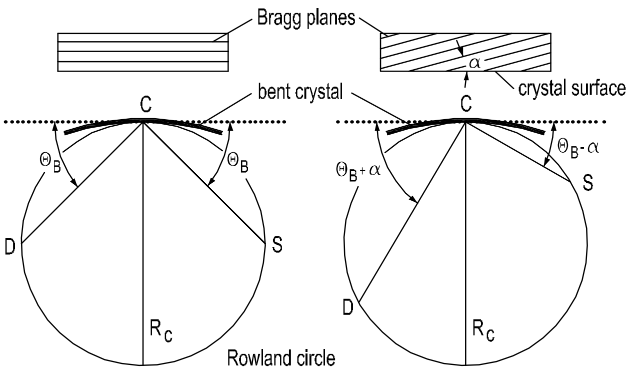

Figure 4.5: *An angle α (miscut) between the crystallographic planes and the crystal surface changes the focusing conditions asymmetrically for source and detector. The figure was taken from [43].*

changes to

$$y = R_C \cdot sin\theta_B \cdot cos(\alpha\ cos\phi) + R_C \cdot cos\theta_B \cdot sin(\alpha\ cos\phi). \tag{4.17}$$

In this equation α is the angle of the miscut and ϕ stands for the orientation of the crystal miscut pertained to the horizontal axis. Obviously an orientation of the miscut of 90°, resp. 270° does not change the focal distance, but influences the vertical position of the reflection with respect to the symmetry plane. This can be corrected by tilting the crystal.

Summarising, the angle measured by a Johann spectrometer using a bent crystal is given by

$$\Theta_{exp} = \Theta_{Bragg} \underset{>0}{+\Delta\Theta_{int}} \underset{<0}{+\Delta\Theta_P} \underset{<0}{+\Delta\Theta_{el}}. \tag{4.18}$$

4.2 Experimental Setup at PSI

As a matter of course high-resolution experiments suffer from low efficiencies. Therefore, pionic atom measurements must be set up at a facility delivering the highest pion flux achievable.

Paul Scherrer Institut

The experiment was set up at the high-intensity pion beam πE5 at the Paul Scherrer Institut. The institute operates the most developed meson factory used for fundamental nuclear and elementary particle physics as well as material research [81]. The pions are produced from a high-intensity proton beam.

Protons from an ion source are first accelerated by a Cockcroft-Walton cascade up to 870 keV which is the injection energy for the PSI Injector 2 cyclotron. This injector provides a high quality proton beam of 72 MeV protons. As a next step the protons are accelerated to 590 MeV in a Ring Cyclotron. The extracted proton current of up to 2.0 mA DC is guided to a target station called "Target E" at which the pions are produced. The target consists of a wheel with a 40 mm thick carbon/graphite layer and rotating with one Hz to prevent overheating.

Five secondary pion beam lines emerge from the "Target E" region. The shortest one is the πE5 beam line with a length of 10.4 m. Because of the short pion lifetime this beam line is the best choice for a low-energy pion beam. For the sake of completeness the main properties of the beam line are mentioned. The pion energy is adjustable in a range from 10-120 MeV/c. The maximum momentum acceptance amounts to 10 %. The momentum resolution was set here to 2 %. The spot size dimensions in the focus are 15 mm in horizontal and 20 mm in vertical direction with an angular divergence of 120 mrad and 450 mrad respectively. The divergence of the beam in vertical direction at the end of the beam line is an important setting for further processing of the pion beam. For the experiment a beam momentum of 112 MeV/c was used, which provides a pion rate of $4 \cdot 10^9$ π^-/s at a proton beam current of 1.6 mA. A graphical overview of the experimental hall at PSI is given in Figure 4.6.

Figure 4.7 shows a sketch of the setup indicating the most prominent components named. These components are described in the order following the X-ray path.

4.2.1 Cyclotron trap

The cyclotron trap, mounted to the pion beam line, allows for a high particle concentration in the center of the trap. It consists mainly out of two He-cooled superconducting coils which generate a strong bottle-like magnetic field. The symmetry axis is horizontal and perpendicular to the incoming beam. The field strength reaches 2.2 Tesla in the central plane at a current of 124 A.

The pions enter the trap through a thin Kapton foil and spiral due to the strong magnetic field in direction of the center. The vertical divergence of the beam ensures for the full beam height to reach a first thick degrader after about 1/4 of a revolution. This degrader slows the pion beam down to a beam momentum of about 82 MeV/c, which lies in the acceptance range of the trap for the pions to reach the center. A small plastic scintillator is integrated in the degrader for the purpose of beam optimisation and beam monitoring. As the lifetime of the pion is very short, additional wedge shaped plastic degraders are placed in the trap to shorten the time the pions need to reach the trap center. Due to the texture and placement of the degraders this happens within 1-2 turns. Figure 4.8 shows a view of the opened trap with the main inner parts indicated.

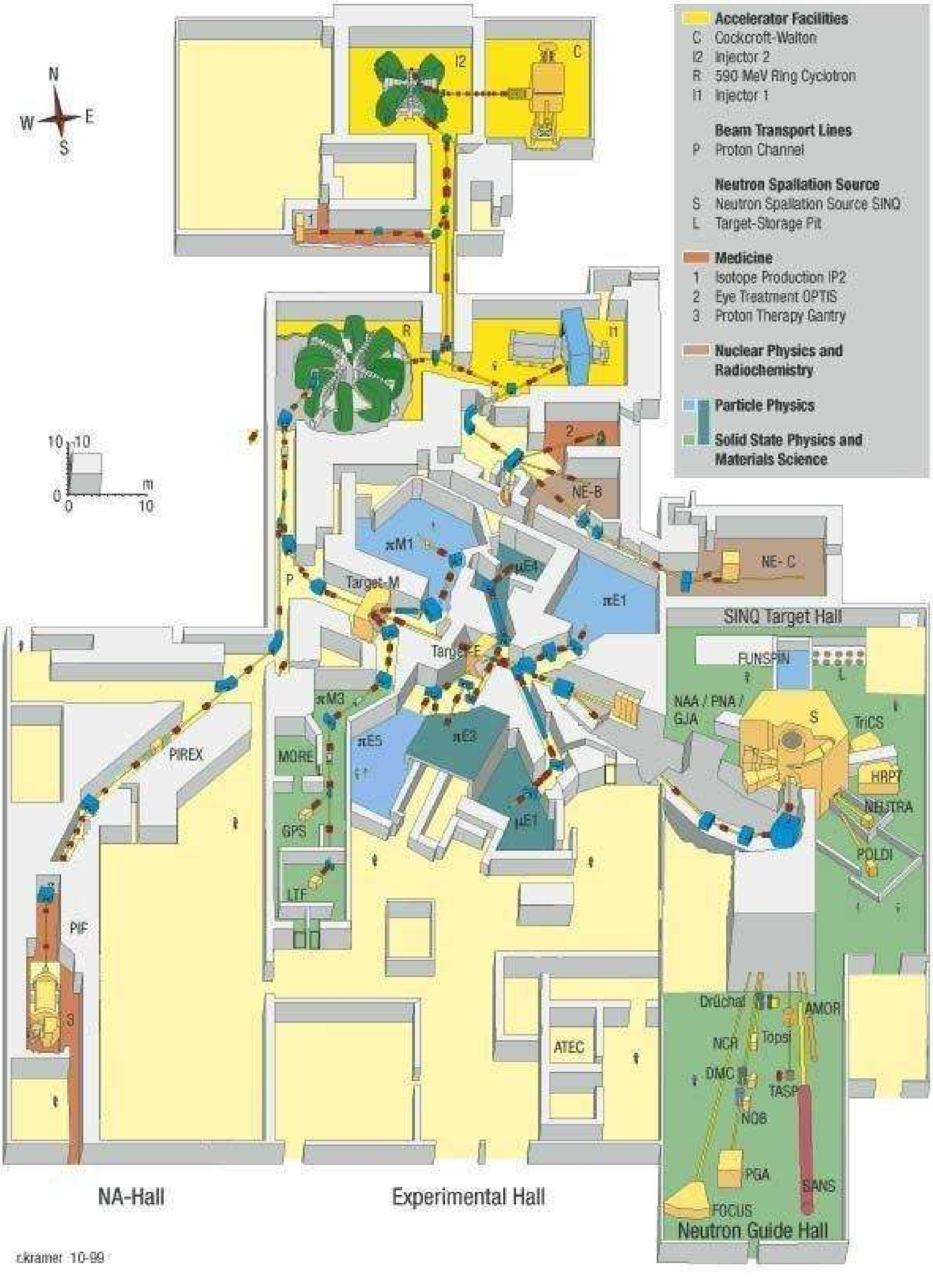

Figure 4.6: *Overview of the experimental hall at PSI.*

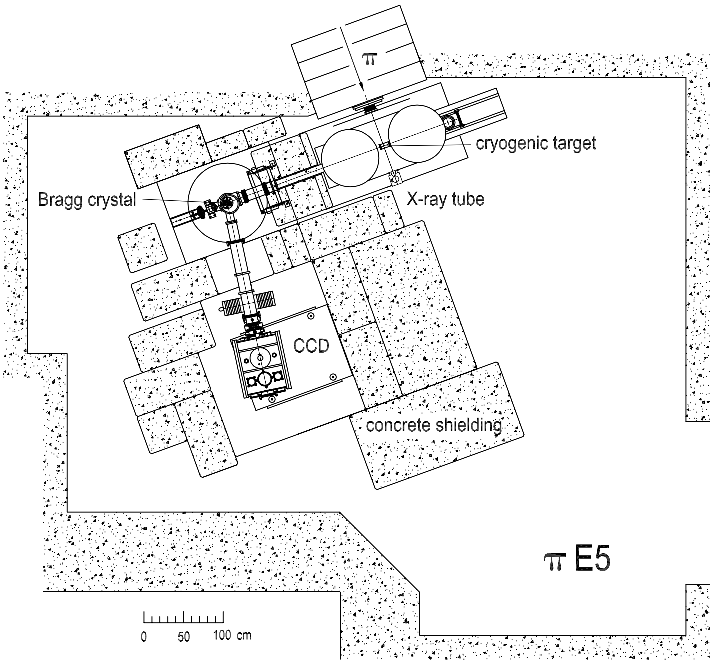

Figure 4.7: *Sketch of the setup at PSI.*

4.2.2 Cryogenic target

In the center of the trap the target cell filled with deuterium gas is placed. It has a cylindrical shape and the walls consists of Kapton. The constitutive dimensions are the inner length of 240 mm and a diameter of 60 mm. The Kapton of the girthed area is 50 μm thick and stabilized by two aluminium rings and three aluminium rods (Fig. 4.9). Through this area the pions enter the cell and form the pionic deuterium atoms. At the exit side a 7.5 μm thin Kapton foil stabilized by an aluminium support with a horizontal grating builds the window for the outgoing pionic deuterium X-rays. The other cylinder base, consisting of aluminium, was connected to an external copper cold finger to cool the target gas down to temperatures in the region of 20 K. The use of a cryogenic target is necessary, to be able to measure at high D_2 densities and simultaneously use a thin window not to absorb the pionic X-rays. As the stop efficiency amounts about 5 ‰/bar, one has to balance between target pressure and the X-ray line yield decreasing for higher pressures (Fig. 2.3). This design allowed to measure the X-radiation of the pionic deuterium densities equivalent to 3.3 bar, 10 bar and 20 bar at room temperature.

Furthermore, the Ga target used for energy calibration, consisting of a 25 mm × 20 mm GaAs plate, was mounted on the second base inside the cell (Fig. 4.10). The whole cell could be moved along its axial direction without breaking the vacuum by

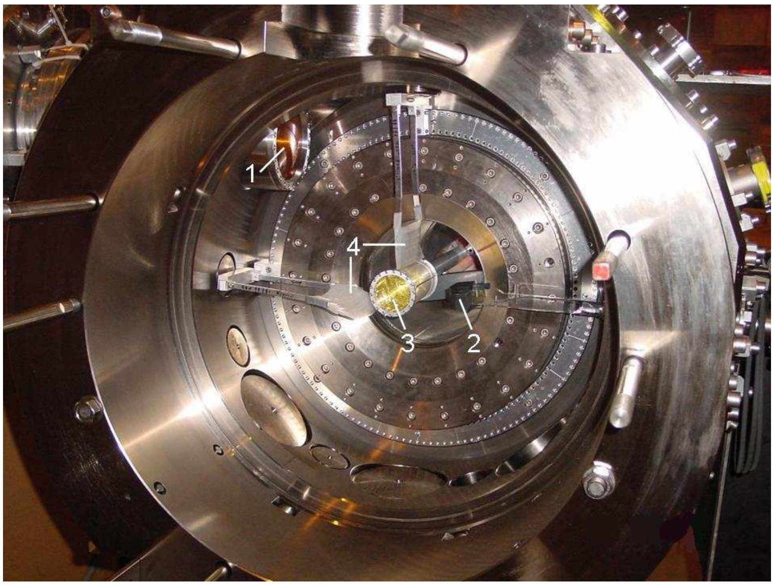

Figure 4.8: *Interior of the cyclotron trap with one magnet coil and its iron yoke removed. 1: Beam entrance window, 2: degrader with integrated scintillator, 3: plastic degraders, 4: target cell.*

about 25 cm by means of a metal bellow. More details about the cryogenic target can be found in [82].

4.2.3 Bragg crystal

The crystal used for this experiment was made of silicon manufactured in cooperation with Carl Zeiss, Inc., Oberkochen. The circular crystal plate is $30\,\mu$m thick and has a diameter of 100 mm. It is cut parallel to the (1 1 1) lattice plane and attached onto a cylindric glass lens. The distance of the lattice planes amounts $2d_{111}=(0.62712016\pm0.00000001)$ nm [83] and, hence, known with a relative accuracy of $\Delta d/d \approx 10^{-8}$. The lens is 30 mm thick, has a diameter of 120 mm and one of its bases is rubbed down into a spherical shape with a bending radius of 2982,4 mm. On this side the crystal is pressed and detained by adhesive forces to the glass lens surface adopting the bending. The crystal is mounted in a special holder which allows for rotation around the horizontal axis in order to adjust the Bragg reflection vertically (Fig. 4.12).

4.2.4 CCD detector

The detection system consists of an array of six charge coupled devices (CCDs) [84, 85]. CCDs allow for a high resolution in place and a good resolution in energy for low

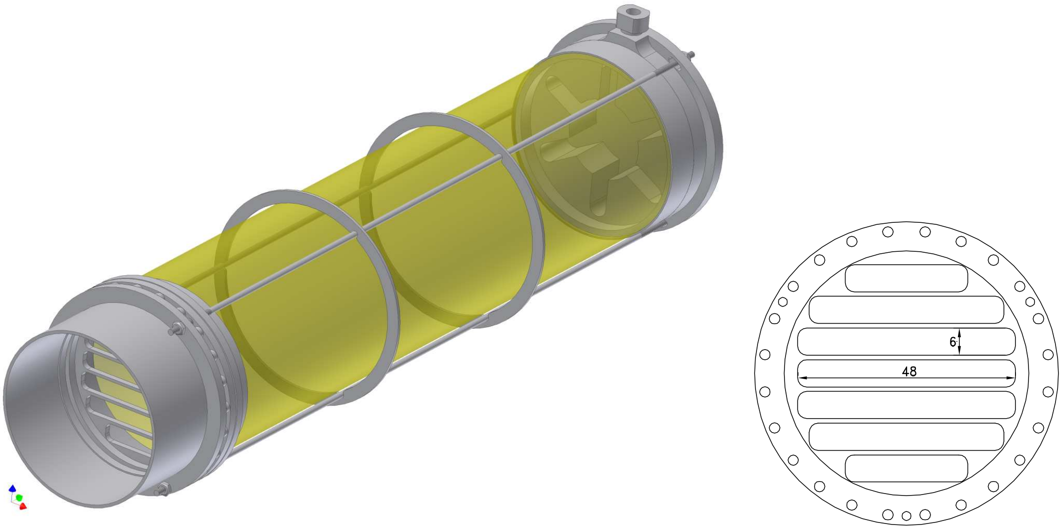

Figure 4.9: *Left: Scheme of the cryogenic target cell. The Ga target was mounted close to the aluminum plate at the rear end of the cylinder. Right: Front view of the target window consisting out of seven rectangles to stabilise the 7.5 µm Kapton exit window.*

Figure 4.10: *Left: View with the exit window removed into the cryogenic target cell. The solid GaAs target was mounted at the base. Right: Magnification of the GaAs target. The damage visible at the bottom right is discussed in Chapter 6.5.2.*

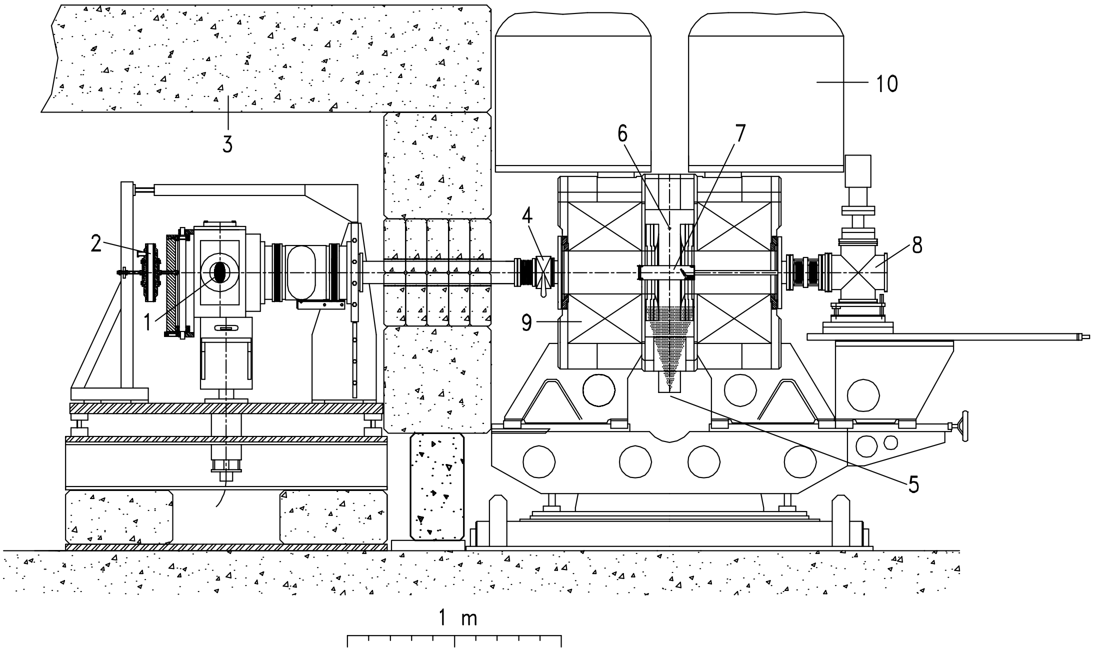

Figure 4.11: *Schematic view of connection of cyclotron trap and crystal chamber of the spectrometer. 1: Bragg crystal, 2: traction relaxation, 3: concrete shielding, 4: gate valve, 5: X-ray tube, 6: position of pion beam without B field, 7: cryogenic target cell including calibration target, 8: target cell support, 9: magnet, 10: LHe-dewar.*

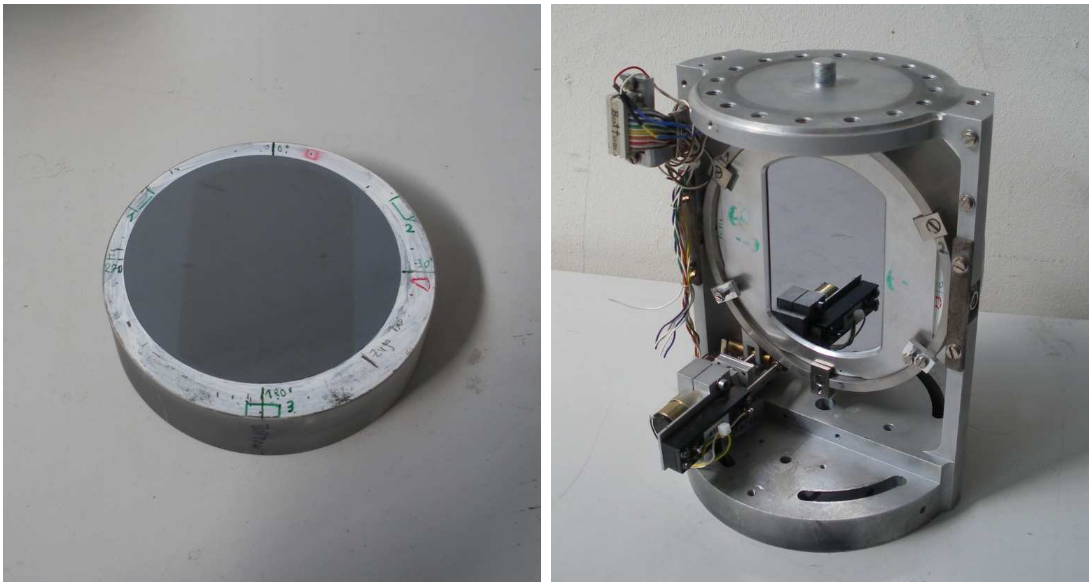

Figure 4.12: *Left: Silicon Bragg crystal "Z13". Right: Crystal support and crystal with an aperture of 60 mm width. On the bottom left a servo-motor with a linear potentiometer to adjust the crystal tilt.*

energy X-radiation. The quantum efficiency in the region of 3 keV is about 80-90%. For this reason CCDs are ideally suited as detector in a high resolution Bragg crystal spectrometer in the few keV range. In this measurement CCDs of type EEV-CCD22 were used [86], which were produced for the XMM-Newton Mission of ESA. Each device has a sensitive area of 24 mm × 24 mm consisting of 600 × 600 pixels, i.e, each pixel has a size of 40 μm × 40 μm. The depletion depth is about 30 μm.

The six CCDs are arranged in 2 columns mounted on a INVAR plane (Fig. 4.13). The thermal expansion of INVAR is extremely small in the temperature range from 150 K to 350 K and is almost similar to the thermal expansion of silicon from which the CCDs are made. This avoids tensions of the chips as they run cooled down to a temperature of 173 K to reduce thermally induced current. The cooling is done by means of a liquid nitrogen reservoir.

Ideally, the CCDs would be mounted perfectly aligned to each other, which is hardly possible. There are small gaps between the CCDs and the individual devices are slightly askewed and rotated to each other. Therefore, to perform high-precision measurements, the alignment must be accurately determined (Chap. 4.3.3).

The exposure time is 30 seconds. To prevent data losses during read out each chip has a storage area which allows to shift the complete image within 10 ms. The storage area is then read out during the next exposure time, which takes about 25 seconds. The whole detector is mounted inside the detector cryostat on a high-precision linear

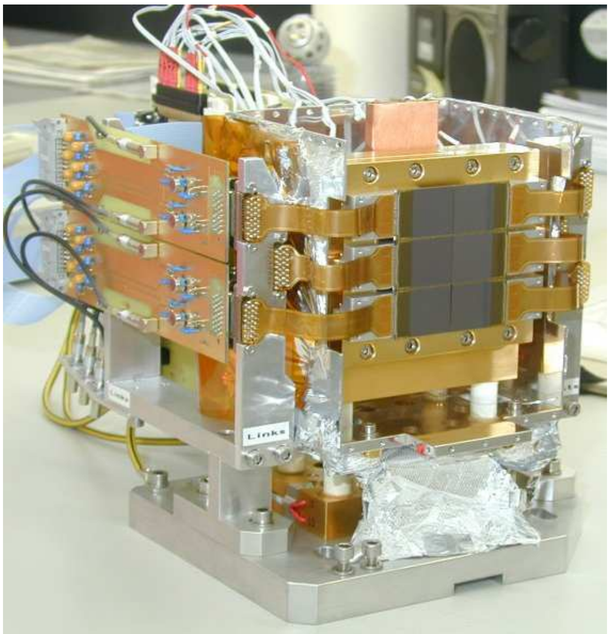

Figure 4.13: *Picture of the X-ray detector. At the front the array of six CCD detectors with horizontal readout. At the left side two of the preamplifiers are visible.*

table allowing for movements parallel to the direction crystal-detector to adjust the focal position without breaking the vacuum.

4.2.5 Crystal-detector connection

The connection between the crystal and the detector is essential for the spectrometer, as the relative orientation of crystal and detector measures the Bragg angle (Fig. 4.14). To reduce the mechanical stress between the crystal support and the detector cryostat a compensator is installed in front of the CCD cryostat allowing small movements in vertical direction, but is stiff in the horizontal direction. Consequently, rotation of the whole arm horizontally does not change the position of the reflection on the detector, i.e., the Bragg angle because detector and crystal move together. By this movement the acceptance of the crystal sweeps over the X-ray source (target scan).

4.2.6 Spectrometer efficiency

The spectrometer efficiency can be expressed as

$$N_x = N_\pi \cdot f_{stop} \cdot Y \cdot A_{tw} \cdot \left(\frac{\Delta\Omega_c}{4\pi}\right) \cdot P_c \cdot f_{det} \cdot \epsilon_E \cdot A_{dw}. \tag{4.19}$$

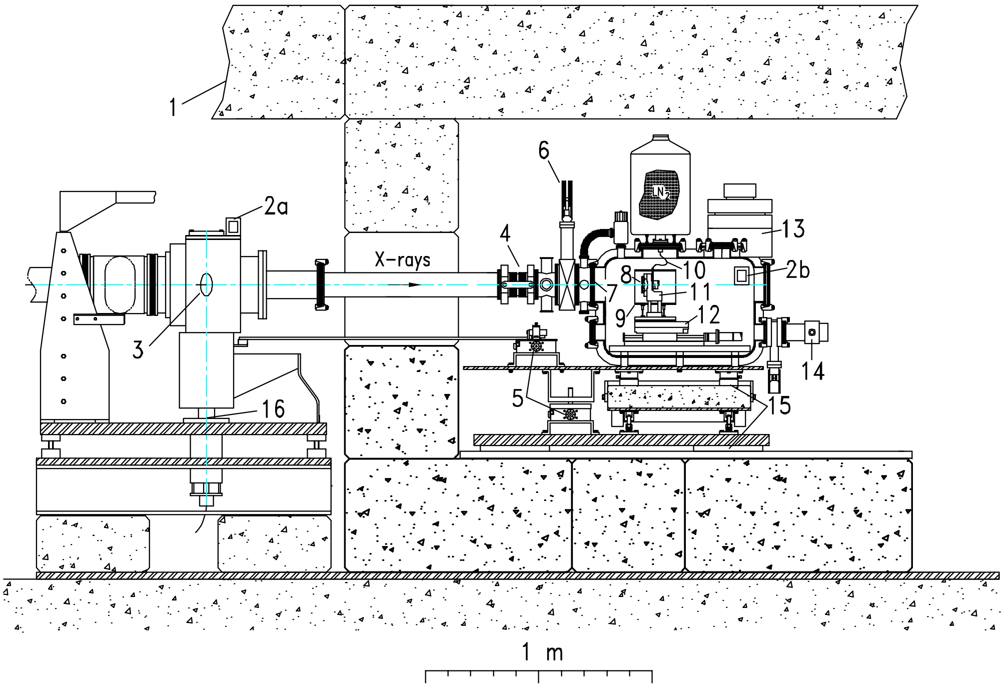

Figure 4.14: *Schematic view of the connection crystal chamber and X-ray detector. 1: concrete shielding, 2a and 2b: inclination sensors, 3: Bragg crystal, 4: compensator, 5: linear tables, 6: gate valve, 7: 5 μm Mylar window, 8: CCD array, 9: cold trap, 10: copper braid, 11: cold finger, 12: translation table, 13: detector electronics, 14: turbomolecular pump, 15: air cushion support, 16: crystal chamber support.*

The factors in this equation are the number of incoming pions N_π, the stop efficiency f_{stop} of the cyclotron trap, the yield Y of the measured X-ray transition, the solid angle $\Delta\Omega_c$ of the crystal with respect to the source, the peak reflectivity P_c, the ratio of reflected X-rays hitting the detector, f_{det} the detector efficiency for the measured energy interval ϵ_E and factors $A_{tw,dw}$ taking into account absorption at the target and detector windows.

4.2.7 Further installations

Vacuum installations

All parts of the setup are connected by vacuum tubes to prevent absorption of the few keV X-rays. For safety reasons, the system is divided into two independent parts. The detector chamber is separated from the other parts by a $5\,\mu$m thin Mylar foil. The detector chamber was evacuated down to a pressure of approx. 3×10^{-7} mbar with a turbomolecular pump and the remaining part down to less than 5×10^{-6} mbar with one turbomolecular pump at the crystal chamber and a cryopump at the cyclotron trap, respectively. Additionally, the cryogenic target acts as a pumping device.

The cyclotron trap and the detector chamber each can be detached by gate valves. The valve at the detector cryostat was equipped with a pneumatic actuator to automatically close in case of a vacuum break within 50 ms to protect the CCDs against destruction through ice building on the surface.

Spectrometer adjustment

The spectrometer adjustment and stabilisation is done by the combination of three linear tables with step motors, two angular encoders, one piezo crystal and one potentiometer. The encoders are placed at the bottom of the crystal chamber and work with an accuracy of 3-4 (arm) and 0.17 seconds of arc (crystal), respectively. The former measures the rotation of the with the chamber connected detector arm. Driving the detector cryostat and arm is performed by means of one of the linear tables placed underneath the detector cryostat setup and facilitated by air cushion supports. The step motors of the linear tables are able to set the angle with an accuracy of about 1 second of arc. The rotation of the Bragg crystal support is also done by such a linear table. On this one the piezo crystal is placed on top controlling movement and stability of the Bragg crystal with a precision as given by the latter high-precision angular encoder's accuracy. The piezo crystal has a full range of $50\,\mu$m corresponding to an angular range in the setup of about $\pm\,3$ seconds of arc. Furthermore, one linear table is placed in the detector cryostat carrying the CCDs to adjust the focal position. The position is controlled by means of the potentiometer. The controls of these parts are integrated in a LabView program to operate and inspect the adjustment [87].

Inclination sensors

To measure and verify the stability of the setup two high precision inclination sensors called Nivel20 from Leica Geosystems ware installed, one on top of the crystal chamber and one at the side of the detector cryostat. They record the inclination in x and y directions to the horizontal plane. The effective range of the sensors amounts to 1.5 mrad, having a resolution of 0.001 mrad and an accuracy of 0.001 mrad within a range of 0.3 mrad. In addition, these units measure and record the temperature.

Concrete shielding

An important point of the whole setup is an effective massive concrete shielding to reduce the background. At the production target for the pion beam also lots of other particles are produced, especially neutrons. Neutrons stem also from nuclear reactions in the deuterium or hydrogen gas. Pions, not stopped in the target, cause when hitting the trap walls, five to six neutrons after pion capture by the surrounding materials.

A concrete shielding of about 1 m thickness is sufficient to moderate the neutrons and absorb gamma rays from neutron capture. Nevertheless, to keep the background low, the vacuum tubes between cyclotron trap and crystal chamber as well as between crystal chamber and detector cryostat are build as small as possible and also surrounded by concrete (Fig 4.11, 4.14, 4.15).

X-ray tube

A conventional water-cooled X-ray tube with a chromium anode was mounted beneath the cyclotron trap to illuminate the GaAs calibration target. It was run with an anode voltage of 30 kV and a current of 30 mA. In this way the calibration transitions are excited from the broad Bremsstrahlungs spectrum.

4.3 Setups at Jülich

At the Institut für Kernphysik Jülich a crystal spectrometer of the same type as the one described before is in operation and used for atomic physics research. The section of the Bragg crystal and chamber is similar to the one used at PSI. The detector cryostat is smaller and equipped with 2 CCDs of the type CCD22 [86]. The entrance window consists of 0.8 mm beryllium. The chamber is mounted on a levitated arm connected with the crystal chamber. The cyclotron trap is replaced by an ordinary target chamber for solid or gaseous targets, which are excited by means of an X-ray tube equipped with a molybdenum anode. When working with gaseous targets, the target chamber is separated from the remaining setup by a 12.5 μm Kapton foil (Fig. 4.16).

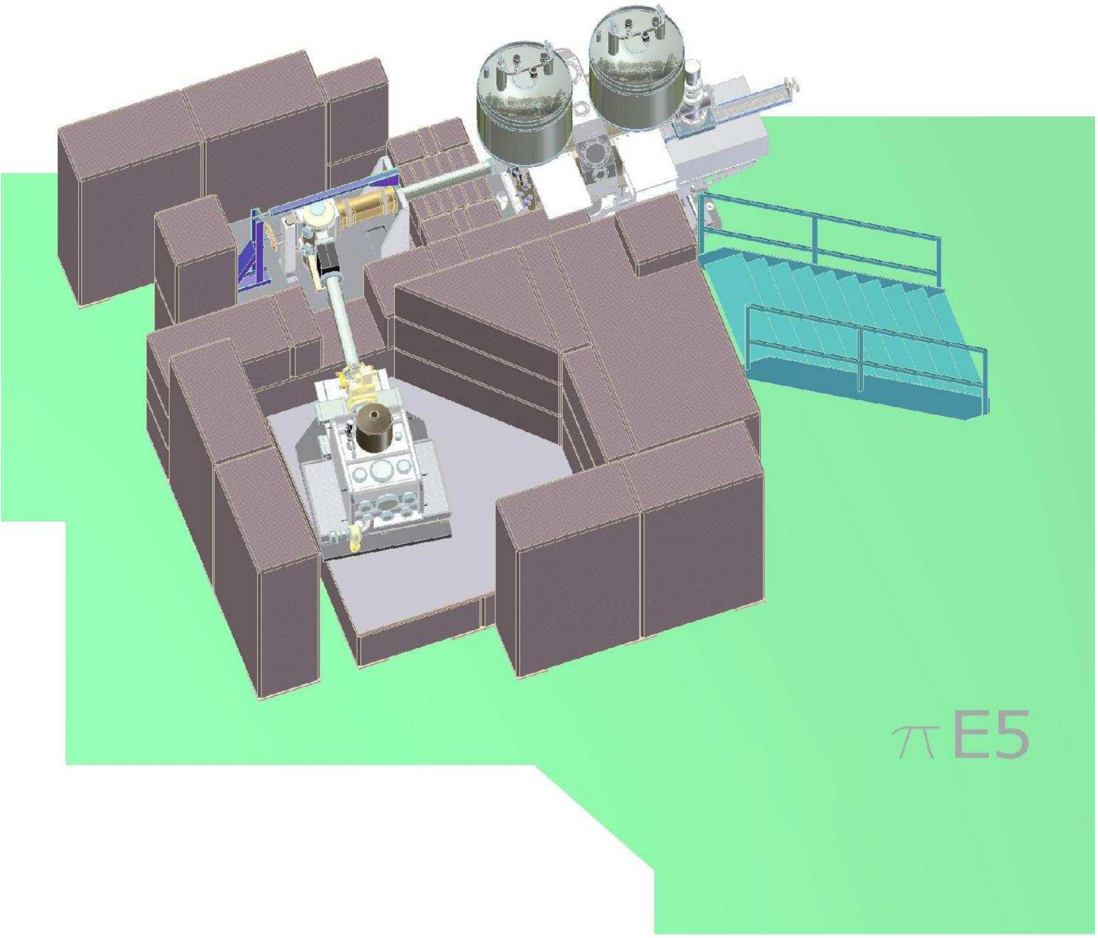

Figure 4.15: *Setup at PSI with concrete shielding between trap and crystal chamber. The concrete roof was omitted to allow free view on the whole setup.*

4.3.1 Ga Kα transition energy check

As calibration standard for the pionic deuterium X-rays the Ga Kα_2 line was used, emitted from a GaAs target. This measurement was performed as a consistency check for the Ga Kα transition energies because it was not known in the beginning, which had been used in the measurement for the tabulated value. Chemical shifts can change the transition energies noticeable.

The GaAs target as used at PSI was placed inside the target chamber filled with argon gas. The Bragg angle of the gallium and argon Kα X-rays differs by approximately two degrees. Measuring the two probes alternately it is necessary to adjust the angular setup for each measurement. Due to the levitated arm of the detector section this is possible in a reproducible manner.

4.3.2 X-ray tube characterisation

To analyse the calibration data with high precision the angular emission characteristics of the X-ray tube had to be measured to figure out whether the calibration target was uniformly illuminated, as contradictions arose in the gallium data taken at PSI. For more details see Chapter 6.5.2. For this purpose the set up of the Jülich spectrometer was modified. The X-ray tube used at PSI was mounted horizontally at the support of the crystal chamber (Fig. 4.17). Using the existing step motor and angular encoder the setup allows to measure the emission characteristic of the tube in a range of about 8 degree. By modifying the tube mounting, the range could be enlarged to nearly 25 degrees. To prevent overexposure of the detector due to the direct irradiation of the X-ray tube a 6 mm thick aluminium plate was placed in front of the detector. In addition, the X-ray tube was run with minimal anode current and voltage assuming that the angular distribution is independent from these parameters.

4.3.3 Characterisation of CCD array

The relative arrangement of the CCDs in the 3×2 array was measured precisely already in 2002 and 2005 [80, 88, 89]. As two chips had to be exchanged before the 2006 run a re-measurement became necessary. The setup was adopted from the 2005 measurement. A quartz wafer with an optical cross grating generated by electron-beam lithography manufactured by the Laboratory of Micro- and Nanotechnoloy of the PSI was placed 37.5 mm in front of the CCD detector array. The grating is composed of vertical and horizontal lines of 50 μm thickness and a distance of 2 mm from each other comprising a total grating area of 70 mm height and 40 mm width. The absolute accuracy of the line linearity of the grid is reported to be 0.15 μm in vertical and 0.05 μm in horizontal direction.

The wafer was illuminated by a point-like light source realized by a aperture with

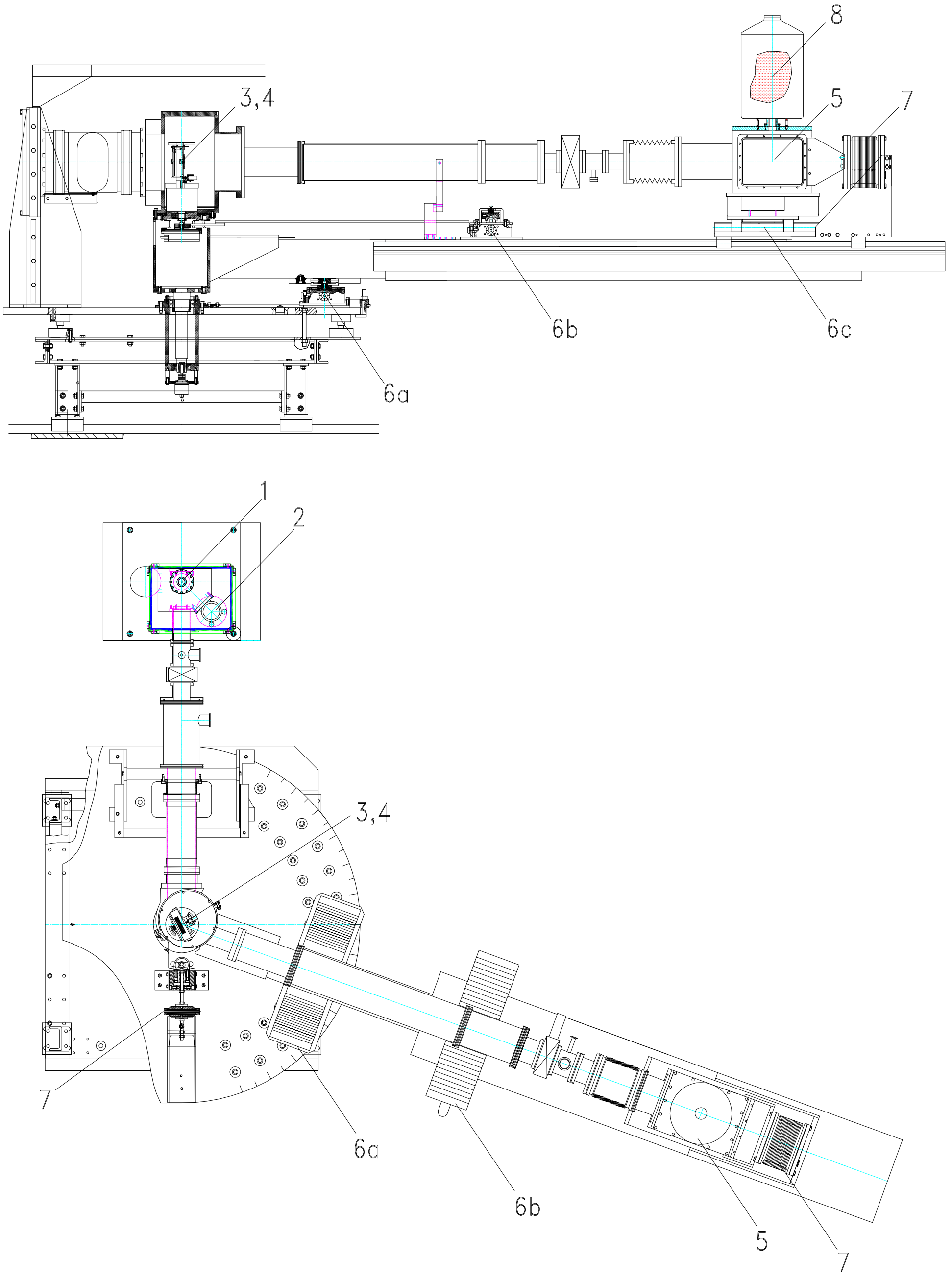

Figure 4.16: *Schematic setup of the Jülich spectrometer: top - side view of the detector arm, bottom - top view. 1: position of fluorescence target, 2: X-ray tube, 3,4: Bragg crystal, support, 5: detector cryostat, 6: linear tables for a) arm-, b) crystal and c) detector-movements, 7: traction relaxation, 8:* LN_2*-dewar.*

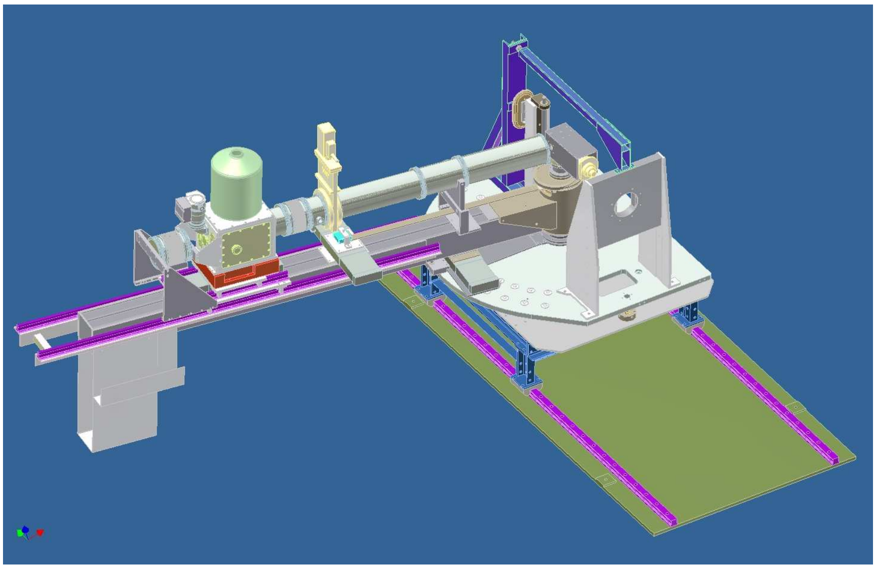

Figure 4.17: *Setup used for the characterisation of the emission direction of the PSI X-ray tube. The tube can be rotated around the vertical axis by about 25 degrees.*

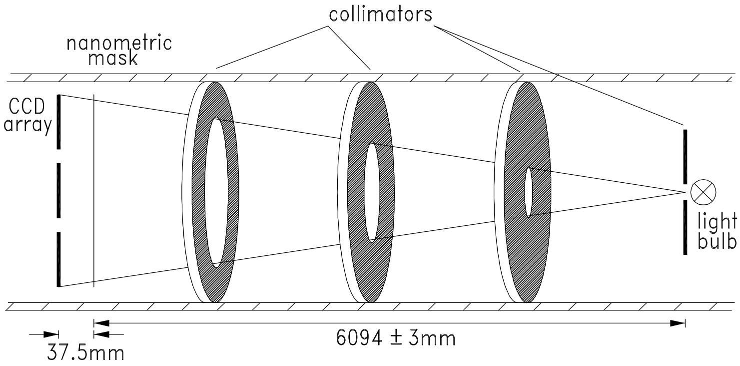

Figure 4.18: *Sketch of the setup to characterise the CCD array. The apertures placed in tubes avoid reflections at the tube walls to distort the pattern generated by the nanometric mask.*

1 mm diameter placed in front of a light bulb. Suitable exposure times, intensities and synchronization with data capture were realized by regulation of voltage and illumination time. To reduce parallax effects distorting the wafer image the distance from the light source to the quartz wafer was set to about 6 m. Reflections at the tube walls were eliminated using three additional collimators at appropriate distances inside the tubes connecting the light source and the detector (Fig. 4.18).

Chapter 5

Measurements

5.1 PSI

Choosing a silicon crystal (Tab. 5.1) cut along the (1 1 1) plane, the spectrometer had to be setup for Bragg angles around 40°. The parameters for the pionic deuterium Kβ and the gallium Kα transitions are given in Table 5.2.

To keep geometrical aberrations as small as possible, the centers of the target cell, crystal and detector were setup in a horizontal plane. Three well defined marks at the cyclotron trap, the crystal chamber and the detector cryostat were measured by the survey group of the PSI and related to the height of the pion beam entrance window and the center of the cyclotron trap (Tab. 5.3).

Several measurements for adjustment, including and most important the horizontal and axial scan of the target, i.e., the X-ray source were performed. In the axial target scan the intensities of the gallium Kα X-rays at different axial target positions were measured (Fig. 4.11). The axial position of the target cell was fixed to the setting with the GaAs target as close as possible to the center of the trap, but without disturbing the stop distribution of the pions. The horizontal target scan was done both with the gallium and the πD X-rays.

The main experiment was done by alternating measurements of gallium and πD. Each single measurement consists of 60 frames collected in one data file and lasts about one hour. Due to the high rate of gallium X-rays it is sufficient to do in average one measurement of calibration after seven πD measurements. In periods, when no pion beam was available additional gallium measurements were performed.

One aim of the experiment was to find out whether there are radiative de-excitations out of molecular formations. For this reason the πD (3p-1s) transition was measured at three different target densities using the cryogenic target as described in Chapter 3.2 (Tab. 5.4). During four weeks of beamtime 600 single measurements were performed. They divide into about 100 measurements for adjustment and about 500 measurements

crystal and cut	Si (1 1 1)	
lattice spacing	2d / A	6.2712016
curvature radius	R_C / mm	2982.24±0.25
miscut angle	α / °	0.288
miscut phase	ϕ_0 / °	-87.4
aperture opening circular	h / mm	95.0
aperture opening horizontal	w / mm	60.0
tilt	t / °	0.18

Table 5.1: *Properties and mounting of the used silicon crystal named Z13, which was shown in figure 4.12. The curvature radius is taken from [43].*

	energy / eV	order / n	Θ_B / °	$\Delta\Theta_{IRS}$ / "	R·$sin(\Theta_B)$ / mm	y_{CD} / mm	y_{CT} / mm
πD (3p-1s)	3075.670	1	40.0089	21.8	1918.06	1918.1	2100.0
Ga Kα_2	9224.484	3	40.0123	2.4	1917.98	1918.1	2182.0

Table 5.2: *Data to adjust the spectrometer in Johann-setup. y_{CD} denotes the distance between crystal and detector as y_{CT} the distance between crystal and target.*

part	height at center / mm
target cell	206.5±0.2
crystal	205.1±0.2
detector	206.1 ±0.2

Table 5.3: *Alignment of the main spectrometer parts.*

D_2 density (equivalent) / bar	temperature / K	pressure / bar
3.3	27	0.51
10.0	33	1.09
20.0	25	1.36

Table 5.4: *Parameters of the cryogenic target to measure a possible density dependence of the πD(3p-1s) transition energy.*

	density	number of	counts		counts	days of
	/bar	measurements	/Cb	/h	integrated	measurement
πD(3p-1s)	3.3	156	2.0		1500	10
	10.0	129	6.4		4000	8
	20.0	140	7.3		4800	6+1
Ga Kα_2		84		1200	100000	

Table 5.5: *Statistics of data as obtained from online analysis.*

at 3.3 bar, 10 bar, 20 bar πD and of gallium Kα X-rays for calibration purposes and stability monitoring. The online analysis resulted in a total number of ~10000 πD X-rays together for all densities (Tab. 5.5). The whole file list of measurements can be found in appendix A.

5.2 Jülich

5.2.1 Ga Kα energy check

The spectrometer was adjusted in the same geometry described in Subsection 5.1 for the PSI measurement. The target chamber was filled with 60 mbar of argon. The count rate for the argon line is less intense than the gallium line as the argon is a gaseous target.

Between the argon and the gallium measurements the Bragg angle was changed by two degrees as well as the focal position was adjusted (Tab. 5.6). To determine the alignment of the detector on the linear table in reference to the detector arm measurements with gallium and argon at different distances from crystal towards the detector between 1918 mm and 1995 mm were performed.

	energy / eV	order / n	Θ_B / °	$\Delta\Theta_{IRS}$ / ”	R·$sin(\Theta_B)$ / mm
Ar Kα_1	2957.68	1	41.9470	23.2	1995.1
Ar Kα_2	2955.56	1	41.9840	23.2	1995.1
Ga Kα_1	9251.67	3	39.8729	2.4	1918.06
Ga Kα_2	9224.484	3	40.0123	2.4	1918.06

Table 5.6: *Data used to adjust the spectrometer in Johann-setup.*

5.2.2 X-ray tube

To determine the emission characteristics of the X-ray tube used at the PSI experiment the X-ray intensity was measured in angular steps of 40 minutes. In the chosen setup with a distance of 1950 mm from the X-ray tube to the detector, the detector width of 24 mm corresponds to an opening angle of 42.3 minutes of arc. This ensures a gap less emission profile. At each position 60 frames were recorded. Anode current and voltage were chosen as small as possible to 5 mA and 5 kV.

5.2.3 CCD array alignment

The optimal illumination parameters as are light bulb voltage and data taking time were determined in a series of measurements. The bulb voltage was adjusted to 130 mV. Four different data sets were recorded. Two sets consisting of one ”dark frame” of ten seconds and nine images with a data taking time of ten seconds each and eight seconds illumination by the bulb. Another two sets were recorded with all times doubled. A ”dark frame” is a measurement without illumination by means of the light bulb to be able to subtract the electronic noise of the measurements. The number of measurements is sufficient to achieve an adequate small statistical error.

Chapter 6

Analysis

6.1 Characterisation of CCD array

The relative orientations of the CCDs was determined from the intensity distribution generated by the nanometric lattice structure of the quartz wafer (Chap. 5.2.3). An example of a recorded image of the total CCD array is given at the left side in Figure 6.1, in which also the numbering of the individual CCDs is indicated. CCD 6 was disconnected, because it was broken already before the πD measurements. The devices 3 and 5 have an extremely high noise level, which makes it difficult to analyse CCD 3 and impossible to analyse CCD 5. This is probably due to a transport damage.

The relative orientation of two devices is determined by reconstructing and aligning the straight lines produced by means of the illumination of the quartz wafer. The points constituting each line are developed by the fitted position of the main peak of the diffraction pattern taken at undisturbed regions of the wafer image in between crossing points. The right side of Figure 6.1 illustrates the procedure. A full description can be found in [80, 89]. This analysis was done within a Diploma thesis [90]. The orientations and positions were determined with CCD 2 as reference. As CCD 5 could not be analysed and CCD 3 was difficult to analyse because of the too high noise level, the result is a mixture of the new [90](CCD 1 and 4) and the old measurement [89](CCD 3, 5 and 6), which is sufficient as only CCD 1 and CCD 4 had been replaced. The extracted numbers are given in Table 6.1 and have been integrated in the program CSDcluster [91] used to process the raw data after detector readout as described in the next section.

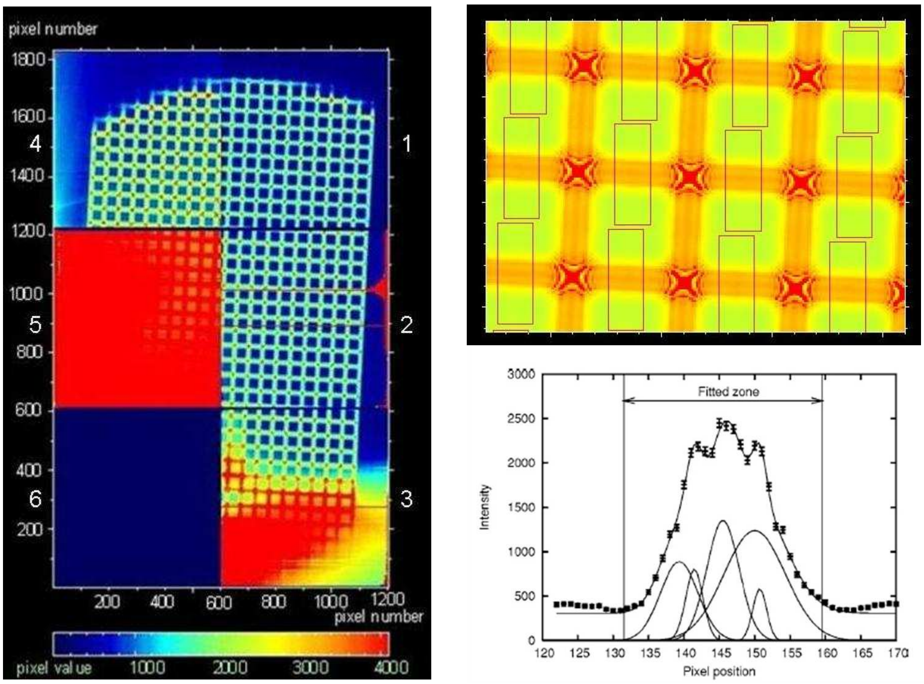

Figure 6.1: *Left: Front view of the image of the quartz wafer on the CCD array. Top right: Enlarged view on the crossing points. The fit regions of the intensity distribution are marked. Bottom right: Diffraction pattern of one fit region with a multiple Gaussian fit.*

No. of CCD	Δx / pixel	Δy / pixel	$\Delta\Theta$ / mrad
CCD1	-1.311± 0.074	5.656± 0.021	0.010± 0.034
CCD2	0.000± 0.000	0.000± 0.000	-0.002± 0.003
CCD3	0.509± 0.012	-11.021± 0.021	-0.677± 0.074
CCD4	-10.990± 0.065	12.200±0.040	2.471± 0.021
CCD5	-13.579± 0.009	1.738± 0.016	2.233± 0.130
CCD6	-15.963± 0.041	-9.435± 0.021	5.530± 0.011

Table 6.1: *Orientation of CCDs relative to CCD no.2.*

6.2 Data processing

As all measurements were done with the same type of detector and readout electronics as a first step of analysis all raw data can be treated in an identical way. When setting up the detector an energy calibration of the CCDs is done with 6 keV X-rays from an ^{55}Fe source to determine the gain and the noise level. The detector read out software processes this calibration and provides the measured data, i.e., the collected charge of the pixel, already offset corrected and data cut below the noise peak at an adjustable level (usually 3σ of the noise peak width). The files with the raw data are processed with the program CSDcluster which allows for data reduction to separate the events of interest from noise and background. The main routines for data processing are

- Bad pixel map
- Cluster analysis
- ADC cuts
- Curvature correction

and are described in some detail in the following. This part ends up with the construction of one dimensional position spectra by projection of the 2-dimensional hit pattern onto the direction of dispersion (x-axis).

6.2.1 Bad pixel map

The detection area consists of 6 × 360000 pixels, not all of them working properly. To eliminate the flawed pixels a so called "Bad pixel map" (BPM) is created. In this BPM all pixels responding more often than a specified number are collected. These pixels are identifiable because they respond more or less regularly without any measurement of real events. The threshold of this specific number depends on the number of frames per measurement and the exposure rate in the peak.

The result of the bad pixel investigation is shown in Figure 6.2. The main constituents are a number of hot horizontal lines and a big irregular area at the right edge of CCD 2. Sorting out some horizontal lines also has no effect on the measured line shape because it only reduces the detector size, i.e., the measured intensity. This becomes clear by inspecting Figure 6.9. The irregular area at the right side of CCD 2, however, influences the background information and, therefore, the line shape. For this reason the information of all three CCDs in the right column of the detector within channels 1100 and above in x-direction were rejected.

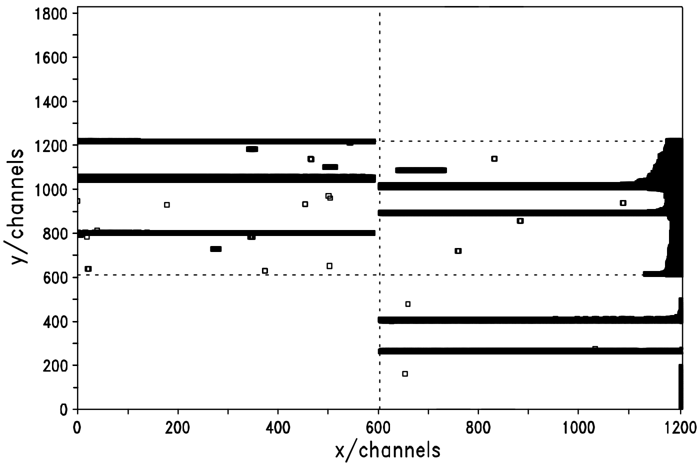

Figure 6.2: *Bad pixel map. The plotted pixel are identified not to work properly and are sorted out. Due to the horizontal read out whacked lines have no negative influence on the line shape of the X-ray reflection. CCD6 was not connected (left bottom), where CCDs 4 (left top) and 1 (right top) work without any distorted pixel.*

6.2.2 Cluster analysis

To separate X-ray events from background events, a cluster analysis is essential (Fig. 6.3). The 3p→1s transition energy in pionic deuterium amounts to approximately 3 keV. X-rays in this energy range are detected with a probability of 65 % in only one pixel and nearly all the rest in two pixels (Fig. 6.4). On the other hand high energetic background events are detected as larger clusters because they produce more extended charge distributions stemming from the larger range of Compton induced electrons. Whereas 3 keV X-rays convert in the first few μm depth of the detectors, background events are produced over the whole volume especially at the boundary of the depletion region.

For πD, the cluster analysis scans the detector area and sorts out all clusters consisting out of three or more pixel and clusters of two pixel without a common side (Fig. 6.3).

The 9 keV X-rays from the Ga Kα_2 transition are detected as much larger clusters because of charge splitting (Fig. 6.4). In this analysis all clusters larger than 9 pixel are sorted out. To accept such large clusters for gallium causes no problems, because the beam line was closed during the gallium measurements, which implies a negligible background in this case.

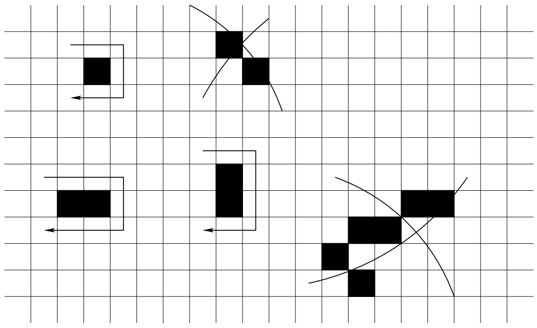

Figure 6.3: *Discrimination of few keV X-rays from beam-induced background events. The cluster size depends strongly on energy deposit and type of radiation.*

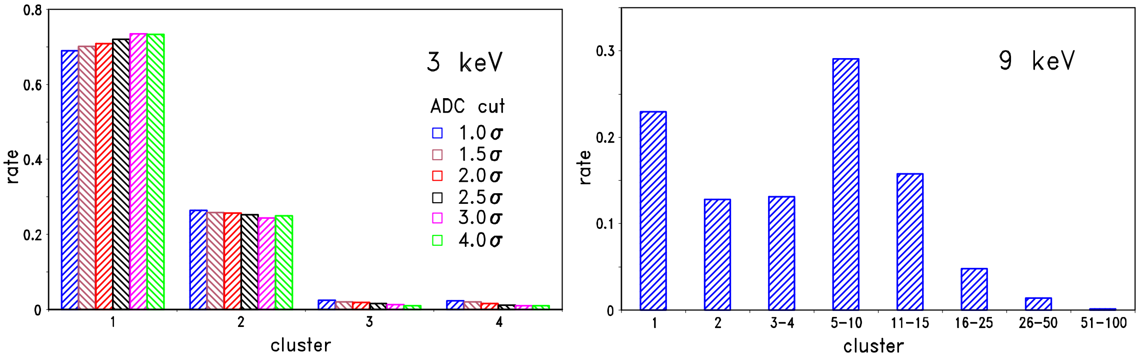

Figure 6.4: *Distribution of the cluster size for the 3 keV πD and for the 9 keV Ga X-rays.*

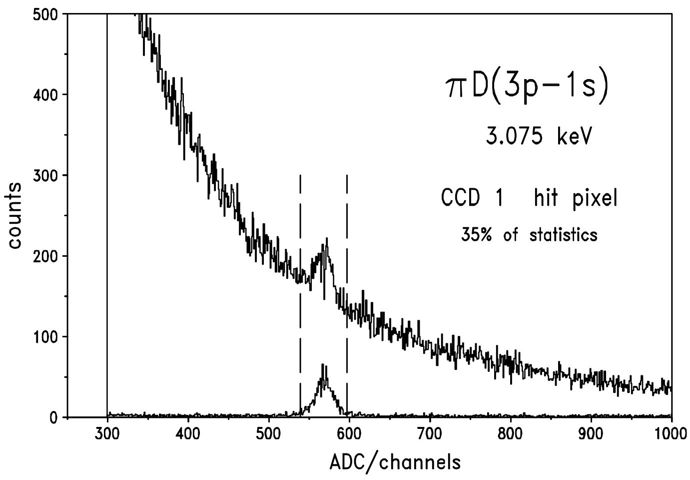

Figure 6.5: *ADC spectrum before and after performing the cluster analysis. The dashed lines show the energy cut at 2.5σ of the peak.*

6.2.3 ADC cuts

A further step to reduce the background is the setting of a window on the collected charge (ADC cut) around the interesting energy region. This is precisely possible due to good energy resolution of CCDs. The 3 keV X-ray peak in the energy spectrum can be in good approximation treated as a Gaussian. The 1 σ widths are obtained from the individual energy resolution of the various CCDs, which are 67 eV for CCD1, 112 eV for CCD2, 60 eV for CCD3, 76 eV for CCD4 and 88 eV for CCD5. CCDs 4 and 5 were needed for the background measurement (Chap. 6.6). The Ga Kα_2 and πD(3p-1s) lines were measured on CCDs 1-3. The resolutions differ from the theoretical limit, which is for 3 keV X-rays in the order of 33 eV, by factors of 2 for CCD1 and CCD3. The performance of CCD2 is inferior by another factor 2. The difference of measured and theoretical resolution is not only due to intrinsic noise of the detector electronics, but also due to induced noise from the surrounding. However, the energy resolution in the range of the pionic deuterium X-rays is sufficient for an efficient background reduction.

The best choice to set the ADC cut is shown by means of MC simulations [92] to be a width of 2.5 σ of the Gaussian peak. This setting delivers the smallest statistical error when determining the line width (Fig. 6.6). This cut corresponds to a window of 334 eV, 562 eV and 296 eV for CCD1, CCD2 and CCD3, respectively. Figure 6.7 shows, that for small ADC cuts the reduction of the count rate prevails the relative reduction of the background (Tab. 6.2).

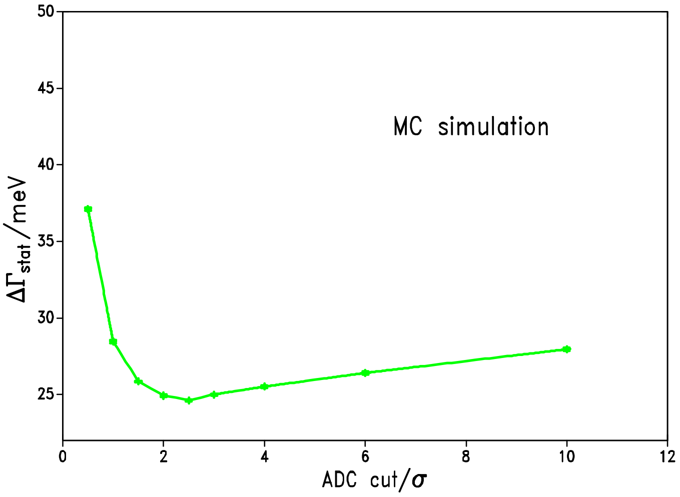

Figure 6.6: *Simulated data showing the connection of fit error for the line width and width of the ADC cut. A cut of about 2.5σ is the best choice. The figure is taken from [92].*

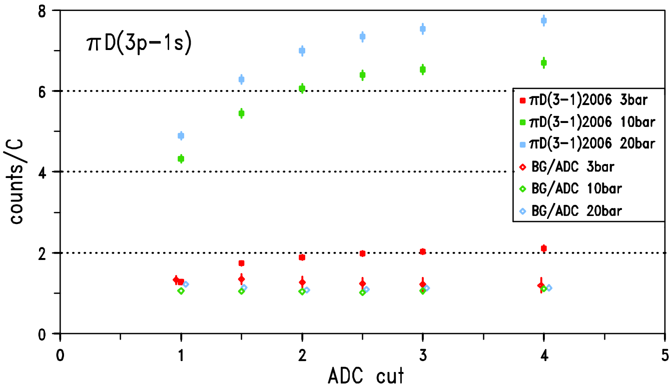

Figure 6.7: *Count rate in dependence on the ADC cut of the πD(3p-1s) line and the background normalised to the cut. The background is seen to be flat. This figure suggests to choose an ADC cut of 2σ or larger.*

data set πD(3P-1S)	ADC cut /σ	count rate/Q$_P$ /Cb	BG/ADC
3.3 bar	1.0	1.28±0.05	0.00133±0.00011
	1.5	1.73±0.06	0.00135±0.00012
	2.0	1.89±0.06	0.00127±0.00014
	2.5	1.98±0.07	0.00123±0.00015
	3.0	2.03±0.07	0.00122±0.00016
	4.0	2.10±0.07	0.00120±0.00018
10.0 bar	1.0	4.32±0.10	0.00105±0.00013
	1.5	5.45±0.11	0.00104±0.00016
	2.0	6.06±0.11	0.00104±0.00018
	2.5	6.40±0.12	0.00101±0.00018
	3.0	6.53±0.12	0.00105±0.00019
	4.0	6.70±0.12	0.00111±0.00022
20.0 bar	1.0	4.89±0.10	0.00122±0.00014
	1.5	6.29±0.11	0.00113±0.00015
	2.0	6.99±0.12	0.00108±0.00017
	2.5	7.34±0.12	0.00109±0.00018
	3.0	7.53±0.12	0.00112±0.00020
	4.0	7.74±0.13	0.00114±0.00023

Table 6.2: *πD count rate and background (BG) for different ADC cuts normalised to the integrated accelerator current (Q_P).*

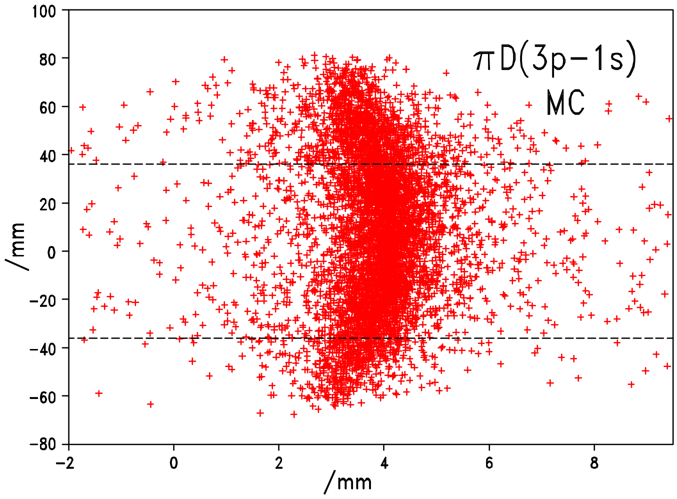

Figure 6.8: *MC simulation of the reflection. The dashed lines indicate the detector limits in vertical direction.*

6.2.4 Curvature correction

The final step producing a position spectrum is a curvature correction. As discussed in Chapter 4.1.2 the imaging properties of the spectrometer lead to a curved shape of the reflection in the detector plane. This can be easily seen by plotting a two-dimensional hit distribution of the data. Projection onto the x-axis without correction of this curvature leads to a distortion of the line shape in the position spectrum. For this reason the quasi hyperbolic curvature has to be adjusted to a straight line. Due to the small detector and target dimensions compared to the bending radius of the crystal the hyperbola can be in good approximation parametrised by a parabola $f(x) = ax^2 + bx + c$. In addition, the reflection overlaps only to about 60 % with the detector (Fig. 6.8).

The parameters a, b, and c needed for the curvature correction are obtained with the help of a χ^2 analysis. In our case the parameters of the curvature correction were determined to be $a = (-8.11 \pm 0.09) \cdot 10^{-6}$ and $b = (1.73 \pm 0.02) \cdot 10^{-2}$. The result can be validated comparing the curvature correction with the calculated radius of the reflection curve given by the bending radius [93]. The curvature of a parabola at the vertex amounts to $\kappa = 2a$, leading to a radius of the parabola at this point of $r_P = 1/2a$. The calculated curvature radius at this point, taking into account a flat detector perpendicular to the X-ray beam direction, is given by $r_v = R_C \cdot cos\Theta_B$. Inserting numbers one gets $r_P = (2466 \pm 28)\,mm$ and $r_v = 2284\,mm$ in reasonable agreement.

Figure 6.9 shows the effect of the curvature correction. After the curvature correction, projection onto the x-axis leads to the final position spectra. These spectra are

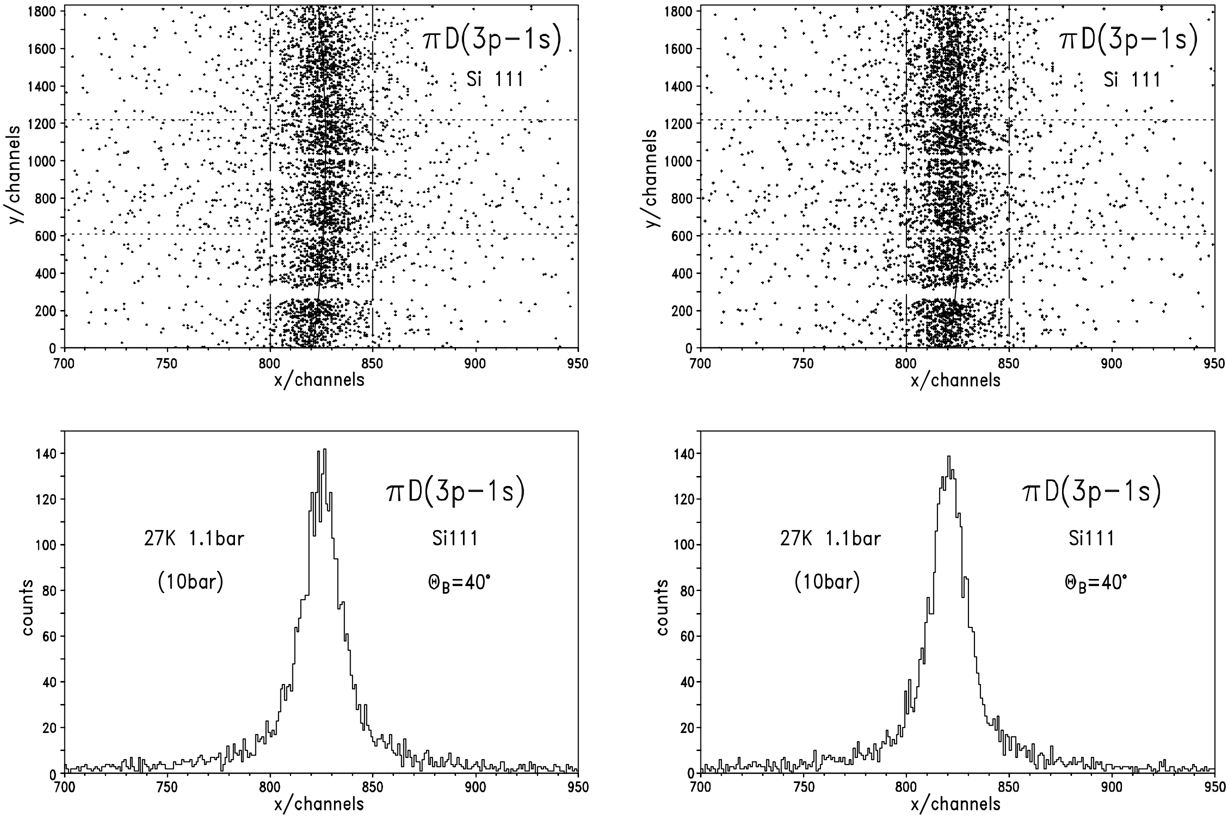

Figure 6.9: *Two-dimensional distribution of the cluster analysed 10 bar πD data and one-dimensional position spectra obtained from projection to the x-axis without (left) and with (right) curvature correction.*

used to extract the hadronic ground-state width and from comparison with the Ga Kα position spectra the hadronic ground-state energy shift.

6.3 Spectrometer stability

The stability of the spectrometer was monitored by two different methods. The first one is a check with help of the gallium Kα_2 calibration line by fitting the position of the peak for measurements spread over the whole beam time. A possible instability of the spectrometer is then visible in a varying position of the Kα_2 line. Figure 6.10 shows the variation around a mean value for each measuring period. Stability of the spectrometer for each period can be assumed, as the gallium position changes within statistical fluctuations. Offsets between the various periods are due to mechanical changes of the setup.

The second method is to evaluate inclination sensor recordings. Two sensors were

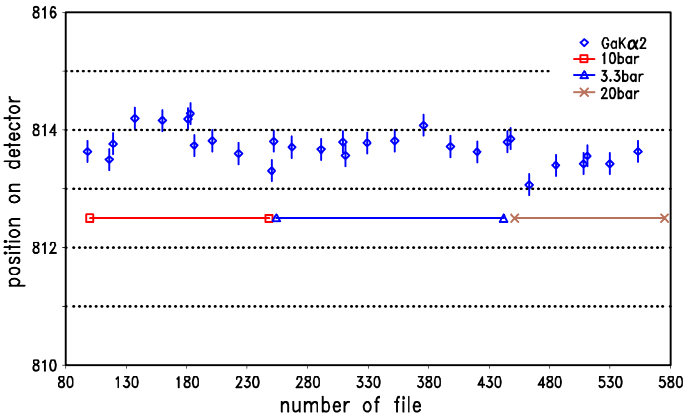

Figure 6.10: *Time dependence of the gallium Kα_2 peak position.*

mounted at the setup (Chap. 4.2.7). One at the top of the crystal chamber and the other one at one side of the detector cryostat in the height of the CCD array (Fig. 4.14). They measure the inclination to the vertical direction in x- and y-direction by an angular deviation. The values were recorded every 15 minutes. In Figure 6.11 the data of the sensor at the detector is shown for the whole beam time.

The point of interest is the variation of the CCD detector position in relation to the position of the crystal. To correlate the inclination data with the positions of detector and crystal an axis of rotation has to be specified. Considering the mechanical setup a natural choice is the base of the crystal chamber where it is connected to the spectrometer platform and for the detector the air cushion supports. These axes are marked in Figure 4.14 as 15 and 16. By taking the horizontal and vertical distances to the respective sensors the inclination can be transformed in position offsets. As an example the horizontal position difference variation of the detector relative to the crystal for the measurement at 20 bar is given in Figure 6.12. It can be seen that the fluctuation is 25 μm corresponding to 0.6 pixel. The variance of the mean value of -0.165 mm amounts to 0.007 mm. The maximal fluctuation of 60 μm is seen for the 3.3 bar measurement corresponding to 1.5 pixel. The variance amounts to 0.018 mm. In vertical direction the position variation is found to be extremely small and and thus can be neglected.

From analysis of the inclination sensor data clearly a day-night rhythm is visible. As the measurements of the gallium calibration line usually followed these rhythm (8:00 a.m.), the time of the calibration measurements can be related to the inclination sensor data (Fig. 6.12). Consequently, for each measuring period, i.e., for each measured D_2 pressure, the mean value of the relative position is determined for the gallium and πD measurements individually. This leads to a small correction, when extracting the position difference of the Ga Kα_2 line and the πD line (Tab. 6.12).

Besides the mechanical stability of the whole setup, stability and absolute value of

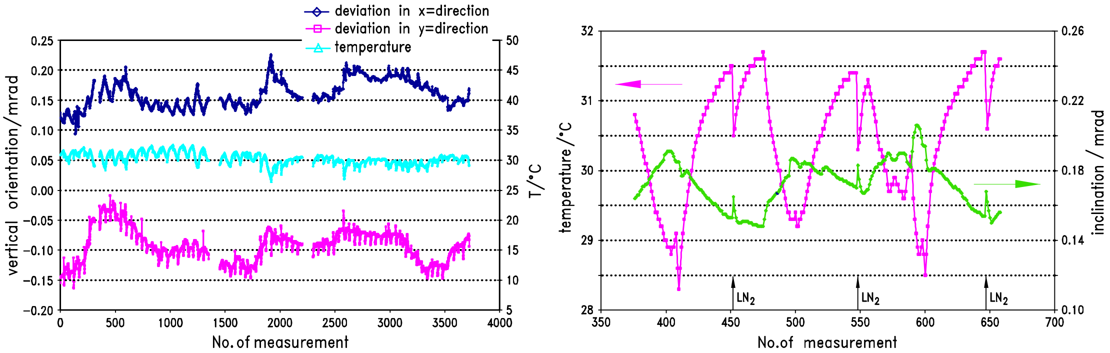

Figure 6.11: *Left: Time dependence of the data of the Nivel20 mounted at the detector cryostat during the four weeks of beam time giving a measure of the spectrometer stability. Right: Enlargement showing a three days interval. The filling of the detector dewar with liquid nitrogen (8:00 a.m. and 8:00 p.m.) precipitates in small peaks in the temperature as well as in the inclination sensor, but they are damped immediately.*

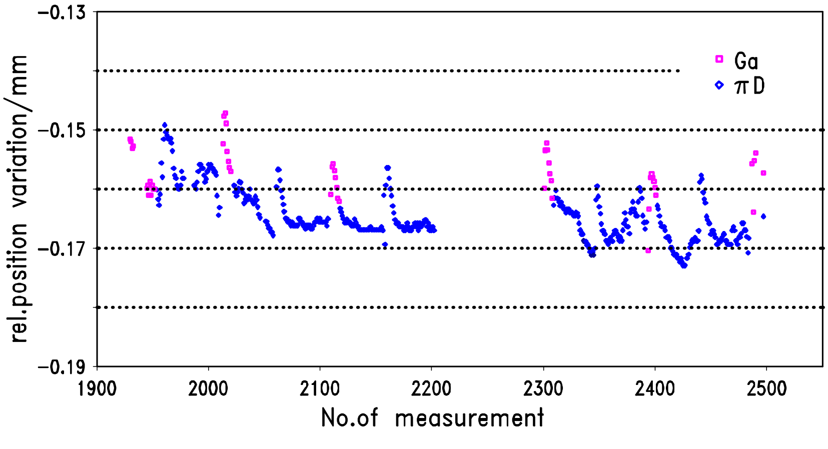

Figure 6.12: *Position variation of the detector relative to the crystal position derived from the inclination sensors data for the measurement at 20.0 bar.*

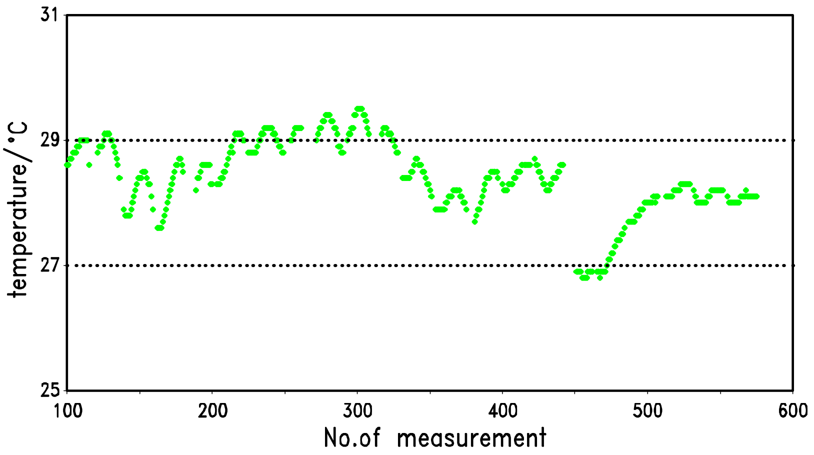

Figure 6.13: *Development of the crystal temperature.*

the temperature of the crystal is of importance due to the temperature dependence of the crystals d-spacing. It is $d(T) = d_0(1 + \Delta d(T))$ with $d_0 \approx 3.1356\,\text{Å}$ and $\Delta d(T) \approx dT \cdot (2.5 \cdot 10^{-6})/K$ for silicon. Therefore, large variations of the temperature can influence the peak positions of the πD and the Ga line differently. The progression of the crystal temperature is shown in Figure 6.13. The mean temperature amounts to 28.3° C. During each measurement period it varied by less than 0.5° C and therefore its effect on d is very small. The main reason for this good temperature stability is the concrete surrounding the crystal spectrometer. As the d-spacing d_0 usually is given in literature for a temperature of 22° C the d-spacing had been corrected relative to the mean temperature for each measuring period. This results in a small correction for the Bragg angle.

6.4 X-ray tube characterisation

Projection of the two-dimensional hit pattern of the single measurements onto the x-axis leads to an intensity distribution in horizontal direction. Each measurement corresponds to a specific angle interval defined by the orientation of the X-ray tube relative to the detector. The angular steps between the measurements allow to obtain a gap less angular intensity distribution of the X-ray tube, which is identified to be the emission characteristics of the tube. Figure 6.14 shows this distribution in a range from 2° to -0.75° build up from five single measurements. 0° corresponds to the axis of the X-ray tube exit window laying perpendicular to the direction X-ray tube to detector. Obviously, the X-ray emission is strongly asymmetric. This is due to the inner setup of the anode in the tube.

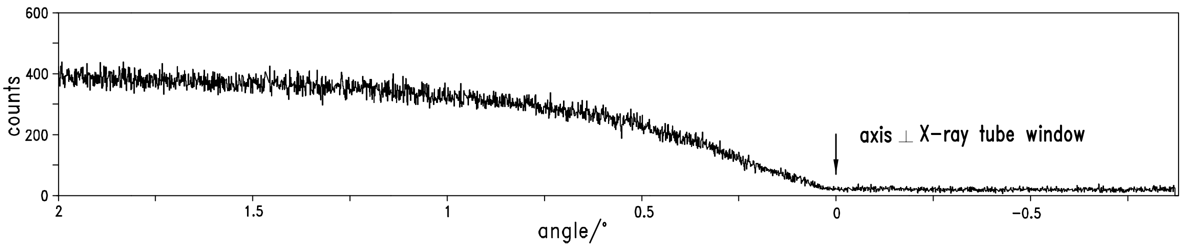

Figure 6.14: *Intensity against the emission angle shows the emission characteristics of the X-ray tube.*

6.5 Spectrometer adjustment

6.5.1 Axial scan

The axial scan of the traget cell was done to determine the optimum axial position of the cryogenic target at which the gallium-arsenide fluorescence target mounted inside the cell is maximally illuminated by the X-ray tube. The data are displayed in Figure 6.15. The zero point marks the position at which the target cell center coincides with the middle of the cyclotron trap. Here, the GaAs target is still shadowed by inserts in the gap of the cyclotron trap (Fig. 4.11). The gallium Kα intensities increase when shifting the target cell and with it the gallium target in direction to the crystal. After the optimal illumination is reached, the intensity is about constant.

The cell is placed at the very beginning of the flat region, namely at -12 mm, to avoid that the gallium target overlaps with the region where the pionic deuterium is formed.

6.5.2 Target scan

Moving only the detector arm does not effect the alignment between Bragg crystal and detector. That means, moving the arm changes the position within the extended target, where the Bragg condition is fulfilled. In that way the intensity distribution over the width of the X-ray source can be measured and the spectrometer can be set to the intensity maximum. As the gallium target is placed in the axis of the target cell and the gallium Kα_2 Bragg angle is nearly the same than the one of the πD (3→1) transition the intensity maxima should be at the same position. In Figure 6.16 on the left side the target scan measured with Ga Kα and πD transitions is plotted. The scan of the Ga Kα lines differs significantly from the expected one. This can be seen in Figure 6.16 on the right side, where the measured Ga Kα_2 scan is compared to a theoretical one generated by means of a MC simulation.

The reason for this was found in the emission characteristics of the X-ray tube (Chap. 6.4). In fact the unexpected shape of the target scan was the main impulse

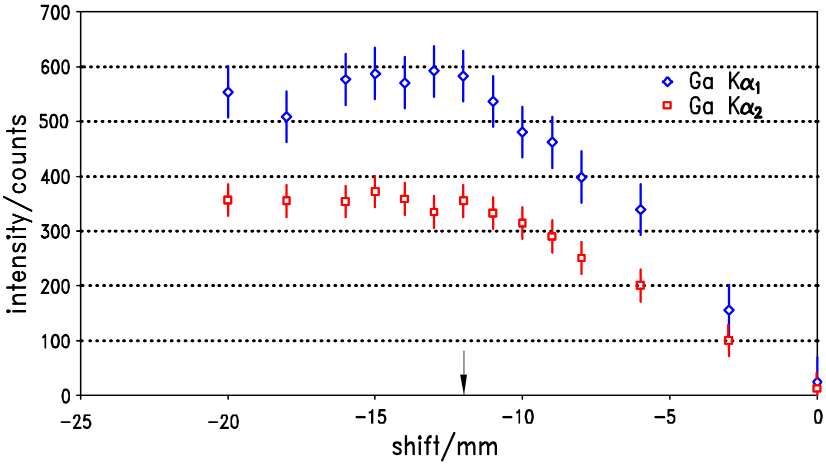

Figure 6.15: *Optimisation of the axial target position to ensure the gallium target to be maximally illuminated. The intensity of the gallium X-rays is measured at different distances towards the crystal. The final measuring position, fixed to a position at the beginning of the flat region, is marked by the arrow.*

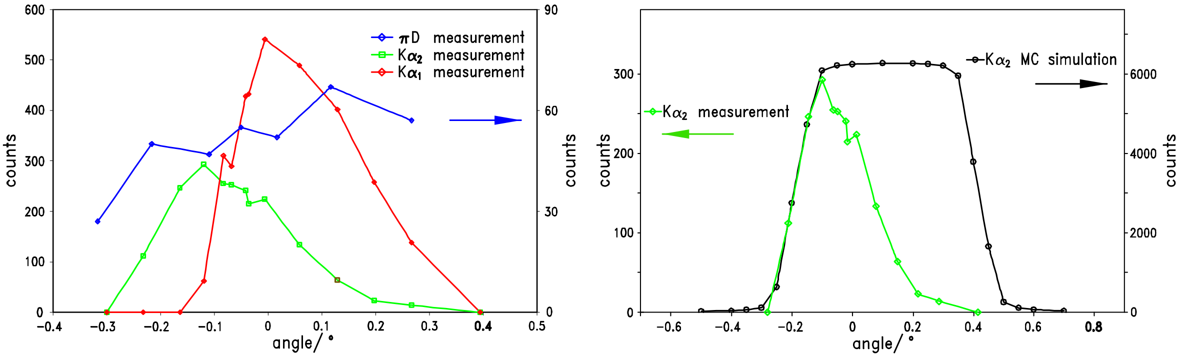

Figure 6.16: *Left: Target scans using Ga Kα and πD X-rays. Right: Measured and expected target scan from Ga Kα*$_2$ *X-rays.*

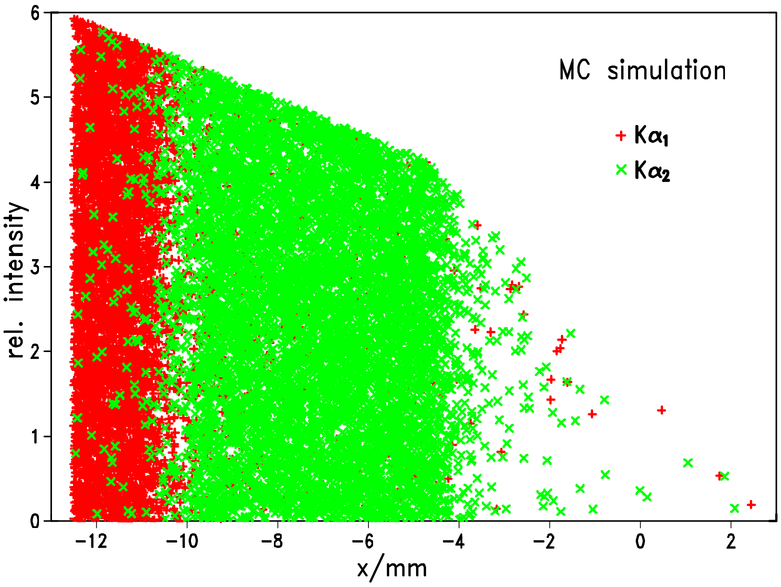

Figure 6.17: *MC simulation of the position and intensities of the gallium K*α_1 *and K*α_2 *lines on the target based on the experiment geometry as realised at PSI and the measured characteristics of the X-ray tube (Fig. 6.14). Only the part of the 25 mm wide target is shown, that could be illuminated.*

to work out the emission distribution. As the X-ray tube was mounted vertical under the target cell with the tube anode rotated by 90 degrees against the gallium target plane, the GaAs plate was not illuminated with uniform intensity. In Figure 6.17 the position of the gallium Kα_1 and Kα_2 line on the target during the pionic deuterium main measurement is shown. Only the part of the in total 25 mm wide target is shown that could be illuminated by the radiation of the X-ray tube. The height is a measure of the intensity distribution. The intensity increases towards higher energies, i.e., smaller Bragg angles. As the right side of the target could not be illuminated the damage of the target (Fig. 4.10) placed at this side does not contribute.

A MC simulation of the target scan taking into account the real target illumination is shown in Figure 6.18. The simulation now fits well to the measured target scan (Fig. 6.16) of both gallium transitions. The result of the simulation explains also the relative intensity of the Kα_1 and Kα_2 lines (Fig. 6.29) for the setup chosen for the experiment.

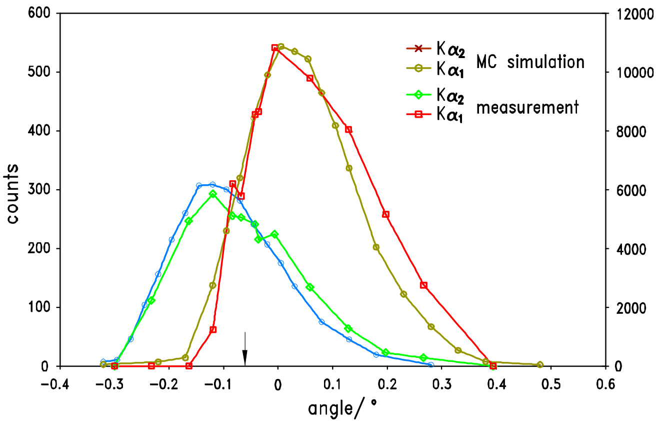

Figure 6.18: *Measured target scan of the gallium $K\alpha_1$ and $K\alpha_2$ lines and overlayed with a MC simulation taking into account the emission characteristics of the X-ray tube. The πD and Ga measurements were done at the position marked by the arrow.*

6.6 Hydrogen target measurement

To exclude a possible excitation of the gallium target by means of the pion beam, a measurement with hydrogen instead of deuterium gas in the target cell was performed. The measurement was done at a target pressure of 10 bar equivalent to achieve pion stop conditions similar to the one with deuterium. During this measurement the X-ray tube of course was switched off. As can be seen in Figure 6.19 no gallium X-rays could be identified. That means, no gallium X-rays are excited from beam induced reactions even with the fluorescence target mounted inside the gas cell.

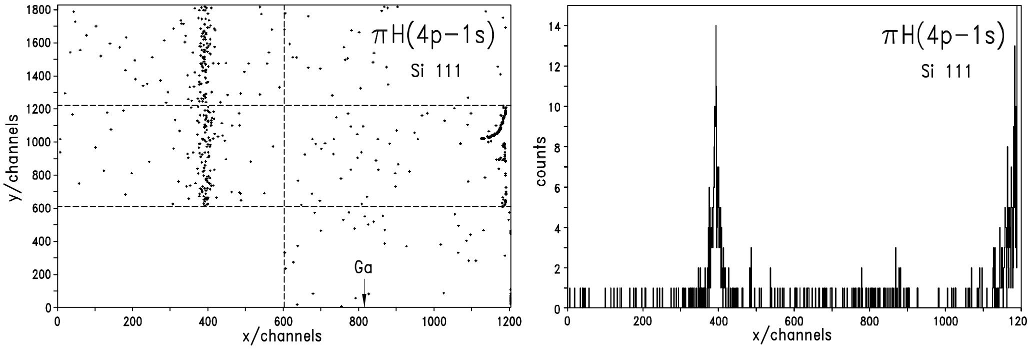

Figure 6.19: *The plot shows the result of a one day measurement with H_2 gas in the target cell. No X-rays from excitation through the pion beam are identified. A Ga $K\alpha_2$ reflection would show up at $x \approx 815$.*

	πD(3p-1s)	Ga Kα_2
energy / eV	3075.560	9224.835
refraction parameter δ=1-μ	5.193E-005	5.780E-006
extinction length σ polarization/ μm	2.24	10.96
extinction length π polarization/ μm	12.92	63.30
1/linear absorption coefficient/ μm	4.69	105.81
FWHM diffraction curve σ / μrad	114.06	8.52
FWHM diffraction curve π / μrad	34.05	1.52
integrated reflectivity R_I σ/ μrad	100.14	9.42
integrated reflectivity R_I π/ μrad	5.39	1.07
θ_B /°	40.00586	40.01548
$\Delta\theta_{ind}$ /°	0.00605	0.00067
θ_B corrected /°	40.01191	40.01615

Table 6.3: *Crystal parameters for the Si(111) (πD) and Si(333) (Ga) reflection as calculated by XOP [74] if not indicated otherwise. πD and Ga Kα_2 energies are from [69, 94].*

6.7 Spectrometer response function

The theoretical spectrometer response function is given by the rocking curve convoluted with the geometry effects due to the Johann setup. The origin of the rocking curve was discussed in Chapter 4.1 as well as the geometrical aspects of a Bragg crystal spectrometer in Johann setup. The program package XOP [74] delivers the rocking curve of an ideal flat crystal (Fig. 6.21 left). Parameters can be found in Table 6.3 for the πD(3p-1s) and Ga Kα_2. This is an idealized picture assuming a perfectly mounted crystal. For the correct spectrometer response function the influence of the imperfectness of the crystal material as well as an imperfect setup must be taken into account (see below).

The geometrical effects such as extended source, crystal size and bending as well as the overlap of reflection and detector are determined by a MC X-ray tracking routine [95]. This routine uses the rocking curves from XOP as input and calculates the Bragg reflection implying all geometrical properties of the experimental setup. The routine delivers a two-dimensional hit pattern in the virtual detector plane similar to the pattern recorded by the real detector. From this pattern a one-dimensional position spectrum is produced by applying a curvature correction and projecting onto the x-axis as described above in the data processing. This position spectrum represents the theoretical response function of the spectrometer. Furthermore, the tracking routine is used to study the influence of the different geometrical inputs, as are the size and shape of the target on the response function.

The theoretical response function is perturbed by imperfections of the setup. To determine the effect of these imperfections on the response function measurements with an Electron Cyclotron Resonance Ion Trap (ECRIT) were performed [96, 97]. This independent experiment was also setup at the PSI by inserting a permanent hexapole in the cyclotron trap.

In the ECRIT highly ionised atoms from low to medium Z atoms are produced and X-ray transitions from the helium-like ions are measured with the crystal spectrometer, using exactly the crystal setup of interest. In helium-like atoms narrow X-ray transitions exist with energies close to the ones of transitions in pionic atoms. It is important to use similar energies as the response function depends on the energy.

For example, in the case of πD a M1 transition in He-like argon leads to an X-ray of 3.10 keV (Fig. 6.20) where the 3p-1s transition energy in pionic deuterium is 3.08 keV. The lifetime of the $^3S_1$ state in He-like argon of $0.2\,\mu$s is synonymous to an extremely narrow line width. This implies, that the natural line width is negligible compared to the spectrometer response. In addition, any Doppler broadening due to fast highly ionised atoms have been found to be small for ECRIT type devices [98]. In this way the real spectrometer response function is measured for this specific energy.

It turns out, that the additional broadening coming from the crystal imperfections can be well described by a single Gaussian. For more details concerning the experimental setup, procedure and analysis of the ECRIT measurement see [43, 97]. In Table 6.4 the additional Gaussian widths for different energies measured with different atoms are given for the silicon crystal with a 60 mm aperture used in this experiment. Interpolating the measured values the broadening at the energy of the πD (3p-1s) transition is assumed to be $35\,\mu$rad. The full response function of the crystal spectrometer is then build up by means of the tracking routine by a convolution of three components (Tab. 6.4):

$$RF = rocking\ curve \otimes geometry \otimes additional\ Gaussian. \tag{6.1}$$

Knowledge of the response function now allows for a precise analysis of the pionic deuterium hadronic width and shift. The devlopment of the response function starting from the theoretical rocking curve by including the geometry and the Gaussian broadening is displayed in Figure 6.21. The energy resolution of the spectrometer for the 3 keV πD X-ray amounts Δ E$_{exp}$ = (436 ± 3) meV (FWHM).

gas, He-like	energy of M1 transition / eV	Gaussian / μrad	Gaussian / meV	total resolution / meV
Ar	3104.18	32.77±2.21	123.1±8.3	439±2
Cl	2756.85	40.95±2.07	109.7±5.5	381±2
S	2430.34	56.53±2.99	98.2±5.2	312±3

Table 6.4: *The additional Gaussian broadening of the crystal Z13 used in this experiment are given in dependence of X-ray energy [43]. The conversion to meV was done considering the dispersion at the corresponding Bragg angle. The last column shows the final result for the resolution of the spectrometer.*

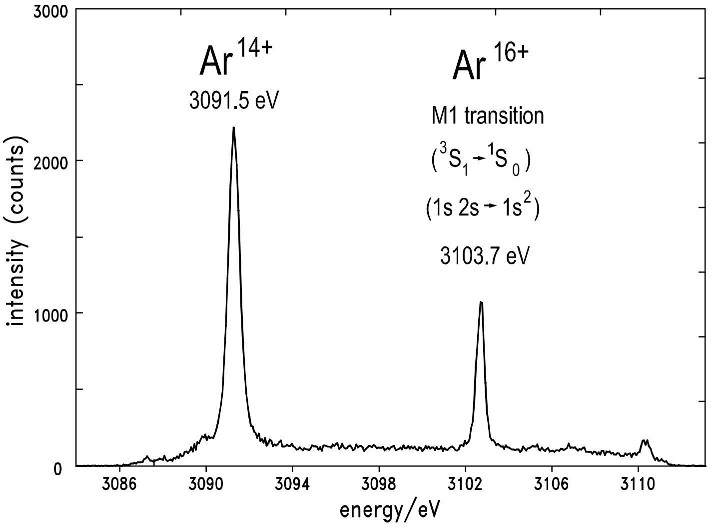

Figure 6.20: *Argon X-rays from Ar^{14+} and Ar^{16+}. The M1 transition in He-like argon is used to determine the spectrometer response (taken from [97]).*

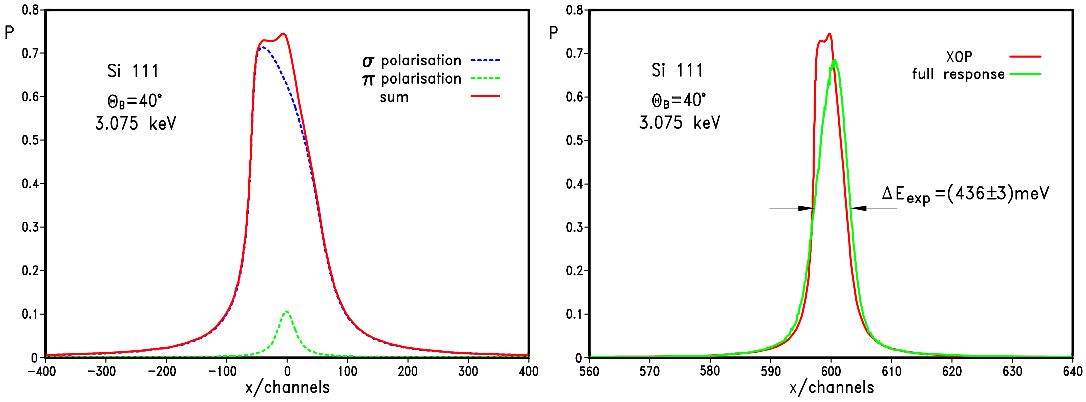

Figure 6.21: *Left: Rocking curve. Right: Response function build up from the rocking curve convoluted with effects of the geometry and the additional Gaussian broadening determined by the ECRIT measurement. The experimental resolution is found to be* $\Delta E_{exp} = (436 \pm 3)\, meV$ *(FWHM).*

6.8 Line shape

The line shape S of the 3p-1s X-ray transition in pionic deuterium is a convolution of three components,

$$S = RF \otimes \left(\sum_i D_i \right) \otimes L. \tag{6.2}$$

RF is the spectrometer response function, D_i stands for the Doppler broadening and L represents the Lorentzian of the ground state transition.

Two different fitting routines to analyse the line shape are available [92, 99], based on the same footing, a least squares fitting using the program package MINUIT [100] from the CERN program library. Parameters of the fit are the line position, the Lorentz width, the background and the relative weights ($\Sigma_{weight} = 1$) of up to five different Doppler-boxes (Chap. 2.2.4). The positions (mean kinetic energies) and widths of the respective Doppler-boxes are fixed input parameters. A further fixed input parameter is the response function RF normalised to 1.

In Chapter 2 the different processes occurring during the atomic cascade in pionic deuterium and leading to a kinetic energy distribution of the pionic atoms at the instant of the X-ray emission are discussed. As mentioned there, evidence was found for the μH system for a reasonable agreement with the energy distribution calculated from ESCM. A kinetic energy distribution calculated for the πH system and scaled to the πD Coulomb transition energies was tentatively used to describe the πD line shape (Fig. 2.5). It was found, that the distribution does not describe well the data.

Therefore, at first the analysis is performed with model free approximations using Doppler-boxes to identify Doppler contributions. Nevertheless, the analysis considers

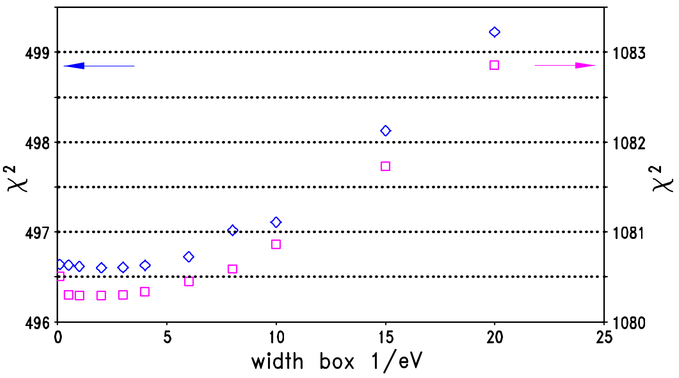

Figure 6.22: χ^2 *in dependence of the upper box limit for the sum spectrum of 10 bar and 20 bar (diamonds) and for a combined fit of both (squares). For the three measurements at 3 bar, 10 bar and 20 bar the development is similar.*

and compares also with the scaled kinetic energy distribution.

One box model

To start a systematic study of the line shape, at first fits with only one Doppler-box are performed searching the main contribution in the kinetic energy distribution. The 10 bar and the 20 bar statistics was added to increase the sensitivity since no essential difference in the line shape is found. It is evident from the χ^2 test, that a low energy box from zero to a few eV is mandatory to describe the line shape. This result is in line with the results from the muonic and pionic hydrogen as well as with predictions of the cascade calculations, where about 2/3 of the atoms have a kinetic energy in the range between 0 eV and 1 eV. The same is found also in the individual spectra of the measurements at the three target pressures. A low energy box can be interpreted that way, that a large number of πD atoms arriving at the n=3 state gained their kinetic energy only at upper cascade levels by Coulomb de-excitation and/or lost kinetic energy due to elastic or other collisions.

In a next step, the width of this first box is determined by fixing the lower limit to zero and varying the upper limit. The results, depicted in Figure 6.22, show that the fit is hardly sensitive on the upper limit of the Doppler box below about 8 eV. It is fixed in the following to 2 eV.

Two box model

After fixing the first box a second one is implemented. The second box is placed at the possible energetic positions of the energy gains due to Coulomb de-excitation. The results are shown in Figure 6.23. No evidence for a second kinetic energy box was

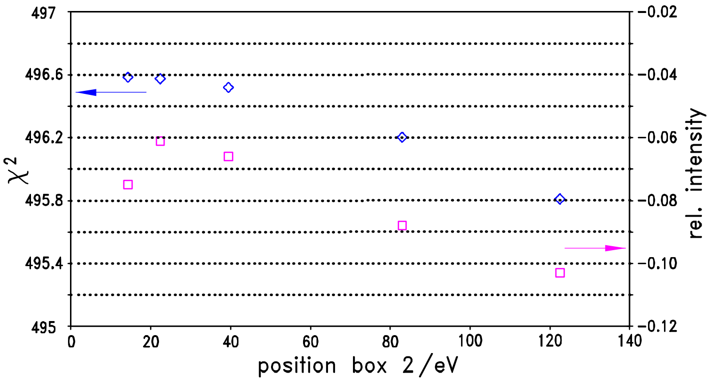

Figure 6.23: *The change in the* χ^2 *is plotted against the position of an assumed second kinetic energy box (diamonds). The relative intensity of the second box in relation to the full line intensity is shown (squares). Note the "unphysical" result of negative weights.*

found. The continuous decrease of χ^2 can be attributed to a systematic absorption of the background into the tails of the line. The best fit for a second box is found at all places with a box weight of even negative sign. In other words, the χ^2 optimisation leads to a second box with negative intensity, impossible high kinetic energies and, therefore, to an unphysical result.

The absence of a Doppler broadening stemming from Coulomb transitions suggests, that it is sufficient to fit the data with one low-energy box only. The fit results are given in Table 6.5 for various ADC cuts for the sum spectrum of 10 and 20 bar and in Table 6.6 for the individual spectra for ADC cut $2.5\,\sigma$.

Bias of the fitting routine. The used analysis routines use maximum likelihood estimation respecting the low background and low statistics in the tails of the measured spectrum following a Poisson distribution. In this case, the estimators can be biased, i.e., the mean value of estimates obtained from repeated independent experiments differs from the true value. Detailed discussions on maximum likelihood estimations can be found in [101, 102, 103]. To determine the value of the bias for the fitted Lorentz width, a high number of MC simulations were performed. The input parameters were adapted from the single measurements, to reproduce intensity, background and with it the peak to background ratio in that way, that the mean value of the BG fitted to the simulations is in good agreement with the value obtained from the free fit to the data. This is necessary because the background and the Lorentz width are strongly correlated. The bias of the width, which is only very weakly correlated to the input width [104], is then determined from the difference between the mean value of the width results and the input value of the width. The results can be found in Table 6.7 and 6.8. The bias corrected widths are given in Table 6.9.

ADC cut /σ	Γ_L /meV	$\Delta\Gamma_L$ /meV	BG	ΔBG	χ^2 /dof	χ^2_{red}
1.0	1181	30	1.31	0.08	553.823	1.137
1.5	1155	26	1.94	0.10	518.446	1.065
2.0	1161	26	2.62	0.11	488.996	1.004
2.5	1160	24	3.36	0.12	497.491	1.022
3.0	1159	24	4.10	0.13	494.099	1.015
4.0	1156	25	5.64	0.15	477.945	0.981

Table 6.5: *Fit results using the one box model with range from 0 eV to 2 eV and a fit interval of 490 channels leading to 487 degrees of freedom for the sum spectrum of 10 bar and 20 bar.*

pressure /bar	Γ_L /meV	$\Delta\Gamma_L$ /meV	BG	ΔBG	χ^2 /dof	χ^2_{red}
3.3	1208	71	2.18	0.09	566.040	1.162
10.0	1194	38	1.56	0.08	563.536	1.157
20.0	1132	32	1.79	0.09	480.126	0.986

Table 6.6: *Fit results using a one box model with range from 0 eV to 2 eV for the three measured pressures (ADC cut 2.5σ only) without bias correction.*

ADC cut /σ	Γ_{simul} /meV	Γ^{fit}_{mean} /meV	BG$_{simul}$ /(counts/ch)	BG$_{mean}$ /(counts/ch)	bias /meV
3.0	1160	1154± 2	4.14	4.10± 0.01	-6±2
2.5	1160	1158± 2	3.32	3.35± 0.01	-2±2
2.0	1160	1158± 2	2.60	2.62± 0.01	-2±2

Table 6.7: *Bias for different ADC cuts of the sum spectrum.*

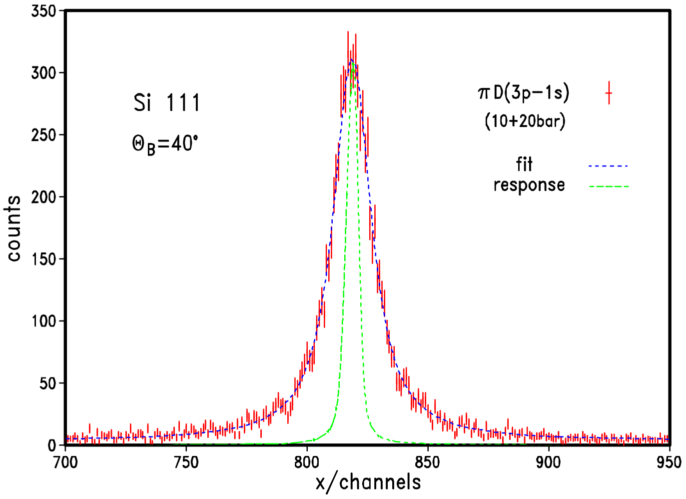

Figure 6.24: *πD spectrum with fit function (one box model) and spectrometer response. The narrow line represents the spectrometer resolution as determined from the ECRIT measurement.*

spectrum	Γ_{simul} /meV	Γ^{fit}_{mean} /meV	BG_{simul} /(counts/ch)	BG_{mean} /(counts/ch)	bias /meV
3.3	1210	1172± 3	2.16	2.17± 0.01	-38±3
10.0	1190	1207± 2	1.58	1.56± 0.01	17±2
20.0	1130	1141± 2	1.80	1.77± 0.01	11±2

Table 6.8: *Bias for the three different measurements with ADC cut 2.5σ.*

spectrum	ADC cut /σ	Γ_L /meV	$\Delta\Gamma_L$ /meV	bias /meV	Δbias /meV	Γ_L^{corr} /meV	$\Delta\Gamma_L^{corr}$ /meV
10.0+20.0	2.0	1161	26	-2	2	1163	26
	2.5	1160	24	-2	2	1162	24
	3.0	1159	24	-6	2	1165	24
3.3	2.5	1208	71	-38	3	1246	71
10.0	2.5	1194	38	17	2	1177	38
20.0	2.5	1132	32	11	2	1121	32

Table 6.9: *Bias corrected width results with statistical error.*

Statistical studies

Both in muonic hydrogen and in pionic hydrogen evidence for more than one Doppler contribution to the broadening was found using a model free fit. As a logical consequence a detailed study was performed, if such effects exist also in pionic deuterium. Aim of this study was, to find to which extend Doppler broadening effects can exist also in pionic deuterium without evidence can be found from the given statistics. Furthermore, the natural line width of pionic deuterium with about 1150 meV is much broader than the width of pionic hydrogen (≈800 meV [14]), which may cover the effects of the Doppler broadening. A series of MC simulations was performed with the same peak intensity and background as found in the fit of the 10 and 20 bar sum spectrum using an ADC cut of $2.5\,\sigma$. The Lorentzian width is an input parameter. For these simulations different kinetic energy distribution were predefined and scrambled in the simulations.

In a first series each kinetic energy distribution consists of a low-energy box, as found in the data, and an additional second box at 80 eV corresponding to the 4-3 transition, being predicted to be the most prominent additional contribution (Fig. 2.5). This second box was implemented with different weights and the spectra then fitted with a two box model. In Figure 6.25 is shown the distribution of the weights obtained from the fit of 400 simulations each for four different weights.

It can be seen, that even for 10% input weight only a small probability of about 15% is found, that the second box is missed by the fit. For weights of 25% and larger, however, some intensity was found in nearly 100% of the simulations. Figure 6.26 shows the relation between the probability <u>not</u> to find an existing intensity at higher kinetic energy. From this evaluation one concludes, that one can miss an intensity of up to 10% for a second box additional to the low energy contribution between 0 and 2 eV at the level of about 15%.

In the following, again by 400 MC simulations each, the dependence of finding some intensity for higher energy contributions from the details of the input distribution or the position of the second box is investigated.

In Figure 6.27 the influence of the position of the second box is shown for three different assumptions for the kinetic energy distribution, as each data set is fitted at three different box positions. At first, the box is placed in between the 5-4 and 6-4 transition at around 50 eV, secondly again at around 80 eV (4-3 transition) and third at the position of the 6-3 transition at about 140 eV. This transition represents the maximal kinetic energy, when scaling the ESCM prediction from πH to πD.

In simulation A the scaled kinetic energy distribution is used as input (Fig. 2.5). It can be seen, that it is very unlikely to miss the kinetic input intensity completely, independent of the position of the second box. This result allows to make the educated guess, that the ESCM prediction scaled to πD overestimates the rate of higher kinetic energies in the kinetic energy distribution.

For simulation B a kinetic energy distribution was constructed placing three boxes

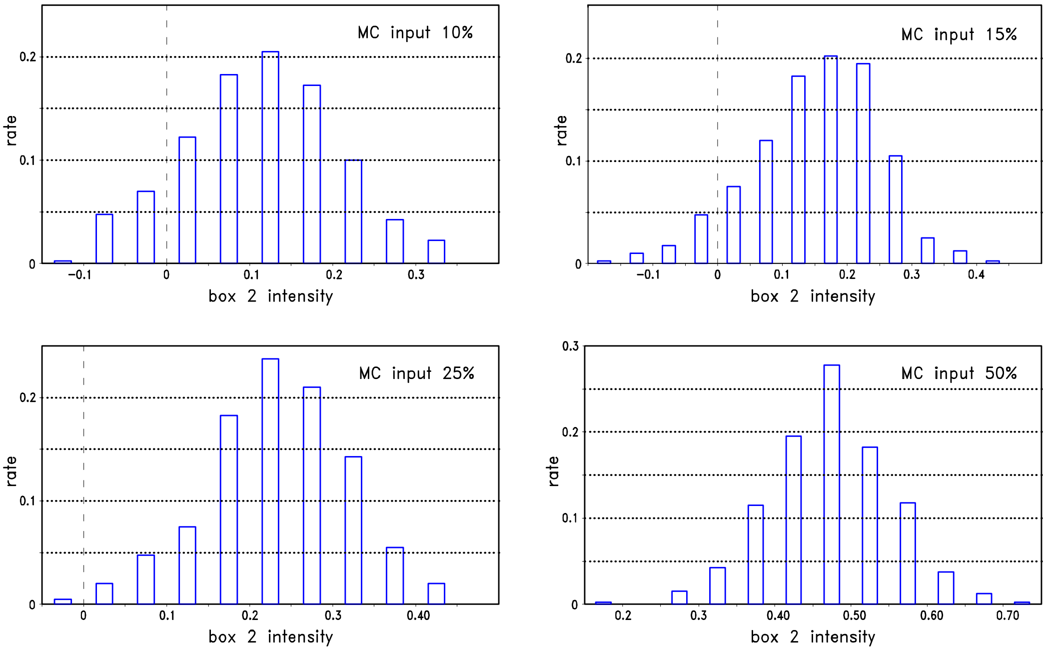

Figure 6.25: *Fit results of simulations with different input weight for a second box.*

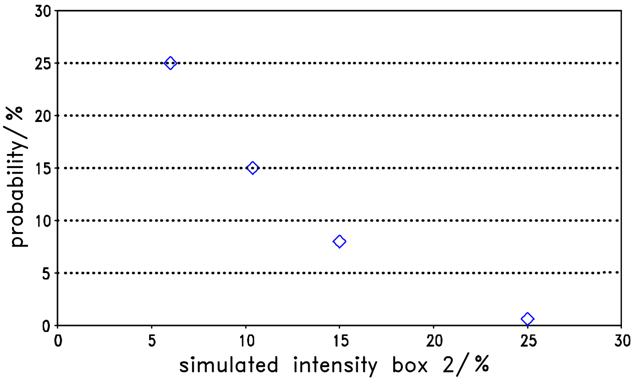

Figure 6.26: *Probability that the fit does not find an existing second box as a function of the weight of the second box.*

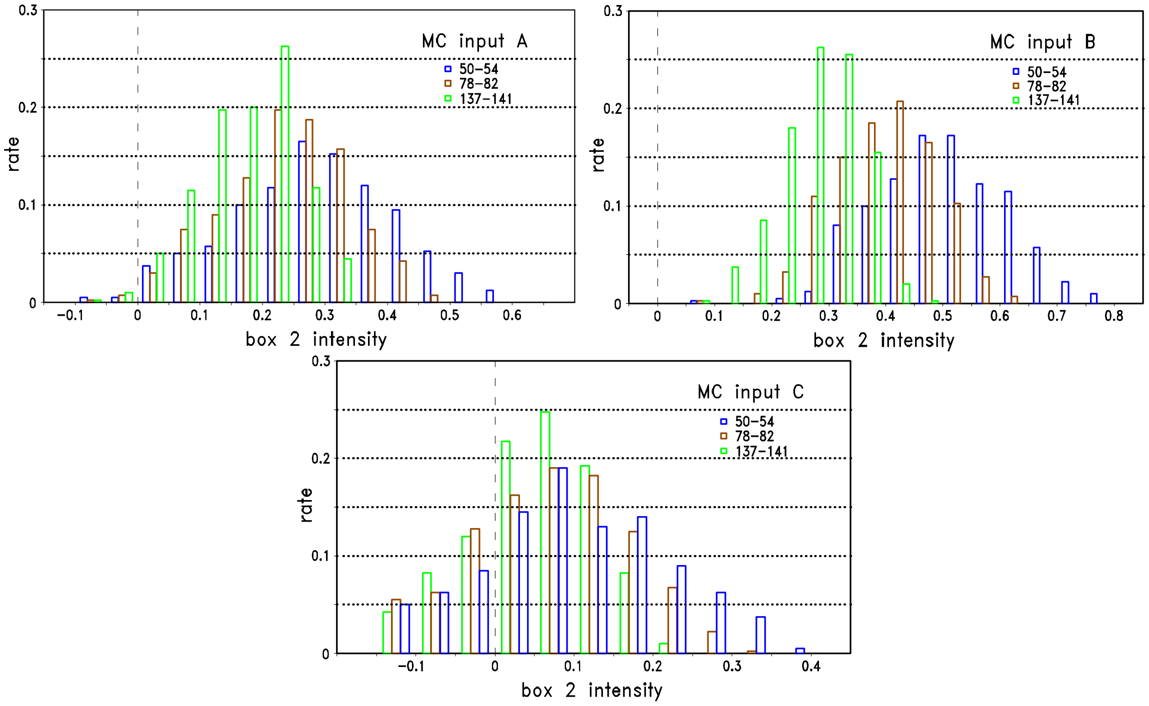

Figure 6.27: *Variation of fit results of different simulations. Simulation A used the scaled kinetic energy distribution calculated for* πH*, in simulation B 50% of intensity are placed randomly at higher energies and simulation C is done with 6% intensity evenly distributed between* $2\,eV$ *and* $140\,eV$*.*

with in total 50% intensity with different weights randomly between 2 eV and 140 eV. It can be seen, that systematically the box placed at the highest energy leads to a lower rate in the second box. This can be explained by the part of intensity which is placed between the low and the high energy box, not really fitting to one of them. This intensity must be divided in two parts and attributed to one of the boxes. Obviously, a larger difference between these boxes leads then to less intensity in the second box.

The only weak dependence on the exact shape of the distribution can also be seen from simulation C. Here, 6% of the line intensity were evenly distributed between 2 eV and 140 eV without accent on an energy region. Anyhow, for all three second box placements of 4 eV width each, the mean value of the second box intensity was found to be about 6%, perfectly consistent with the simulation input intensity.

Assuming now 10% of the line intensity to be Doppler broadened due to kinetic energies larger than 2 eV, one can see from the fit results of the simulations, that the weight of the second box intensity is directly correlated to the extracted line width (Figure 6.28 left). The input value of the width in the simulations was set to 1130 meV and the 10% intensity was placed at 80 eV (adapted from the 4-3 Coulomb transition). It can be seen from the slope, that not finding an intensity in the second box leads to an extracted width of 1160 meV. Shifting the additional kinetic energy distribution to higher or lower energies leads to a increased or decreased gradient of the slope, but does not change the zero crossing.

In Figure 6.28 right, the χ^2 belonging to the left side of the figure is shown. No dependence on the found rate alluding on the input rate for the second box exists and, therefore, no further information on the underlaying kinetic energy distribution can be extracted.

This result gives a measure of the systematical error of the line width determination from a missed second box in dependence of the total intensity above 2 eV, where the one box fit gives an upper limit. Concerning the 10 and 20 bar sum spectrum the value of this systematic error is, therefore, determined to be $\Delta\Gamma_{sys-int} =^{+0}_{-30}$ meV. For the single spectra the systematic error increases because of statistics. In cases of low statistics, broadening of the identified second box intensity distribution leads to an increased overlap with zero, and thus leads to higher intensities in the kinetic energy distribution which may be missed. This results directly in a increased systematic uncertainty, which can be given to be for the 3.3 bar spectrum $\Delta\Gamma_{sys-3.3}=^{+0}_{-140}$ meV, for the 10.0 bar $\Delta\Gamma_{sys-10.0}=^{+0}_{-80}$ meV and for the 20.0 bar $\Delta\Gamma_{sys-20.0}=^{+0}_{-70}$ meV.

Additionally a contribution to the systematical error must be added from the dependence on the detailed shape of the kinetic energy distribution and the fit model. It is evaluated to be $\Delta\Gamma_{sys-mod} =^{+0}_{-30}$ meV for the 10 and 20 bar sum spectrum. The lower boundary for these error values for the single spectra of 3.3 bar, 10 bar and 20 bar are found to be -60 meV, -45 meV and -40 meV, respectively.

The final value of the hadronic ground state width is extracted exploiting the in-

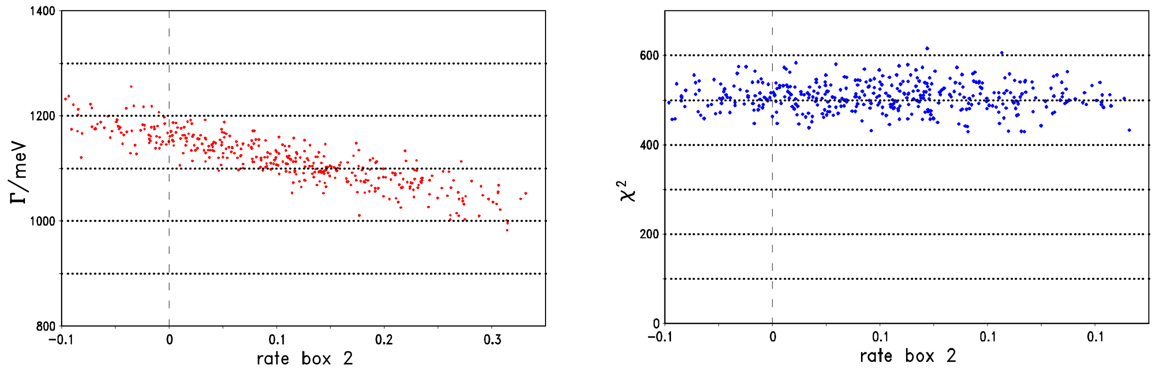

Figure 6.28: *Left: The extracted line width increases for the case, that less intensity is found in the second energy box. Right: Associated* χ^2.

creased statistics from the 10 and 20 bar sum spectrum, therefore, corresponding to an average target pressure of 15.5 bar. The total systematic error for the sum spectrum is $\Delta\Gamma_{sys} =^{+0}_{-43}$ meV.

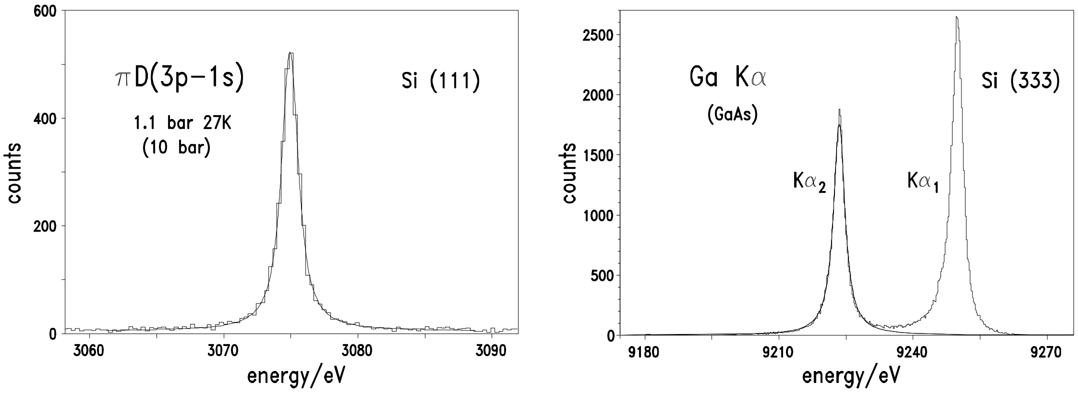

Figure 6.29: *πD measured at 10 bar and the associated gallium calibration spectrum. The position difference of the πD(3p-1s) and the Ga Kα_2 line on the detector is 0.1 mm only (Tab. 6.10).*

6.9 Transition energy

To determine the energy of the πD(3p-1s) transition measured in 1st order its position is compared to the position of the Ga Kα_2 line measured at 3rd order. The position difference Δx and the focal length Y_{CD} lead to a Bragg angle difference $\Delta\Theta_B$. The Ga Kα_2 energy is reported to be (9224.835 ± 0.027) eV [94], which corresponds to an expected angular difference to the πD (3p-1s) line in the order of about 7 sec of arc only. The positions of the different πD spectra were fitted within the analysis of the line shape and, therefore, can directly be used for the energy shift determination. The position of the Ga Kα lines is obtained with the program FITOS [105] using Voigt profiles. In the case of Ga, the natural line width of about 2.6 eV exceeds by far the spectrometer response.

The πD(3p-1s) transition spectrum at 10 bar target pressure and the associated Ga Kα_2 spectrum are shown in Figure 6.29. The results for positions and position differences are given for each measured pressure in Table 6.10. From the angular difference the absolute Bragg angle and from that the πD(3-1) transition energy is determined. The transition energies are calculated by means of the corrected Bragg law, i.e., taking into account the index of refraction shift (Tab. 6.11).

Finally, in addition to the statistical analysis, corrections have to be applied and systematic errors have to be studied. The list of corrections and sources of systematical errors are given in Table 6.12 and shortly discussed in the following.

Crystal bending. As described in Chapter 4.1 bending of the crystal changes the d-spacing in dependence of the crystal depth. Therefore, the correction is slightly different for the πD and for the gallium line. For the calculation a Poisson ratio of ν=0.182 was used, also for the following correction.

target pressure /bar	πD(3-1) position /pixel	Ga Kα_2 position /pixel	Δx /pixel	$\Delta\Theta_B$ /arc sec
3.3	817.62±0.36	815.11±0.04	2.51±0.37	10.79±1.60
10	818.65±0.22	815.11±0.04	3.54±0.23	15.22±0.96
20	818.42±0.21	814.84±0.05	3.58±0.22	15.41±0.92

Table 6.10: *Position and position differences Δx of πD(3p-1s) and Ga Kα_2 yielding the Bragg angle difference $\Delta\Theta_B$.*

target pressure /bar	Θ_B				E$_{trans}$ /eV
3.3	40°	0'	35.8"	± 1.6"	3075.482±0.028
10	40°	0'	31.3"	± 1.0"	3075.559±0.017
20	40°	0'	31.1"	± 0.9"	3075.562±0.016

Table 6.11: *πD transition energies as calculated from the Bragg angle using the corrected Bragg law and showing the statistical error.*

Penetration depth. The different penetration depths for the πD(3-1) transition and the Ga Kα_2 transition due to the energy difference of a factor 3 leads to an offset to the high energy side for increasing transition energies.

Curvature of reflection. The curvature correction to linearise the reflection can contribute to the systematical error. The correction can be estimated by comparing curvature corrections performed with the πD reflection and the gallium reflection. In the end the curvature correction of the gallium reflex was used because of the higher statistics in the line.

Index of refraction shift. The error for the determination of the index of refraction shift calculated by the programm XOP has to be estimated. It is given by the uncertainties of the scattering amplitudes. From the tabulated values an upper limit of 1% is assumed [106].

Illumination of the gallium target. As discussed in Chapter 6.5.2, the Ga target was not fully and uniformly illuminated. Due to this fact to the shape of the Ga line an asymmetry is induced, which leads to a shift of the position. For this reason MC studies were performed. A number of Ga Kα lines were simulated on the one hand with the target properties found in the experiment and then again with a uniformly illuminated target, unrestricted in the width. It was found, that the measured asymmetry leads to a shift of the Ga Kα_2 position of

$$\Delta x_{asy} = (0.17 \pm 0.07)\, pixel.$$

Model of the Ga line shape. The Ga Kα_2 peak in the Ga Kα doublet spectrum is fitted using a simple one line model without additional satellites and identifying the energy of the peak maximum as the Ga Kα_2 transition energy. This procedure agrees with the one used to determine the Ga Kα_2 transition energy given in literature and which is used as reference in this experiment [107]. Furthermore, the reference energy given in literature was determined using a X-ray tube and also a GaAs target, i.e., with similar experimental conditions. Consequently, no bias determination is necessary in the gallium case.

Defocussing correction. Due to the different focal lengths of the πD and the Ga line a tiny correction taking into account the position difference was included.

Model of response function. The slightly asymmetrical shape of the response function can lead to a (small) shift of the fit result. This is already included in the position bias determination using the response function given by the tracking routine.

Focal length. The upper limit of deviation from the nominal focal length can be given as $\Delta Y_{CD} = \pm 0.2\,\mathrm{mm}$.

Orientation CSD tubes and CCD. Deviations of the parallelity of the vacuum tubes as well as of the detector orientation lead to an error of the angle difference, as the effective pixel size is reduced.

Height CSD out of plane. If the detector is out of plane, geometrical aberrations increase. The survey of the experiment geometry excludes noticeable effects as tested with the tracking routine (Chap. 5.1).

Target size and shape of stop distribution. In former πH measurements the shape of the pion stop distribution in the target cell was studied, defining together with the target window the effective target size. The analysis of this investigation resulted in a uniformly stop distribution. Together with the target window this results in a well defined target geometry. The optimal placement on this target is ensured by means of the target scan. Therefore, deviations are negligibly small.

Mechanical stability. The mechanical stability was discussed in detail in Chapter 6.3.

Pixel size. The nominal pixel size of the CCDs is given as $40\,\mu$m. Deviations of this nominal value were measured in [89] at different temperatures. The mean pixel size at -100° C was determined to be $(39.9775 \pm 0.006)\,\mu$m.

Temperature renormalization. The effect of d-spacing changes on the Bragg angle due to an temperature offset against the nominal value of 22° C was taken into account according to the temperature variation discussed in Chapter 6.3.

Ga Kα_2. The uncertainty of the Ga Kα_2 transition energy is taken from literature [94].

name of the correction	$\Delta\Theta_{\pi D}$ /”	$\Delta\Theta_{GaK\alpha_2}$ /”	$\Delta\Theta$ /meV	pos. error /meV	neg. error /meV
crystal bending	-3.726	-3.647	-1.41	0.36	0.89
penetration depth	-0.059	-0.317	4.58	1.07	2.66
curvature of reflection				2.0	2.0
index of refraction	21.800			3.87	3.87
index of refraction		2.400		0.43	0.43
illumination Ga target	0	-1.075	19.10	3.82	3.82
model Ga line shape		0	0	0	0
defocussing			0.11	0.01	0.01
model RF			-	-	-
focal length				0.18	0.18
orientation CSD-tubes				0	0.15
height CSD				0	0.16
target size πD				0	0
mechanical stability 3.3 bar			4.22	2.45	2.45
mechanical stability 10.0 bar			12.57	3.99	3.99
mechanical stability 20.0 bar			14.18	1.29	1.29
pixel size				0.14	0.14
temperature renormalization				0.02	0.02
GaKα_2				27.0	27.0
QED energy				7.87	7.87

Table 6.12: *Overview of corrections and errors in the hadronic shift determination.*

target pressure /bar	E_{trans} /eV	ΔE_{stat} /eV	ΔE_{sys} /eV	ΔE_{Ga} /eV
3.3	3075.509	±0.028	±0.007	±0.027
10	3075.594	±0.017	±0.008	±0.027
20	3075.599	±0.016	±0.007	±0.027

Table 6.13: *πD transition energies including all corrections and all errors.*

The resulting transition energies taking into account all corrections and systematical errors are given in Table 6.13.

6.9.1 Ga calibration measurement

The Ga calibration measurement was done for a consistency check to the transition energy of the Ga Kα_2 line as given in literature [94]. The procedure of the analysis was described before, as it is the same in this experimental setup as for the πD measurement. To determine the Ga Kα_2 energy by extracting the Bragg angle difference in relation to argon also the Kα_2 transition of argon was used, as the line shape of this transition is not as much influenced by satellite lines as the line shape of the Kα_1 transition. The measured spectra are shown in Figure 6.30. The almost same position on the detector is due to the fact, that the measuring angle was changed by two degrees between the measurements. A focal scan was performed to determine the alignment of the detector when changing the focal position between the argon and the gallium measurements.

The analysis shows, that the alignment of the detector in relation to the detector arm amounts to 1 pixel at a distance of ≈ 83 mm (Fig. 6.31). This result corresponds to an angle of 0.027° between the arm and the direction of detector movement. Besides the statistical error of the measurements and the error of the argon Kα_2 transition energy the accuracy of the result is limited by the systematical error stemming from the necessary adjustments between the measurements. The analysis results in

$$E_{Ga_{K\alpha_2}} = 9224.747 \pm 0.008(stat.) \pm 0.070(sys.) \pm 0.016(Ar)\, eV. \qquad (6.3)$$

This result is in good agreement with the value given in literature, but no further improvement of the tabulated value can be achieved with the setup available.

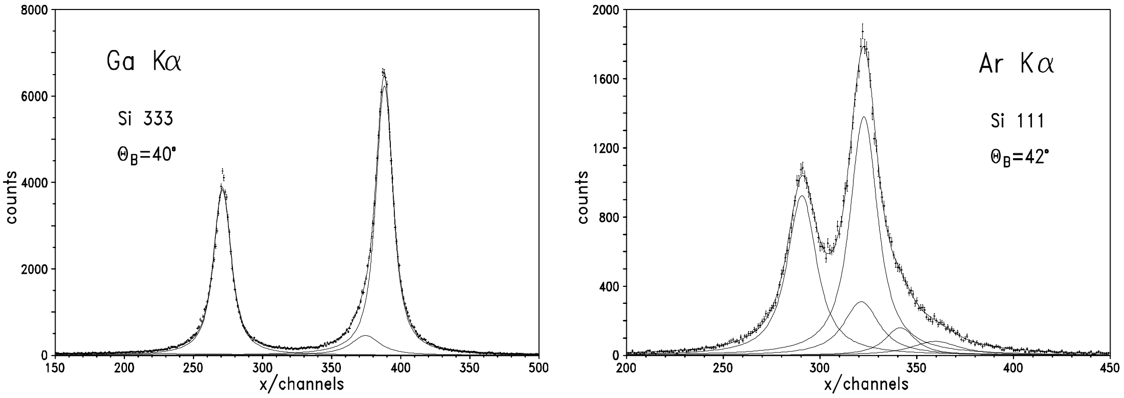

Figure 6.30: *On the left side the position spectrum of gallium is shown as on the right the spectrum of argon.*

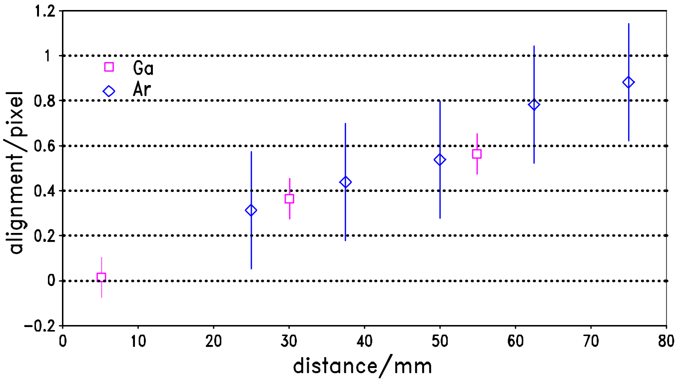

Figure 6.31: *Alignment of the detector determined from the shift of the peak positions at different distances crystal-detector.*

contribution	3p	1s	3p-1s
Coulomb	-384.31080	-3458.47050	3074.15970
Self-energy and F.N.	0.00000	0.00220	-0.00220
Vac. P 11	-0.01432	-3.72919	3.71487
Vac. P 13	0.00000	0.00002	-0.00002
Vac. P 21	-0.00013	-0.02789	0.02776
Recoil 1	-0.00004	-0.00297	0.00293
Relativistic recoil	0.00000	0.00029	-0.00029
L-A-L VP	0.00000	-0.00583	0.00583
Total energy	-384.32529	-3462.23387	3077.90858

Table 6.14: *Contributions to the pure electromagnetic transition energy* E_{QED} *[69].*

6.9.2 QED value

To extract the hadronic shift the pure electromagnetic transition energy has to be subtracted from the measured transition energy. Therefore, a well known QED value for the pure electromagnetic part is essential. For pionic deuterium a new calculation is available [69]. The different contributions to the calculated value are given in Table 6.14. The total purely πD(3p-1s) electromagnetic transition energy amounts E_{QED}=3077.90858 eV. The error of the calculated QED transition energy, arising from the uncertainties in the deuteron radius (0.00123 eV), the pion radius (0.00095 eV) and dominant the pion mass (0.00772 eV), is given by ΔE_{QED}=0.00787 eV.

Chapter 7

Results

7.1 Hadronic width

The results for the πD ground state width Γ_{1s} obtained from the line shape analysis are given in Table 7.1. As no density dependence is found within the experimental accuracy, the spectra of the 10 bar and 20 bar measurement were added which doubles about the statistics. The result obtained from this spectrum delivers the final value for the width. The final result is compared to former results in Table 7.2. All existing measurements are collected in Figure 7.1. The new result is in good agreement with the earlier measurements, but at least a factor of 3 more precise.

The imaginary part of the hadronic πD scattering length is determined from the width using Equation 3.22 to

$$\Im\, a_{\pi D} = (0.00621^{+0.00013}_{-0.00026}) m_\pi^{-1}. \tag{7.1}$$

target pressure /bar	Γ_{1s} /meV	$\Delta\Gamma_{1s}$(stat.) /meV	$\Delta\Gamma_{1s}$(sys.) /meV	$\Delta\Gamma_{1s}$(tot.) /meV
3.3	1264	± 71	$^{+0}_{-152}$	$^{+71}_{-168}$
10.0	1177	± 38	$^{+0}_{-92}$	$^{+38}_{-100}$
20.0	1121	± 32	$^{+0}_{-81}$	$^{+32}_{-87}$
sum 10.0+20.0	1162	± 24	$^{+0}_{-43}$	$^{+24}_{-49}$

Table 7.1: *Results of the pionic deuterium ground state width.*

transition	av. target pressure /bar	Γ_{1s} /eV	$\Delta\Gamma_{1s}$ /eV	reference
3p-1s	15	1.02	±0.21	[20]
2p-1s	2.5	1.194	±0.105	[21]
3p-1s	15.5	1.162	$^{+0.024}_{-0.049}$	this work

Table 7.2: *Comparison of width measurements of pionic deuterium.*

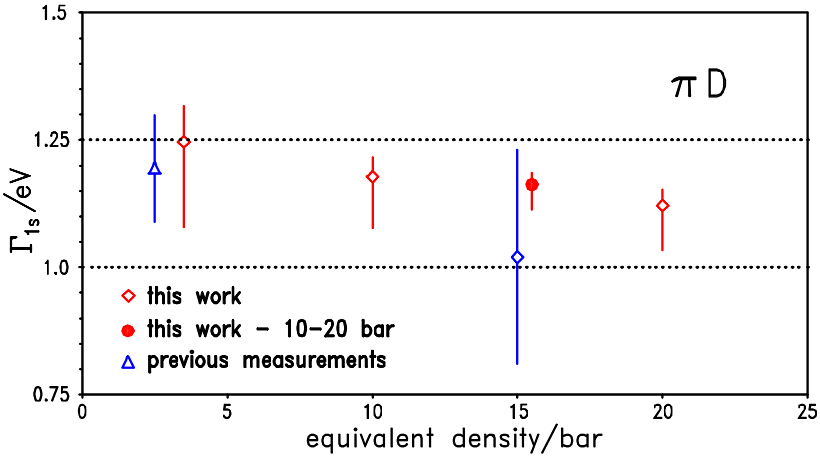

Figure 7.1: *Collection of measurements of the hadronic width in pionic deuterium.*

Furthermore from the width the pion s-wave production parameter α can be derived (Chap. 3.2.2). Table 7.3 and Figure 7.2 show a collection of results for α from different experimental and theoretical approaches. The small errors of the most production experiments is due to the omission of systematical uncertainties, i.e., represent only statistics. The value of this work is more precise, as no normalisation is necessary in our case, and Doppler broadening is reasonably well under control. The value obtained within χPT has the highest uncertainty, but the calculations are just at their beginning. Improvement of the uncertainty by a factor of 5 is expected in the next years.

data source	α /μb			remarks	reference
atomic					
πD(3p-1s)	220	±	45		[20]
πD(2p-1s)	258	±	23		[21]
πD(3p-1s)	250		$^{+5}_{-11}$		this work
production					
pp→ dπ^+	138	±	15		[108]
pp→ dπ^+	240	±	20		[109]
π^+d→ pp	180	±	20		[110]
π^+d→ pp	200			no radiative capture correction	[64]
π^+d→ pp	270			with radiative capture correction	[64]
pp→ dπ^+	228	±	46		[111]
pn→ dπ^0	184	±	5		[112]
π^+d→ pp	174	±	3		[113]
p_{pol}p→ dπ^+	208	±	5		[114]
pp→ dπ^+	205	±	9		[115]
theory					
Watson-Brueckner	140	±	50		[116]
rescattering	146			HJ	[117]
rescattering	146			HJ extended	[65]
Faddeev	220			Reid soft core	[118]
Faddeev	267			Brian-Scott	[118]
χPT NLO	220	±	70		[16]

Table 7.3: *Results for s-wave production parameter α obtained from several approaches.*

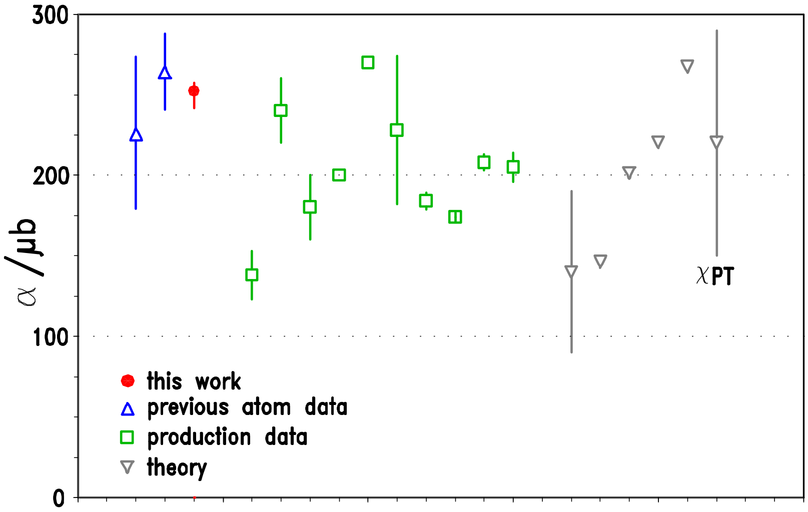

Figure 7.2: *Results for s-wave production parameter* α *obtained from several approaches.*

7.2 Hadronic shift

X-ray transitions from molecular states would lead to smaller (3p-1s) transition energies, and, therefore, to a reduced level shift with decreasing target pressure. No density dependence could be identified from the data. Consequently, the final result of the shift ϵ_{1s} is determined as the weighted mean value of the three measurements using the most recent value for the electromagnetic transition energy (Tab. 7.4).

In Table 7.5 the extracted shifts are compared to the results of all exisiting measurements and shown in Figure 7.3. The two former precision results are given at the basis of new QED calculations [69], which are in very good agreement with the new value. Noteworthy, that in the three measurements different calibration standards were used.

From the shift the real part of the scattering length is calculated (Eq. 3.15) to

$$\Re\, a_{\pi D} = (-0.02479 \pm 0.00033) m_{\pi}^{-1}. \tag{7.2}$$

target pressure /bar	ϵ_{1s} /eV	$\Delta\epsilon_{1s}$ /eV stat.	sys.	QED	Ga
3.3	-2.400	±0.028	±0.007	±0.008	±0.027
10.0	-2.315	±0.017	±0.008	±0.008	±0.027
20.0	-2.310	±0.016	±0.007	±0.008	±0.027
mean	-2.325	±0.011	±0.007	±0.008	±0.027

Table 7.4: *Shift results.*

transition	av. target pressure /bar	ϵ_{1s} /eV	$\Delta\epsilon_{1s}$ /eV	calibration	reference
2p-1s	4-5.8	-4.8	$^{+1.6}_{-2.0}$	Bi M_V edge	[18]
2p-1s	≈50	-5.5	±0.9	Cl $K\alpha_1$	[19]
3p-1s	15	-2.39	±0.07	Ar $K\alpha_1$	[20]
2p-1s	2.5	-2.430	±0.057	Cl $K\alpha_1$	[21]
3p-1s	13.7	-2.325	±0.031	Ga $K\alpha_2$	this work

Table 7.5: *Overview of shift measurements for pionic deuterium. The results of the precision experiments [20][21] and of this work were obtained using the most recent values* E_{3p-1s}*=(3077.90858±0.00787) eV and* E_{2p-1s}*=(2597.48834±0.00670) eV [69] for the electromagnetic transition energies.*

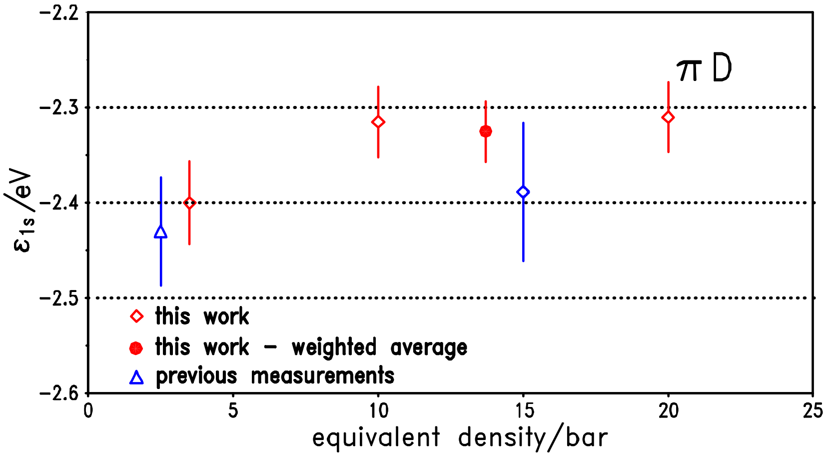

Figure 7.3: *Set of the existing measurements of the hadronic shift in pionic deuterium.*

Chapter 8

Conclusion and outlook

A high-precision measurement of the 3p-1s X-ray transition line in πD was performed with a Bragg crystal spectrometer in Johann setup to extract the strong-interaction effects in pionic deuterium. The results are

$$\epsilon_{1s} = (-2.325 \pm 0.031)\, eV, \; \frac{\Delta\epsilon_{1s}}{\epsilon_{1s}} = 1.3\% \tag{8.1}$$

and

$$\Gamma_{1s} = (1.162^{+0.024}_{-0.049})\, eV, \; \frac{\Delta\Gamma_{1s}}{\Gamma_{1s}} =^{+2.1}_{-4.2} \%, \tag{8.2}$$

improving the accuracy for the hadronic shift ϵ_{1s} and width Γ_{1s} by a factor of about 2 and 3, respectively, compared to the most precise previous measurement [21]. The largest contribution to the error of ϵ_{1s} is due to the uncertainty in the Ga Kα_2 X-ray energy (±0.027 eV) used for calibration. Consequently, a remeasurement of the Ga Kα_2 transition energy by means of a double flat spectrometer would be the next logical step in order to improve the accuracy of the hadronic shift.

From these results the complex pion-deuteron scattering length is obtained. It reads

$$a_{\pi D} = (-0.02479 \pm 0.00033) m_\pi^{-1} + i(0.00621^{+0.00013}_{-0.00026}) m_\pi^{-1}. \tag{8.3}$$

In the last years significant progress has been achieved describing the strong interaction at low energies within the frame work of χPT. Concerning the hadronic shift, an accuracy of 1.5% has been achieved recently [17], i.e., the experiment already reaches this level even with the existing precision for the Ga Kα_2 line. In the case of the threshold parameter α, directly related to the hadronic width, in a first approach a theoretical accuracy of about 30% was reported. However, an improvement by a factor of about 5 seems to be feasible within a few years [17], i.e., the experimental precision also here is sufficient.

In conclusion, the experimental accuracy and the expected theoretical result match nicely. Together with the forthcoming precise results for the hadronic shift and width in pionic hydrogen, in a combined πH and πD analysis more accurate values for the isospin scattering lengths a^+ and a^- and a significantly improved constraint for the almost unknown LEC f_1 will be obtained.

Appendix A

File lists

In this appendix the lists of data files of the PSI experiment is shown. The headers are shortly explained here:

- **date** is the day the measurement was performed.
- **crystal aperture** indicates the dimension of the aperture attached to the Bragg crystal.
- **target/source** is the target case or the fluorescence target, respectively.
- **p/mbar** is the real target gas pressure.
- **T/K** is the temperature of the target gas.
- **Q/C** is the integrated proton beam current.
- **LEX #/page** gives the page in the belonging beamtime logbook.
- **file name** is the name of the recorded data file. The files are named with incremental number.
- **comment** gives additional notes as times and spectrometer settings.

FILE LIST PSI 2006 **PIONIC DEUTERIUM** **Run book: LEX #13**

date	crystal aperture	target/source	$p_{average}$ /mbar	T /K	Q_p /C	LEX #/page	file name		comment
12.7.	Z13 ǁ60	Ga Kα	---	---	---		GaKa_0001-0004		Tilt adjust -0.07 -> +0.18 LinTab 56.76
12.7.	Z13 ǁ60	Ga Kα	---	295 K	---		GaKa_005-0017		14:40 Target scan 30kV 30 mA target warm
12.7.	Z13 ǁ60	Ga Kα	---	---	---		GaKa_0018-0027		17:32 Axial position of target 30 kV 30 mA
12.7.	Z13 ǁ60	Ga Kα	---	---	---		GaKa_0028		18:53 25kV 18mA
12.7.	Z13 ǁ60	Ga Kα	---	---	---		GaKa_0029-0033		19:01
13.7.	Z13 ǁ60	Ga Kα	---	---	---		GaKa_0034		11:30
13.7.	Z13 ǁ60	Ga Kα	---	26	---		GaKa_0035-0048		12:00 Target scan target cold
13.7.	Z13 ǁ60	Ga Kα	---	---	---		GaKa_0049-0062		Axial scan
13.7.	Z13 ǁ60	Ga Kα	---	---	---		GaKa_0063-0065		30kV 30mA target –12 mm CRY 42 31 05
		πH(4-1) BG							
13.7.	Z13 ǁ60	H_2	0.93	26?	86.35		piH_bg_0066-0083		18:30 CRY 40 20 00 ARM 42 31 05 LinTab 56.75
		πD(3-1)							
14.7.	Z13 ǁ60	D_2	1.09	27	66.39	13/102	piD3-1_0084-0097		16:31CRY 40 20 00 target scan LinTab 59.76
15.7.	Z13 ǁ60	Ga Kα	---	---	---	13/104	GaKa_0098-0099		8:50 CRY 40 20 00 ARM 42 31 00
15.7.	Z13 ǁ60	D_2	1.09	27.0	73.59	13/103	piD3-1_0100-0114		11:15 CRY 40 20 00 ARM 42 31 00 10 bar start
15.7.									4:02 PION3 crash – disk full
16.7.	Z13 ǁ60	D_2	1.09	27.0	4.91	13/103	piD3-1_0115		7:30
16.7.	Z13 ǁ60	Ga Kα	---	---	---	13/106	GaKa_0116-0120		9:05
16.7.	Z13 ǁ60	D_2	1.10	27.1	78.47	13/108	piD3-1_0121-0136		15:16
17.7.	Z13 ǁ60	Ga Kα	---	---	---	13/110	GaKa_0137-0138		8:25
17.7.	Z13 ǁ60	D_2	1.10	27.1	99.21	13/112	piD3-1_0139-0159		10:39
18.7.	Z13 ǁ60	Ga Kα	---	---	---	13/118	GaKa_0160-0161		8:47
18.7.	Z13 ǁ60	D_2				13/117	piD3-1_0162-0180		10:59
19.7.	Z13 ǁ60	Ga Kα	---	---	---	13/119	GaKa_0181-0185		7:28 after CCD off
20.7.	Z13 ǁ60	Ga Kα	---	---	---	13/128	GaKa_0186-0187		15:15
20.7.	Z13 ǁ60	D_2				13/	piD3-1_0188		empty beam line valve closed
20.7.	Z13 ǁ60	D_2	1.06	26.5	58.79	13/	piD3-1_0189-0200		20:03
21.7.	Z13 ǁ60	Ga Kα	---	---	---	13/130	GaKa_0201-0202		8:49
21.7.	Z13 ǁ60	D_2	1.09	26.8	92.42	13/	piD3-1_0203-0222		10:58
22.7.	Z13 ǁ60	Ga Kα	---	---	---	13/136	GaKa_0223-0224		8:05
22.7.	Z13 ǁ60	D_2	1.10	27.0	122.96	13/134	piD3-1_0225-0249		10:20 10 bar end
23.7.	Z13 ǁ60	Ga Kα	---	---	---	13/137	GaKa_0250-0251		11:50

crystal: Z13 silicon 111, (**aperture**: ǁ60), **focus** : according R_{ZEISS} = 2982,24 mm , set as earlier at marks 1,2,3
X-ray tube 30 kV, 30 mA if not noticed, Cr anode, **exposure time**: (30+30)s
CSD6 gain D

FILE LIST PSI 2006 **PIONIC DEUTERIUM** **Run book: LEX #13**

date	*crystal aperture*	*target/source*	$p_{average}$ */mbar*	*T /K*	Q_p */C*	*LEX #/page*	*file name*		*comment*
23.7.	Z13 ǁ60	Ga Kα	---	---	---	13/137	GaKa_0252-0253		16:04
23.7.	Z13 ǁ60	D_2	0,52	36.5	38.78	13138/	piD3-1_0254-0261		18:23 3.3 bar start
24.7.	Z13 ǁ60	Ga Kα	---	---	---	13/139	GaKa_0262		2:59 no beam 1 frame only
24.7.	Z13 ǁ60	Ga Kα	---	---	---	13/139	GaKa_0263-0269		2:59 no beam 60 frames
24.7.	Z13 ǁ60	Ga Kα	---	---	---	13/140	GaKa_0270-0271		14:20 no beam
24.7.	Z13 ǁ60	D_2	0.51	35.77	92.13	13/138	piD3-1_0272-0290		17:20
25.7.	Z13 ǁ60	Ga Kα	---	---	---	13/144	GaKa_0291-0292		13:17
25.7.	Z13 ǁ60	D_2	0.52	35.83	75.43	13/143	piD3-1_0293-0308		16:25
26.7.	Z13 ǁ60	Ga Kα	---	---	---	13/145	GaKa_0309		13:54
26.7.	Z13 ǁ60	Ga Kα	---	---	---	13/146	GaKa_0310-0314		9:18
27.7.	Z13 ǁ60	D_2	0.47	32.57	9.46	13/150	piD3-1_0315-0316	skipped	corrupt (noise overflow CD2)
27.7.	Z13 ǁ60	D_2	0.48	32.9	44.41	13/151	piD3-1_0317-0328		16:25
28.7.	Z13 ǁ60	Ga Kα	---	---	---	13/151	GaKa_0329-0330		8:34
28.7.	Z13 ǁ60	D_2	0.49	33.4	101.56	13/155	piD3-1_0331-0351		10:36 LinTab59.76 (LEX 13 p.153)
29.7.	Z13 ǁ60	Ga Kα	---	---	---	13/156	GaKa_0352-0353		8:22
29.7.	Z13 ǁ60	D_2	0.50	33.6	108.73	13/	piD3-1_0354-0375		10:24
30.7.	Z13 ǁ60	Ga Kα	---	---	---	13/159	GaKa_0376-0380		8:52
30.7.	Z13 ǁ60	D_2	0.50	33.8	77.44	13/159	piD3-1_0381-0397		14:25
31.7.	Z13 ǁ60	Ga Kα	---	---	---	13/163	GaKa_0398-0399		8:10
31.7.	Z13 ǁ60	D_2	0.51	33.9	91.62	13/163	piD3-1_0400-0419		10:10
1.8.	Z13 ǁ60	Ga Kα	---	---	---	13/168	GaKa_0420-0421		7:50 LinTab59.76 (LEX 13 p.167)
1.8.	Z13 ǁ60	D_2	0.51	34.0	101.40	13/168	piD3-1_0422-0442		9:52 3.3 bar end
2.8.	Z13 ǁ60	Ga Kα	---	---	---	13/169	GaKa_0443-0444		8:09
2.8.	Z13 ǁ60	Ga Kα	---	---	---	13/169	GaKa_0445-0447		15:21
3.8.	Z13 ǁ60	Ga Kα	---	---	---	13/169	GaKa_0448		10:55
3.8.	Z13 ǁ60	Ga Kα	---	---	---	13/169	GaKa_0449-0450		14:42
3.8.	Z13 ǁ60	D_2	1.37	25.15	56.04	13/175	piD3-1_0451-0462		16:54 20 bar start
4.8.	Z13 ǁ60	Ga Kα	---	---	---	13/175	GaKa_0463-0464		7:55
4.8.	Z13 ǁ60	D_2	1.36	25.05	4.94	13/176	piD3-1_0465	used!	9:58 file too long for csdcluster, new noise set.
4.8.	Z13 ǁ60	D_2	1.36	25.01	87.60	13/177	piD3-1_0466-0484		11:35
5.8.	Z13 ǁ60	Ga Kα	---	---	---	13/179	GaKa_0485-0486		8:25
5.8.	Z13 ǁ60	D_2	1.37	24.94	102.14	13/179	piD3-1_0487-0507		10:31
6.8.	Z13 ǁ60	Ga Kα	---	---	---	13/180	GaKa_0508-0512		8:32
6.8.	Z13 ǁ60	D_2	1.36	24.88	83.27	13/182	piD3-1_0513-0529		14:45

crystal: Z13 silicon 111, (**aperture**: ǁ60), **focus** : according R_{ZEISS} = 2982,24 mm , set as earlier at marks 1,2,3 2
X-ray tube 30 kV, 30 mA if not noticed, Cr anode, **exposure time**: (30+30)s
CSD6 gain D

FILE LIST PSI 2006 **PIONIC DEUTERIUM** **Run book: LEX #13**

date	*crystal aperture*	*target/source*	*$p_{average}$ /mbar*	*T /K*	*Q_p /C*	*LEX #/page*	*file name*		*comment*
7.8.	Z13 ǁ60	Ga Kα	---	---	---	13/183	GaKa_0530-0531		8:35
7.8.	Z13 ǁ60	D_2	1.35	24.79	102.13	13/183	piD3-1_0532-0552		10:44
8.8.	Z13 ǁ60	Ga Kα	---	---	---	13/185	GaKa_0553-0554		8:23
8.8.	Z13 ǁ60	D_2	1.36	24.80	99.49	13/185	piD3-1_0555-0575		10:26 *(451-462+466-575: 530.67 Cb)* 20 bar end
9.8.	Z13 ǁ60	Ga Kα	---	---	---	13/190	GaKa_0576		8:06
10.8.	Z13 ǁ60	Ga Kα	---	---	---	13/190	GaKa_0577		11:30
		πH(4-1)							
10.8	Z13 ǁ60	H_2	1.04	26.28	2.50	14/1	piH4-1_0578		CRY405020 ARM 414000 LinTab79.84 10 bar start
10.8	Z13 ǁ60	H_2	1.04	26.31	3.97	14/1	piH4-1_0579 *corrupt*		15:30 file too long for csdcluster new noise set.
10.8	Z13 ǁ60	H_2	1.06	26.54	92.31	14/3	piH4-1_0580-0598		17:02 PION3 crash after 0598
11.8	Z13 ǁ60	H_2	1.07	26.3	301.53	14/5	piH4-1_0599-0662		20:19 between 662 and 673 start MEGAPIE
14.8	Z13 ǁ60	H_2	1.06	26.4	51.37	14/15	piH4-1_0663-0673		21:06 without MEGAPIE
15.8	Z13 ǁ60	H_2	1.07	26.1	57.27	14/17	piH4-1_0674-0687		15:53
16.8	Z13 ǁ60	H_2	1.01	26.6	83.31	14/19	piH4-1_0688-0705		14:04
17.8	Z13 ǁ60	H_2	1.04	26.4	298.29	14/22	piH4-1_0706-0769		14:08 (580-769: 878.08 Cb)
									CRY40 20 00 ARM 42 31 00
20.8.	Z13 ǁ60	Ga Kα	---	---	---	14/31	GaKa_0770-0771		8:30 LinTab 79.84
20.8.	Z13 ǁ60	Ga Kα	---	---	---	14/31	GaKa_0772-0773		10:38 LinTab 50.00
20.8.	Z13 ǁ60	Ga Kα	---	---	---	14/31	GaKa_0774-0775		12:54 LinTab 95.00
20.8.	Z13 ǁ60	Ga Kα	---	---	---	14/31	GaKa_0776-0777		14:59 LinTab 70.00
20.8.	Z13 ǁ60	Ga Kα	---	---	---	14/31	GaKa_0778-0782		17:02 LinTab 59.76
		πD(3-1)							CRY402000 ARM 42310 LinTab59.76 20 bar start
21.8	Z13 ǁ60	D_2	1.27	24.5	128.38	14/35	piD3-1_0783-0811		2:12
22.8.	Z13 ǁ60	Ga Kα	---	---	---	14/37	GaKa_0812-0813		8:18

crystal: Z13 silicon 111, (**aperture**: ǁ60), **focus** : according R_{ZEISS} = 2982,24 mm , set as earlier at marks 1,2,3
X-ray tube 30 kV, 30 mA if not noticed, Cr anode, **exposure time**: (30+30)s
CSD6 gain D

Appendix B

Cabling plan

On the next side the plan of the spectrometer cabling is shown. It divides into two parts. One labeled **AREA**, which indicates the experimental setup area πE5 at PSI, and one labeled **HUT** indicating the parts placed in the control hut outside the experimental area for radiation protection reasons. The extensions to the control hut allow for adjustment and a permanent control of the spectrometer setting, the incoming pion beam current and the detector.

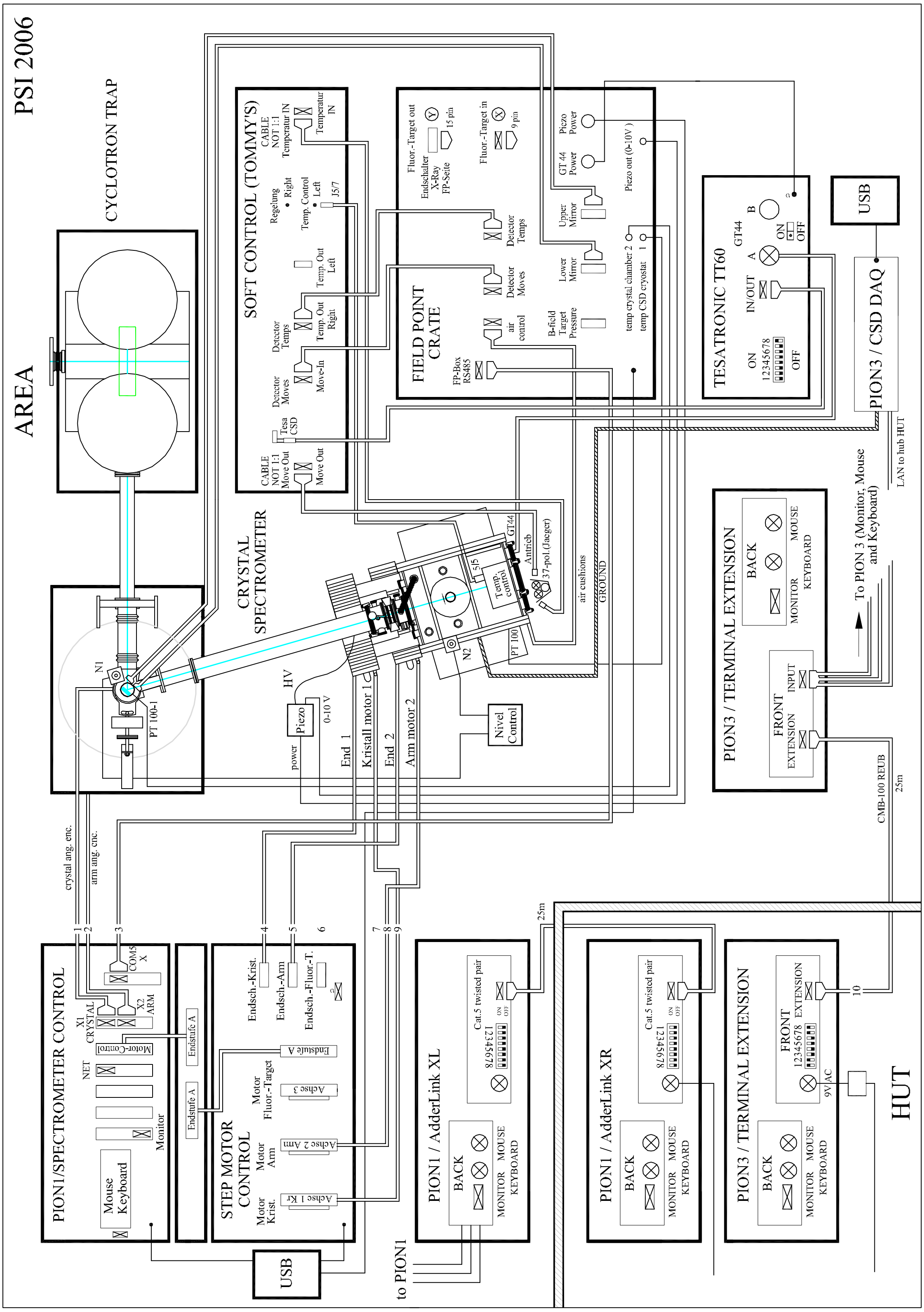
PSI 2006
AREA
HUT
CYCLOTRON TRAP
CRYSTAL SPECTROMETER
SOFT CONTROL (TOMMY'S)
FIELD POINT CRATE
TESATRONIC TT60
PION3 / CSD DAQ
USB
PION3 / TERMINAL EXTENSION
PION1/SPECTROMETER CONTROL
STEP MOTOR CONTROL
PION1 / AdderLink XL
PION1 / AdderLink XR
N1
PT 100-1
HV
Piezo
power
0-10 V
End 1
Kristall motor 1
End 2
Arm motor 2
Nivel Control
N2
PT 100
GT44
Antrieb
37-pol.(Jaeger)
5|5
Temp. control
air cushions
GROUND
CABLE NOT 1:1 Temperatur IN
Temperatur IN
Regelung
Right
Temp. Control
Left
J5/7
Temp. Out Left
Temp. Out Right
Detector Temps
Detector Moves
Move-In
Tesa CSD
CABLE NOT 1:1 Move Out
Move Out
Fluor.-Target out
Endschalter X-Ray FP-Seite
15 pin
Fluor.-Target in
9 pin
GT 44 Power
Piezo Power
Piezo out (0-10V)
Upper Mirror
Lower Mirror
Detector Temps
Detector Moves
air control
B-field Target Pressure
FP-Box RS485
temp crystal chamber 2
temp CSD cryostat 1
GT44
B
A
ON
OFF
IN/OUT
ON 12345678 OFF
LAN to hub HUT
To PION 3 (Monitor, Mouse and Keyboard)
BACK
MONITOR
KEYBOARD
MOUSE
FRONT
EXTENSION
INPUT
CMB-100 REUB
25m
crystal ang. enc.
arm ang. enc.
1
2
3
4
5
6
7
8
9
10
COMS X
X1 CRYSTAL
X2 ARM
NET
Motor-Control
Monitor
Mouse Keyboard
Endstufe A
Endsch.-Krist.
Endsch.-Arm
Endsch.-Fluor.-T.
Endstufe A
Motor Fluor.-Target
Achse 3
Motor Arm
Achse 2 Arm
Motor Krist.
Achse 1 Kr
to PION1
Cat.5 twisted pair
12345678
ON OFF
25m
9VAC

Appendix C

Vacuum system

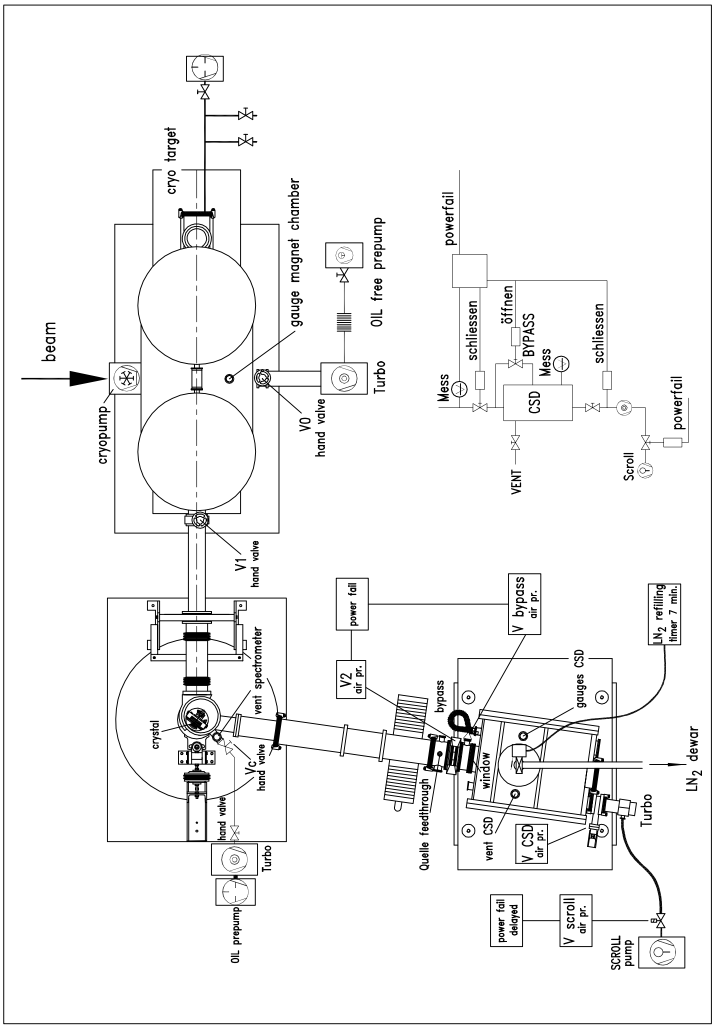

Bibliography

[1] A. W. Thomas, W. Weise, *The Structure of the Nucleon*, (WILEY-VCH, Berlin 2001).

[2] S. Weinberg, Physica A **96**, 327 (1979).

[3] J. Gasser and H. Leutwyler, Ann. Phys. **158**, 142 (1984).

[4] J. Gasser and H. Leutwyler, Nucl. Phys. B **250**, 465 (1985).

[5] H. Leutwyler, Ann. Phys. **235**, 165 (1994).

[6] J. Gasser et al., Phys. Rev. D **64**, 016008 (2001).

[7] G. Colangelo, J. Gasser and H. Leutwyler, Nucl. Phys. B **603**, 125 (2001).

[8] S. Scherer, Advances in Nucl. Phys. **27**, 277 (2003).

[9] G. Ecker, Prog. Part. Nucl. Phys. **35**, 1 (1995), and references therein.

[10] E. Jenkins, A. V. Manohar, Phys. Lett. B **255**, 558 (1991).

[11] V. Bernard, N. Kaiser, U.-G. Meissner, Int. J. Mod. Phys. E **4**, 193 (1995).

[12] D. Gotta, Prog. Part. Nucl. Phys, **52**, 133 (2004).

[13] PSI experiment R-98.01, http://www.fz-juelich.de/ikp/exotic-atoms.

[14] D. Gotta et al., Lect. Notes Phys. **745**, 165 (2008).

[15] PSI experiment R-06.03

[16] V. Lensky et al., Eur. Phys. J. A **27**, 37 (2006).

[17] C. Hanhart, *private communication.*

[18] J. Bailey et al., Phys. Lett. B **50**, 403 (1974).

[19] E. Bovet et al., Phys. Lett. **153B**, 231 (1985).

[20] D. Chatellard et al., Nucl. Phys. A **625**, 855 (1997).

[21] P. Hauser et al., Phys. Rev. C **58**, 1869 (1998).

[22] K. Kirch et al., Phys. Rev. A **59**, 3375 (1999).

[23] T. S. Jensen, PhD thesis, Universität Zürich (2002).

[24] J. S. Cohen N. T. Padial, Phys. Rev. A **41**, 3460 (1990).

[25] H. A. Bethe, E. E. Salpeter, *Handbuch der Physik*, Band XXXV (Springer, Berlin) (1957).

[26] T. S. Jensen, V. E. Markushin, Eur. Phys. J. D **21**, 261 (2002).

[27] A. V. Kravtsov, A. I. Mikhailov, I. A. Mikhailov, Phys. Rev. A **67**, 042713 (2003).

[28] J. F. Crawford et al., Phys. Lett. B **213**, 391 (1988).

[29] A. Badertscher et al., Phys. Lett. B **392**, 278 (1997).

[30] Proc. of the Int. Symp. on Exotic Atoms, Molecules and Muon Catalyzed Fusion, Hyperfine Interact. 118/119 (1999).

[31] D. Taqqu, AIP Conference Proc. **181**, 217 (1989).

[32] S. Jonsell, J. Wallenius, P. Froelich, Phys. Rev. A **59**, 3440 (1999).

[33] E. Lindroth, J. Wallenius, S. Jonsell, Phys. Rev. A **68**, 032502 (2003).

[34] S. Kilic, J.-P. Karr, L. Hilico, Phys. Rev. A **70**, 052506 (2004).

[35] E. Borie and M. Leon, Phys. Rev. A **21**, 1460 (1980).

[36] V. E. Markushin, Phys. Lett. A **59**, 1137 (1994).

[37] V. E. Markushin and T. S. Jensen, Hyperfine Int. **138**, 71 (2001).

[38] A. J. Rusi El Hassani et al., Z. Phys. A **351**, 113 (1995).

[39] T. H. Fields et al., Phys. Rev. Lett. **5**, 69 (1960).

[40] J. H. Doede et al., Phys. Rev. **129**, 2808 (1963).

[41] T. S. Jensen and V. E. Markushin, Lecture Notes in Phys. **627**, 37 (2003).

[42] D. S. Covita, Phys. Rev. Lett. **102**, 023401 (2009).

[43] D. S. Covita, PhD thesis, University of Coimbra (2008).

[44] V. P. Popov and V. N. Pomerantsev, arXiv:0712.3111 [nucl-th], (2007).

[45] K. Heitlinger et al., Z. Phys. A **342**, 359 (1992).

[46] V. P. Popov and V. N. Pomerantsev, *Private communication.*

[47] R. Frosch, Technical report TM 37-21, Paul Scherrer Institut, (1985).

[48] J. Spuller et al., Phys. Lett. B **67**, 479 (1977).

[49] V. L. Highland et al., Nucl. Phys. A **365**, 333 (1981).

[50] T. E. O. Ericson, W. Weise, *Pions and Nuclei*, Clarendon, Oxford (1988).

[51] S. Deser, L. Goldberger, K. Kaufmann and W. Thirring, Phys. Rev. **96**, 774 (1954).

[52] T. L. Trueman, Nucl. Phys. **26**, 57 (1961).

[53] G. Rasche, W. S. Woolcock, Nucl. Phys. A **381**, 405 (1982).

[54] D. Sigg et al., Nucl. Phys. A **609**, 310 (1996).

[55] T. E. O. Ericson, B. Loiseau, S. Wycech, Phys. Lett. B **594**, 76 (2004).

[56] J. Gasser, M. A. Ivanov, E. Lipartia, M. Mojzis, A. Rusetsky, Eur. Phys. J. C **26**, 13 (2002).

[57] P. Zemp, in *Proc. of Chiral Dynamics 2003*, p. 128, Bonn, Germany, Sep. 8-13 (2003).

[58] V. E. Lyubovitskij, A. Rusetsky, Phys. Lett. B **494**, 9 (2000).

[59] U.-G. Meißner, U. Raha, A. Rusetsky, Phys. Lett. B **639**, 478 (2006).

[60] V. Lensky et al., Phys. Lett. B **648**, 46 (2007).

[61] U.-G. Meißner, PoS LAT2005 009 (2005).

[62] J. Gasser, V. E. Lyubovitskij, A. Rusetsky, Phys. Rep. **456**, 167 (2008).

[63] E. Byckling and K. Kajantie, *Particle Kinematics*, J. Wiley and Sons, London (1973).

[64] J. Hüfner, *Pions interact with Nuclei* Phys. Rep. **21** (1975).

[65] A. Reitan, Nucl. Phys. B **11**, 170 (1969).

[66] L. Tauscher, Proc. 1st Course Int. School Phys. Exotic Atoms, 145 (1977).

[67] M. Leon, Nucl. Phys. A **260**, 461 (1976).

[68] E. Lambert, Helv. Phys. Acta **42**, 607 (1969).

[69] P. Indelicato, *Private communication.*

[70] W. L. Bragg, Proc. Cambridge Philos. Soc. **17**, 43 (1913).

[71] A. E. Sandström, *Handbuch der Physik*, Band XXX (Springer, Berlin) 78 (1952).

[72] W. H. Zachariasen, *Theory of X-ray Diffraction in Crystals* J. Wiley and Sons Inc., New York (1947).

[73] J. Als-Nielson, D. McMorrow, *Elements of Modern X-ray Physics* J. Wiley and Sons Inc., Chichester (2001).

[74] M. Sanchez del Rio and R. J. Dejus, *XOP: Recent developments*, Proc. SPIE **3448**, 246 (1998).

[75] H. H. Johann, Z. Phys. **69**, 185 (1931).

[76] G. Zschornack, G. Müller and G. Musiol, Nucl. Instr. Meth., **200**, 481 (1982).

[77] T. Johansson, Z. Phys. **82**, 507 (1933).

[78] J. Eggs and K. Ulmer, Z. angew. Phys., **20(2)**, 118 (1965).

[79] F. Cembali et al., J. Appl. Crystallogr., **3**, 424 (1992).

[80] M. Trassinelli, PhD thesis, l'Universite Paris VI (2005).

[81] www.psi.ch

[82] A. Gruber, Diploma thesis, Institut für Mittelenergiephysik (2003).

[83] G. Basile et al., Phys. Rev. Lett. **72**, 3133 (1994).

[84] J. R. Janesick, *Scientific Charge-Coupled Devices* (SPIE Press, Bellingham, Washington) (2001).

[85] N. Nelms et al., Nucl. Instr. Meth. A **484**, 419 (2002).

[86] Marconi Applied Technologies with University of Leicester; A. D. Holland et al., Proc. SPIE **2808**, 414 (1996).

[87] N. Dolfus, *Private communication.*

[88] M. Hennebach, PhD thesis, Universität zu Köln (2003).

[89] M. Trassinelli et al., Rev. Sci. Instr. **77**, 043107 (2006).

[90] C. Weidemann, Diploma thesis, Friedrich-Schiller-Universität Jena (2007).

[91] D. Gotta and M. Hennebach, *Private communication.*

[92] L. M. Simons, *Private communication.*

[93] D. Gotta, *Private communication.*

[94] R. Deslattes et al., Rev. Mod. Phys. **75**, 35 (2003).

[95] L. M. Simons, program X-track *Private communication.*

[96] S. Biri, L. M. Simons, D. Hitz, Rev. Sci. Instr. **71**, 1116 (2000).

[97] D. Anagnostopoulos et al., Nucl. Instr. Meth. A **545**, 217 (2005).

[98] C. Bernard, PhD thesis, l'Universite Lyon (1996).

[99] A. Hirtl, P. Hauser, *Private communication.*

[100] F. James and M. Roos, program package Minuit, Comput. Phys. Commun **10**, 343 (1975).

[101] S. Baker and R. D. Cousins, Nucl. Instr. and Meth. **221**, 437 (1984).

[102] T. Hauschild and M. Jentschel, Nucl. Instr. and Meth. A **457**, 384 (2001).

[103] U. C. Bergmann and K. Riisager, Nucl. Instr. and Meth. A **489**, 444 (2002).

[104] A. Hirtl, PhD thesis, Technische Universität Wien (2008).

[105] T. Köhler, D. Rohmann, program Fitos, Eur. Org. Nucl. Research, Geneva (1984).

[106] C. T. Chantler, J. Phys. Chem. Ref. Data **24**, 71 (1995).

[107] T. Mooney, *Private communication.*

[108] F. S. Crawford and M. L. Stevenson, Phys. Rev. **97**, 1305 (1955).

[109] C. M. Rose, Phys. Rev. **154**, 1305 (1967).

[110] C. Richard-Serre et al., Nucl. Phys. B **20**, 413 (1970).

[111] D. Aebischer et al., Nucl. Phys. B **108**, 214 (1976).

[112] D. A. Hutcheon et al., Phys. Rev. Lett. **64**, 176 (1990).

[113] B. G. Ritchie et al., Phys. Rev. Lett. **66**, 568 (1991).

[114] P. Heimberg et al., Phys. Rev. Lett. **77**, 1012 (1996).

[115] M. Drochner et al., Nucl. Phys. A **643**, 55 (1998).

[116] A. H. Rosenfeld, Phys. Rev. **96**, 139 (1954).

[117] D. S. Koltun and A. Reitan, Phys. Rev. **141**, 1413 (1969).

[118] I. R. Afnan and A. W. Thomas, Phys. Rev. C **10**, 109 (1974).

Danksagung

Ganz herzlich bedanken möchte ich mich bei

Herrn Prof. Dr. H. Ströher, dass ich meine Doktorarbeit am Institut für Kernphysik des Forschungszentrums Jülich anfertigen konnte,

Herrn PD Dr. D. Gotta für die umfangreiche Betreuung meiner Arbeit und die ständige Bereitschaft und Ruhe für Erklärungen, Diskussionen und Hilfestellungen aller Art, die unersetzlich zum Gelingen dieser Arbeit beigetragen haben,

Herrn Prof. Dr. A. Zilges für die Übernahme des Korreferats,

Herrn K.-P. Wieder sowohl für die technische Hilfe als auch für die Hilfe beim Erstellen der zahlreichen Zeichnungen,

Herrn Dr. L. M. Simons für die Unterstützung während der Messung am PSI, die Bereitstellung von Analyseroutinen und viele fruchtvolle Diskussionen und Anregungen,

Herrn Dr. A. Hirtl für die Bereitstellung und die Einführung in die Analyseroutinen und zahlreiche Diskussionen zur Breitenanalyse,

Herrn C. Weidemann für die Analyse der Vermessung des CCD-Array,

Herrn Dr. M. Nekipelov für Hilfe bei allen Computerfragen,

allen Mitgliedern des IKP-2, der Mechanik- und der Elektronikwerkstatt für ihre ständige Hilfsbereitschaft,

allen für das allzeit gute Arbeitsklima,

und nicht zuletzt, meiner Familie.

Special thanks to all members of the pionic hydrogen collaboration, too numerous to name here explicitly, it was a pleasure to work with you even under outstanding conditions.

Erklärung

Ich versichere, dass die von mir vorgelegte Dissertation selbständig angefertigt, die benutzten Quellen und Hilfsmittel vollständig angegeben und die Stellen der Arbeit - einschließlich Tabellen, Karten und Abbildungen -, die anderen Werken im Wortlaut oder dem Sinn nach entnommen sind, in jedem Einzelfall als Entlehnung kenntlich gemacht habe; dass diese Dissertation noch keiner anderen Fakultät oder Universität zur Prüfung vorgelegen hat; dass sie - abgesehen von unten angegebenen Teilpublikationen - noch nicht veröffentlicht worden ist sowie, dass ich eine solche Veröffentlichung vor Abschluss des Promotionsverfahrens nicht vornehmen werde. Die Bestimmungen der Promotionsordnung sind mir bekannt. Die von mir vorgelegte Dissertation ist von Herrn PD Dr. D. Gotta betreut worden.

Thomas Strauch